TUM School of Life Sciences

Lehrstuhl für Pflanzenernährung

Advancing digital farm management by machine learning and remote sensing

Michael Lukas Marszalek

Vollständiger Abdruck der von der TUM School of Life Sciences der Technischen Universität München zur Erlangung des akademischen Grades eines

Doktor-Ingenieurs (Dr.-Ing.)

genehmigten Dissertation.

Vorsitzender:

Prof. Dr. Kang Yu

Prüfende der Dissertation:

1. Prof. Dr. Urs Schmidhalter
2. Prof. Dr. Senthold Asseng
3. Priv.-Doz. Dr. habil. Marco Körner

Die Dissertation wurde am 17.12.2020 bei der Technischen Universität München eingereicht und durch die TUM School of Life Sciences am 12.07.2021 angenommen.

Für Monika Anna, Jan, Daniela und Matthias.

"Nothing in life is to be feared, it is only to be understood.
Now is the time to understand more, so that we may fear less."

Marie Curie (1867 - 1934)

Abstract

The knowledge of crop yields is a prerequisite for an optimisation of agricultural resources and is necessary for yield prediction. Crop yields are often aggregated at the farm level and are difficult to derive due to internal farm processes. Machine learning and remote sensing help to overcome this problem and derive yield maps at the field level. This requires the identification of crop types and the detection of field boundaries. The aim of this work was to fill these gaps with satellite data and machine learning methods to identify field boundaries and crop types that provide a basis for yield estimation at the field level. A multi-temporal and object-based approach was used to incorporate the high temporal availability of Sentinel-2 data. Nevertheless, the methods can also be applied to pixels which is essential for implementing precision farming applications to ensure optimal fertilisation and irrigation. The identification of field boundaries and crop types is a prerequisite for yield prediction at the field level, when official data is not available. In general, the field boundaries are needed for an object-based approach to aggregate all pixels in a field to a mean value, thus generating a time series of satellite data per field. The field boundaries identification is based on edge detection and was successfully evaluated in first experiments. The edge detection reveals many irrelevant edges and significantly increases the noise ratio. This was solved by using an index to reduce the noise and focus on field borders. The user accuracy (UA) of 79% and producer accuracy (PA) of 81% confirm the method, which can be applied worldwide and without training data. Crop-type mapping achieved around 92% overall accuracy (OA) using Sentinel-2 raw bands, which can be further improved with hyper-parameter optimisation. Random forest (RF) and support vector machine (SVM) were compared, with RF performing more efficient, especially for predictions under atypical climatic conditions. The main crop types, grown in Bavaria, were classified and experiments with a rejection class ("Other") were conducted to account for crop types not considered. This resulted in slightly lower

accuracies, which is why it is preferable to work solely with the target crop types. The crop-type classification is usually investigated with data from the same time spectrum, but a real application requires experiments with predictions of an unknown year and without labels. Official crop types are sometimes not available or only available with a organisation delay, so a model with data from 2016 and 2017 was trained to predict crop types in 2018. 2018 was an atypical year, influenced by periods of drought and heat, which also affected the plant growth and its spectral signature. Nevertheless, the model classified the crop types with an overall accuracy of 86% for one experimental area. Another important result relates to the use of all raw bands from Sentinel-2, which reveals multi-spectral distinguishing features compared to an application-oriented index. This spectral bandwidth improves the yield prediction, but not as significantly as in crop-type classification. The aim of this work was to produce yield prediction at the field level for the years 2016 to 2018 and to evaluate them quantitatively. Depending on the features, up to 90% of the yield variance of winter wheat was explained. Linear regression (LR) and random forest were compared, with LR achieving higher accuracies. RF requires more samples while LR generalises better. Yield data at the field level is difficult to obtain, and this is one reason why previous research has focused on yield prediction at the regional level. In contrast, this work analysed each field in terms of yield and its relationship to water. This is also an important aspect, because previous empirical research was conducted with indirect parameters or isolated indices. LR and RF were helpful because both approaches provided the significance or "feature importance" to explain relationships. The applied methodology is additionally based on a physical model for evapotranspiration using climatological and satellite data. Especially, the incorporation of the normalised difference water index ($NDWI$), red edge inflection point ($REIP$) and all raw bands achieved the best results for yield prediction. In this context, approaches for an optimal irrigation at the field level were also discussed. This thesis covers several topics on yield prediction at the field level, reflects the state-of-the-art and discusses future satellite-based approaches for advanced digital and sustainable farm management.

Zusammenfassung

Die Kenntnis der Erträge landwirtschaftlicher Betriebe auf der Feldebene stellt eine Grundvoraussetzung für die Optimierung landwirtschaftlicher Ressourcen dar und ist für eine Ertragsvohersage erforderlich. Häufig liegen Erträge nur aggregiert auf der Betriebsebene vor oder Erträge können aufgrund des innerbetrieblichen Kreislaufs nur grob abgeleitet werden. Mit Methoden der Fernerkundung und des maschinellen Lernens könnten Erträge auf der Feldebene erfasst werden. Voraussetzung dafür ist wiederum die Kenntnis der Feldgrenzen wie auch die Identifikation der Fruchtarten. Ziel dieser Arbeit war es somit diese Lücken zu füllen, indem basierend auf Satellitendaten und mit Methoden des maschinellen Lernens Feldgrenzen und Fruchtarten identifiziert wurden und darauf basierend Erträge auf Feldebene geschätzt wurden. Hierbei wurde ein objektbasierter und multitemporaler Ansatz verwendet, um die hohe zeitliche Verfügbarkeit von Sentinel-2 Daten zu nutzen. Diese Methoden können auch auf einzelne Pixel angewendet werden, welches für die Umsetzung von Precision Farming Anwendungen essentiell ist, um die Düngung und Bewässerung mengenmäßig zu optimieren. Die Kenntnis der Feldgrenzen wird für einen objektbasierten Ansatz benötigt, um alle im Feld liegenden Pixel zu einem Mittelwert zu aggregieren und eine Zeitreihe von Satellitendaten pro Feld zu generieren. Die Feldgrenzenerkennung basiert auf einer Kantenerkennung und wurde in vorhergehenden Experimenten erfolgreich evaluiert. Kantenerkennung detektiert viele nicht relevante Kanten, welche das Rauschverhältnis deutlich erhöhen. Eine Indexbildung ermöglichte es die Anzahl der Kanten im Feld zu reduzieren und den Fokus auf die Feldgrenzen zu legen. Die erzielte Nutzergenauigkeit (UA) von 79% und eine Herstellergenauigkeit (PA) von 81% bestätigen die Richtigkeit der Methodik, welche sich weltweit anwenden lässt und ohne Trainingsdaten auskommt. Die Fruchtartenerkennung erreichte mittels Rohbändern von Sentinel-2 eine Gesamtgenauigkeit von 92% OA, wobei dieses Ergebnis mittels Hyperparameteroptimierung weiter verbessert werden kann.

Random Forest (RF) und Support Vector Machine (SVM) wurden verglichen und es zeigte sich, dass RF für die Fruchtartenbestimmung besser geeignet ist, besonders für die Vorhersage unter klimatisch abweichenden Bedingungen. Die Hauptfruchtarten in Bayern wurden hierbei klassifiziert, wobei auch Experimente mit einer Ablehnungsklasse ("Other" rejection class) durchgeführt wurden, um zusätzlich nicht betrachtete Fruchtarten in einer Klasse zu vereinen. Dies war zwar erfolgreich, jedoch führte es auch zu einer leichten Verschlechterung der Ergebnisse. Es ist vorteilhafter direkt mit den betrachteten Fruchtarten zu arbeiten. Ein weiterer wichtiger Aspekt für eine reale Umsetzung ist die Nutzung eines Modells mit Daten aus vergangenen Jahren. Offizielle Fruchtarten liegen in manchen Gebieten nicht vor oder sind nachträglich verfügbar. Aus diesem Grund wurde eine Vorhersage von Fruchtarten für 2018 durchgeführt, wobei das Modell mit Daten aus 2016 und 2017 trainiert wurde. Das Jahr 2018 war geprägt durch trockene Perioden und Hitze, welche sich im Pflanzenwachstum und in der spektralen Signatur auswirkten. Nichtsdestotrotz konnte das Modell die Fruchtarten mit einer Genauigkeit von bis zu 86% für ein Testgebiet im Jahr 2018 bestimmen. Ein weiteres wichtiges Ergebnis bezieht sich auf die Nutzung aller Rohbänder von Sentinel-2, die im Vergleich zu einem Index-basierten Ansatz mehr spektrale Unterscheidungsmerkmale erkennen lassen. Diese spektrale Bandbreite verbesserte auch die Ertragsvorhersage, jedoch nicht so signifikant wie bei den Fruchtarten. Im Rahmen dieser Arbeit wurden Winterweizenerträge für 2016 bis 2018 quantitativ bewertet. Je nach Feature-Zusammenstellung konnten bis zu 90% der Ertragsvarianz der Winterweizenerträge erklärt werden. Lineare Regression (LR) und Random Forest wurden als Methoden verglichen, wobei LR die höchsten Genauigkeiten erzielte. RF benötigt mehr Ertragsdaten während LR besser generalisiert. Ertragsdaten auf Feldebene sind schwer verfügbar, weswegen in früheren Arbeiten Ertragsvorhersagen hauptsächlich auf Regionalebene untersucht wurden. Im Gegensatz dazu wurden in dieser Arbeit einzelne Felder und deren Wasserverfügbarkeit betrachtet. Dies ist auch deshalb ein wichtiger Aspekt, weil frühere empirische Forschungsarbeiten mit indirekten Parametern oder isolierten Indizes durchgeführt wurden. LR und RF sind hilfreich, da mittels Signifikanz und 'Feature Importance' auch Zusammenhänge erklärt werden können. Die angewandte Methodik basiert zusätzlich auf einer physikalischen Modellierung der Evapotranspiration mittels Wetterdaten und integrierten Satellitendaten. Die

Integration der Indizes $NDWI$, $REIP$ und der Rohbänder ergab die besten Ergebnisse in der Ertragsvorhersage. In diesem Zusammenhang werden auch Ansätze für eine optimale Bewässerung auf Feldebene diskutiert. Diese Arbeit thematisiert verschiedene Aspekte der Ertragsvorhersage auf Feldebene, spiegelt den gegenwärtigen Stand der Technik wieder und diskutiert zukünftige satellitenbasierte Ansätze für eine verbesserte digitale und nachhaltige Bewirtschaftung.

Contents

List of Figures

List of Tables

Acronyms

CWR	Crop Water Requirement
ET_c	Crop Evapotranspiration
$EVI2$	Enhanced Vegetation Index
K_c	Crop Coefficient
LAI	Leaf Area Index
MAE	Mean Absolute Error
$NDRE$	Normalised Difference Red Edge Index
$NDVI$	Normalised Difference Vegetation Index
$NDWI$	Normalised Difference Water Index
$REIP$	Red Edge Inflection Point
$RMSE$	Root Mean Absolute Error
$SAVI$	Soil Adjusted Vegetation Index
$TVDI$	Temperature Vegetation Dryness Index
ACIX	Atmospheric Correction Intercomparison Experiment
ALOS	Advanced Land Observing Satellite
AMBAV	Agrarmeteorologisches Modell zur Berechnung der Aktuellen Verdunstung
ANN	Artificial Neural Network
ASI	Agenzia Spaziale Italiana
AWS	Amazon Web Services
AZMET	Arizona Meteorological Network
CNN	Convolutional Neural Network

DWD	German Meteorological Service
EnMAP	Environmental Mapping and Analysis Program
EO	Earth Observation
EO-1	Earth Observing-1
ESA	European Space Agency
ET	Evapotranspiration
FAO	Food and Agriculture Organisation
GEE	Google Earth Engine
GLONASS	Globalnaja Nawigazionnaja Sputnikowaja Sistema
GNSS	Global Navigation Satellite Systems
GPS	Global Positioning System
IoU	Interception over Union
IR	Infrared
JAXA	Japan Aerospace Exploration Agency
L1C	Level-1C
L2A	Level-2A
LR	Linear Regression
LST	Land Surface Temperature
METRIC	Mapping EvapoTranspiration at high Resolution with Internalised Calibration
MODIS	Moderate Resolution Imaging Spectroradiometer
N	Crop Nitrogen

NASA	National Aeronautics and Space Administration
NIR	Near Infrared
NRT	Near Real-Time
OA	Overall Accuracy
OpenCV	Open Computer Vision
OSM	OpenStreetMap
PA	Producer Accuracy
PF	Precision Farming
PRISMA	PRecursore IperSpettrale della Missione Applicativa
PROBA	PRoject for On-Board Autonomy
Py6S	Python interface to the 6S Radiative Transfer Model
RF	Random Forest
S-SEBI	Simplified Surface Energy Balance Index
SAR	Synthetic-Aperture Radar
SciHub	Sentinels Scientific Data Hub
SDGs	Sustainable Development Goals
SEB	Surface Energy Balance
SEBAL	Surface Energy Balance Algorithm for Land
SLC	Scan Line Corrector
SM	Soil Moisture
SMAP	Soil Moisture Active Passive
SMOS	Soil Moisture and Ocean Salinity
SNIC	Simple Linear Iterative Clustering
SPOT	Satellite Pour l'Observation de la Terre
SSEBop	Operational Simplified Surface Energy Balance
SSM	Surface Soil Moisture
StMELF	Bavarian State Ministry of Agriculture and Forestry

SVM	Support Vector Machine
SWIR	Short Wave Infrared
TDR	Time Domain Reflectometry
TIRS	Thermal Infrared Sensor
UA	User Accuracy
UAV	Unmanned Aerial Vehicle
USA	United States of America
USGS	United States Geological Survey
VNIR	Visible and Near Infrared
WOFOST	World Food Studies

1 Introduction

1.1 Precision farming and satellite remote sensing

Precision farming (PF) is based on several technologies ranging from drones, sensors, Global Positioning System (GPS) to satellites. GPS is a satellite navigation system, operated by the United States of America (USA). It is sometimes confused with other satellite navigation systems, which can be summarised as Global Navigation Satellite Systems (GNSS). Other constellations include the Chinese system Beidou, the Russian Globalnaja Nawigazionnaja Sputnikowaja Sistema (GLONASS) and Galileo, the European navigation system. All of them provide high localisation accuracies for end users and thus enable various applications such as variable rate application, soil sampling or vehicle guidance (Goswami et al., 2012; Pérez-Ruiz and Upadhyaya, 2012). Terrestrial sensors based on electromagnetic induction or infrared spectroscopy, provide insights into soil properties, plant health, water or nitrogen (N) status (Becker and Schmidhalter, 2017; Mistele and Schmidhalter, 2010; Rischbeck et al., 2016). Modern tractors are often equipped with proximal near infrared sensors, used for variable rate application, which on the one hand save costs, and on the other hand allow to optimise nitrogen application, thus protecting the environment (Schmidhalter et al., 2008). A tractor-based near infrared sensor may enable to precisely measure and predict grain yield (Barmeier et al., 2017).

Unmanned aerial vehicles (UAV's) are used for different applications and must be controlled by an user within the visual range. They allow rapid and nondestructive analysis of soils or crop growth (IPATE et al., 2015). Nevertheless, it is an advantage of UAV's, that they can be flexibly equipped with different sensors, for instance for determining ground temperature or for reflection measurements in the near infrared (NIR) or short wave infrared (SWIR) spectrum. Other advantages are high resolution images which

are available independent of cloud cover. The application of UAV's is also associated with material and personnel deployment. In addition, processing of data after an overflight must be carried out. From a research perspective, the high resolution images and flexibility make UAV's very interesting (Saiz-Rubio and Rovira-Más, 2020), but satellites are better suited for practice-oriented PF applications (Sishodia et al., 2020). Table 1.1 gives an overview of the most interesting satellite missions identified for PF. In general, satellites offer different resolutions and sensors. High-resolution images can be obtained from commercial operators offering images up to a resolution of 0.3 metres. Free of charge data can be obtained e.g. from the Landsat or Sentinel mission. The high resolution, revisit time and free availability of data are ideal for PF why Table 1.1 summarises only free satellite data. Figure 1.1 shows the corresponding assignment in the electromagnetic spectrum. A distinction is made between satellites with hyperspectral, multispectral and radar-based sensors. Hyperspectral sensors offer a high amount of bands in the SWIR, visible and near infrared (VNIR) spectrum. SWIR also provides thermal information which are important for soil moisture determination or surface temperatures. The Landsat mission dates back to the 1970s and were a great success for the first developments of Earth observation (EO) applications. Since the availability of images is a limiting factor solved by the Sentinel mission, this research work focuses on Sentinel-2. A minor analysis was done with Sentinel-1 data to assess soil moisture, but this was not the objective of this thesis. The Sentinel-2 mission started in June 2015 and reached its fully capability in 2017. The worldwide availability of data enables the monitoring of agricultural areas and adapted solutions for digital farm management. Independent of the determination of soil moisture, Sentinel-1 was also evaluated for other applications in agriculture (Khabbazan et al., 2019; Mercier et al., 2020; Nasrallah et al., 2019). The advantage of radar is its independence from clouds due to the frequency range used.

Table 1.1: Overview of current satellite missions and their technical characteristics which can be used for precision farming applications.

Satellites	Launch	Resolution	Sensor type	Spectral Characteristics	Revisit time	Data	Source
Sentinel-3A, Sentinel-3B	3A: 02/2016, 3B: 04/2018	300, 500 m Thermal: 1000 m	Optical SAR	21 spectral bands: 400 - 1020 nm (300 m), 550 - 12000 nm (0.5 -1 km), Altimeter: 13.575 / 5.41 GHz, Radiometer: 23.8 / 36.5 GHz	NRT <2 days	SciHub Google AWS	(ESA, 2020f) (Wikipedia contributors, 2020e)
Sentinel-2A, Sentinel-2B	2A: 06/2015, 2B: 03/2017	10, 20, 60 m	Optical	13 spectral bands, 442,7 - 2202,4 nm	3-5 days	SciHub Google AWS	(ESA, 2020e) (Wikipedia contributors, 2020d)
Sentinel-1A, Sentinel-1B, Sentinel-1C, Sentinel-1D	1A: 04/2014, 1B: 04/2016, 1C/1D: planned	SM: 5x5 m, IW: 5x20 m, EW: 25x100 m, WV: 5x20 m	SAR C-Band	Central Frequency: 5.405 GHz, Polarization: HH+HV, VV+VH, VV, HH	2-5 days	SciHub Google AWS	(ESA, 2020d) (Wikipedia contributors, 2020c)
Proba-1	10/2001	17 m, Pan: 8 m	Hyper-spectral	62 spectral bands, Different viewing angles for same spot	7 days	ESA	(ESA, 2020c)
EnMap	2021	30 m	Hyper-spectral	VNIR: 420 - 1000 nm, SWIR: 900 - 2450 nm	4 days		(DLR, 2020)
Landsat-7	04/1999	15, 30 m, Thermal: 60 m	Optical	8 spectral bands: 450 - 2350 nm 10400 - 12500 nm	16 days	NASA Google AWS	(USGS, 2020)
Landsat-8	02/2013	15, 30 m, Thermal: 100 m	Optical	11 spectral bands: 433 - 1390 nm, 10300 - 12500 nm	16 days	NASA Google AWS	(Wikipedia contributors, 2020b)
Terra/ Aqua MODIS	Terra: 12/1999, Aqua: 05/2002	250, 500, 1000 m	Optical	36 spectral bands: 400 - 14400 nm	1-2 days	NASA Google AWS	(NASA, 2020)
EO-1 Hyperion	11/2000	30 m	Hyper-spectral	224 bands: VNIR: 426.82 - 925.41 nm, SWIR: 912.45 - 2395.50 nm	16 days	USGS Google (<2017)	(GEE, 2020) (Wikipedia contributors, 2020a)
ALOS-2	05/2014	Strip: 3 - 10 m, ScanSAR: 100 m, Spotlight: 1 x 3 m	SAR L-Band	1257,5 MHz	14 days	Google JAXA	(ESA, 2020a)
PRISMA	03/2019	30 m, Pan: 5 m	Hyper-spectral	238 bands: VNIR: 400-1010 nm, SWIR: 920-2505 nm, PAN: 400-700 nm	29 days	ASI	(ESA, 2020b)

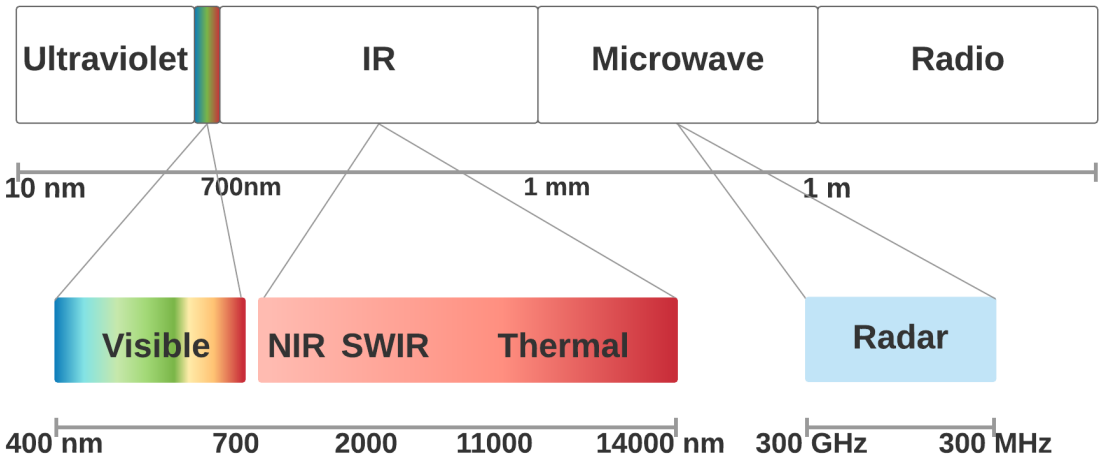

Figure 1.1: Overview of the electromagnetic spectrum and spectral classification used for Earth observation. Depending on the wavelength, different parameters such as texture, temperature or chlorophyll content can be determined. Especially the infrared (IR) radiation with its NIR, SWIR and thermal bands is used in PF.

1.2 Crop water demand

Crop water demand is an important aspect of PF as it ensures yields especially in regions with water scarcity. Climate change means that irrigation may soon be needed even in regions that have not experienced water stress. Section 1.2.1 and section 1.2.2 therefore compare satellite-based soil moisture and evapotranspiration assessments and their usability for field level mapping.

1.2.1 Soil moisture

The determination of high resolution soil moisture (SM) estimates can be performed with the C-band synthetic-aperture radar (SAR) of Sentinel-1 (Wagner et al., 2010). Other missions like Soil Moisture and Ocean Salinity (SMOS) or Soil Moisture Active Passive (SMAP) offer a L-band radar, which is more suitable for soil moisture (SM) determination, since it is not as strongly influenced by vegetation as the C-band. However, both missions do not provide the required field level resolution, so these missions are not listed in Table 1.1 (El Hajj et al., 2018b). A SAR system is characterised by frequency, polarisation and its active sensor. While the frequency range enables to penetrate clouds and vegetation, the polarisation determines the diffusion. The penetration of soil and

vegetation decreases with a rising frequency. Active means that modulated and pulsed electromagnetic waves are transmitted and the backscattered signals are received by the same satellite (Moreira and Krieger, 2003). Various methods have been investigated for SM retrieval. Paloscia et al. (2013) used an artificial neural network (ANN), resulting in results with a $RMSE$ of around 4%. A multi-temporal approach, based on Bayes, which incorporates multiple observations over time achieved soil moisture estimates that correlate with corresponding precipitation over time (Pierdicca et al., 2014). These authors propose to exploit optical data in order to correct the underlaying vegetation. In general, the relationship between backscatter and SM is nonlinear, affected by surface roughness, topography and vegetation (Greifeneder et al., 2016; Greifeneder et al., 2018; Pasolli et al., 2015), why SM retrieval improves with the incorporation of land cover maps, digital elevation models and vegetation indices. Another C-band satellite mission is the Canadian RadarSAT mission. Although the data must be ordered, which is why the mission is not listed, several publications on SM retrieval have been produced with promising results (Merzouki and McNairn, 2015; Merzouki et al., 2011). The polarisation characteristics of RadarSAT and Sentinel-1 differ, which must be taken into account when comparing results. However, the SM estimates are limited to bare or sparely vegetated areas (Merzouki and McNairn, 2015), as denser vegetation over time strongly influences the SM estimates. In addition to radar-based approaches, hyperspectral sensors or thermal bands can be used to derive the ground temperature and indirectly the SM. Soil temperature correlates with soil moisture and was investigated in several studies (Al-Kayssi et al., 1990; Aliyu Kasim et al., 2020; Idso et al., 1975; Lakshmi et al., 2003; Zhang et al., 2014). However, since an important requirement is the required field level resolution, Landsat-7, 8 and Sentinel-3 are particularly suitable. A planned future Sentinel mission will provide land surface temperature (LST) with a resolution of even 50 metres per pixel. The temperature vegetation dryness index ($TVDI$) is a proven method for SM retrieval based on LST and a vegetation index (Li et al., 2016; R. et al., 2009; Sandholt et al., 2002). Although it delivered good correlations, the indirect negative relationship is prone to errors depending on the vegetation (Li et al., 2016; Mallick et al., 2009). Liang et al. (2020) applied high resolution vegetation indices such as the normalised difference vegetation index ($NDVI$), the normalised difference water index

($NDWI$) and leaf area index (LAI) from Sentinel-2 in order to determine surface soil moisture and obtained a good correlation with SM in wetlands. Foroughi et al. (2020) presented a solution verified for a sugarcane field and based on red and NIR reflectance values and without thermal information. The authors mention that the correlation decreases with soil depth, why this approach is not suitable for deriving the root zone SM. Serrano et al. (2019) showed that the usage of optical bands correlated with soil moisture in the upper soil up to 20 cm for the test site with grass cover. The authors used the $NDWI$, which is related to leaf moisture content and achieved a R^2 of 0.76 for biomass productivity and a R^2 of 0.75 for soil moisture. In comparison to the presented SAR methods, which directly determine soil moisture, this represents an interesting agreement. Both approaches (direct or indirect) are limited by vegetation cover or soil depth. All presented approaches deliver SM estimates for the upper soil. A comparison of several active and passive satellite missions also concluded that although it is very well possible to determine soil moisture in general, soil moisture cannot be determined in the root zone (Ahmed et al., 2011). However, the root zone must also be considered as long as the plant type is not grass. In addition, backscatter absorption by the vegetation cover complicates reliable SM measurements and thus a current incorporation into yield prediction systems.

1.2.2 Evapotranspiration

Besides SM, evapotranspiration (ET) has the potential to monitor crop water needs. ET accounts for the evaporation of soil and transpiration of plants. It is a proxy for water demand of plants and can be measured by local sensors (e.g. lysimeter) or satellites. In recent years, several approaches for ET determination have been developed with a focus on surface energy balance (SEB) models or Penman-based approaches. Important examples for energy balance models are surface energy balance algorithm for land (SEBAL) (Bastiaanssen et al., 2005; Sun et al., 2011), mapping evapotranspiration at high resolution with internalised calibration (METRIC) (Allen et al., 2007; McShane et al., 2017), operational simplified surface energy balance (SSEBop) (McShane et al., 2017; Senay et al., 2013) and simplified surface energy balance index (S-SEBI) (Roerink et al., 2000). All models require LST as a prerequisite (Senkondo et al., 2019), but

only SSEBop and S-SEBI do not require additional information such as climatological data and provide ET estimates based purely on remote sensing data. A comparison of METRIC with SSEBop regarding advantages and disadvantages has been made by McShane et al. (2017). Senkondo et al. (2019) verified successfully energy balance models for a region in Tanzania by integrating Moderate Resolution Imaging Spectroradiometer (MODIS) data. S-SEBI, SEBAL and SSEBop provided similar results and can be used for hydrological models, since the medium spatial resolution is only partially suitable for PA. MODIS provides besides RGB also NIR, SWIR and surface temperature data with a high temporal availability, but at the cost of spatial resolution. The use of MODIS is especially suitable for energy balance models because of the surface temperature data (Faisol et al., 2020; Huang et al., 2017; Li et al., 2009), but only for the production of ET maps at the regional level. An advantage of certain SEB models is the independence of climatological data which is interesting for regions without local weather stations. However, field accurate ET mapping requires high resolution temperature data which is only possible with Landsat 8, 7 and 5. Landsat 5 was operational from 1984 to 2013. Landsat 7 is still in operation, but there are gaps in the acquisitions due to a scan line corrector (SLC) error. While Landsat-7 provides processed 30 m temperature images, the thermal infrared sensor (TIRS) of Landsat 8 provides surface temperature data with a resolution of 100 metre (Jeevalakshmi et al., 2017; Sekertekin and Bonafoni, 2020). Even if the data is scaled up to 30 metres, this would meet the PF requirements, but revisit time would be still problematic. Landsat has a revisit time of around 2 weeks and the data availability is limited by clouds (see Table 1.1). Sentinel-3 solves the temporal coverage but its temperature data have a resolution of around 1 km. A fusion of Sentinel-3 and Sentinel-2 was shown during the preparation of this work and estimates the actual evapotranspiration with a resolution of 20 metres (Guzinski et al., 2020). This could be a potential alternative approach for irrigation management or yield forecasts.

A very straightforward methodology for irrigation management is the application of Penman-Moneith (FAO56) (Allan et al., 1998; FAO, 2020) which is based on climatological data and a crop coefficient K_c. The K_c coefficient adapts a reference evapotranspiration ET_0 over grass and under standard conditions to a crop-specific evapotranspiration ET_c. It can be determined by remote sensing as indices or raw reflectance can monitor crop

type and plant phenology (D'Urso and Belmonte, 2006; Kamble et al., 2013; Marszalek et al., 2020). Vuolo et al. (2015a) describes the K_c factor as a proxy where the LAI index, albedo radiation and crop height are estimated using satellite data. The crop coefficient also considers the heterogeneity of fields e.g. due to soil differences or farming practices (D'Urso and Belmonte, 2006). A drawback of this approach is the dependence on climatological data, and thus on the distribution of weather stations, which varies from country to country. A weather station can be several kilometers away from a field. An irrigation solution at the field level based on the $NDVI$ or LAI was recently proposed (D'Urso and Belmonte, 2006; D'Urso et al., 2010; Vuolo et al., 2015a). This methodology optimises the water usage on the one hand and ensures the yields on the other (Vuolo et al., 2015a,b). Although water is free of charge in Europe, the energy costs for the water pumps can be very high over time and the water availability is frequently limited. Since the presented soil moisture approaches in section 1.2.1 consider the upper soil and suffer from vegetation cover, active and passive soil moisture estimates have not been considered for winter wheat yield prediction in section 3.3. The promising results obtained with the FAO56 methodology will be used to determine crop water requirements (CWR) and ultimately to predict yields to incorporate the water requirements of winter wheat.

1.3 Crop-type identification

Crop-type mapping was one aspect of this work since it is related to yield prediction. Crop types have to be identified before a yield prediction can be applied if no crop information or land cover masks are available (Friedl and Sulla-Menashe, 2019). Crop-type mapping has been investigated in several studies and the corresponding data sets have been published to enable other researchers to compare their methods and to establish benchmarks (Marszalek et al., 2020; Remelgado et al., 2020; Rußwurm et al., 2020). The research studies differ between classifications based on one satellite or UAV image (Böhler et al., 2018; Chetan et al., 2017; Immitzer et al., 2016; Mazzia et al., 2019; Natteshan and Kumar, 2020; Saini and Ghosh, 2018; Wei et al., 2019) and a multi-temporal stack of images (Belgiu and Csillik, 2018; Dimitrov et al., 2019; Harfenmeister et al., 2018; Marszalek et al., 2020; Vuolo et al., 2018). Multi-temporal crop-type classification uses time as

a significant dimension that maps information on the development of the crop types. This enable to include the spectral response and phenology of a crop type, resulting in a more efficient classification. The implementation of multi-temporal approaches requires stable and gap-less observations and appropriate methods for noise reduction and gap filling (Lepot et al., 2017). In the past, the availability of high-resolution satellite data limited these techniques, or it was important to use medium resolutions such as MODIS data to meet this requirement. However, the availability of Sentinel-2 multispectral data changed this, as its resolution and time coverage solved this problem. Only cloud cover remains a limiting factor, especially in regions with high cloud cover. For instance, the identification of crop types in the tropics would be a challenge that could be overcome by SAR satellites, since radar operates independently of cloud cover or sunlight (Orynbaikyzy et al., 2019; Tricht et al., 2018). Regions with average cloud cover do not necessarily require fusion with radar data, since the temporal coverage of Sentinel-2 provides sufficient data. Independent of the used data, various methods have been investigated for this purpose with various sample sizes and classification accuracies (Belgiu and Csillik, 2018; Ma et al., 2017; Nitze et al., 2012). However, there is a lack of practical considerations, since the results are based on train/test splits in the same year. In many countries ground truth data (crop types) is not available or will be made only available in the course of the year. A train/test split for the same year or region is appropriate for comparing the efficiency of methods or various feature sets, but when it comes to real-world applications, it must be possible to determine crop types in a region or year without ground truth data. Belgiu and Csillik (2018); Maus et al. (2016); Petitjean et al. (2012) recognised this issue and emphasise that a time series for a crop type can differ from year to year as weather anomalies or management practices affect the spectral characteristics of the plants. Hao et al. (2016) is a rare work which addressed this issue and predicted crop types for a year without ground truth data and based on $NDVI$ time series from Landsat and MODIS. The authors achieved an accuracy of up to 87.13%, which is slightly lower than research studies, where the validation is based on the same year. Early classification of crops is also essential from a practical point of view and considers the best possible classification as early as possible before harvest. Mori et al. (2018) proposed the usage of a cost function and stopping rule for early classification.

Rußwurm et al. (2019) proposed a neural network with a stopping rule to classify crops in 2018. One important finding is that the stopping dates for each class presented were in June and July before harvest. Another characteristic issue is the similarity of some crop types, as certain crops have similar spectral characteristics, e.g. winter barley and winter wheat (Dimitrov et al., 2019). Nevertheless, this topic is also a methodological problem. Some research projects use indices for crop-type classification, with $NDVI$ being most frequently used (Belgiu and Csillik, 2018; Dimitrov et al., 2019; Sousa et al., 2019). The question arises why an index for biomass or chlorophyll is frequently used for crop-type or land-use classification (Sousa et al., 2019). An index can even make crop-type detection more difficult, as the biomass can often be similar at the beginning of the season, while the use of all raw bands benefits from additional insights such as colour differences (Immitzer et al., 2016).

1.4 Field boundaries

Field boundary extraction was also addressed in this thesis and has emerged in the context of crop-type detection. The detection of field borders and the creation of resulting polygons is mandatory for object-based crop-type classification or yield forecasts at the field level. The usage of object-based approaches improves the accuracy and is more efficient than pixel-based classification (Blaschke et al., 2014; Schultz et al., 2015; Watkins and Van Niekerk, 2019). Nevertheless, an object-based classification, where an aggregated mean value represents a field, does need a polygon that describes field borders. Polygons are used in order to determine a mean value over all pixels in a polygon and for each observation. The applications addressed - yield prediction and crop type detection - are based on this procedure. The field borders applied were provided by the Bavarian State Ministry of Agriculture and Forestry (StMELF) and include such information as georeferenced polygons and crop types. These labels are necessary for supervised learning, but it remains to be seen how the yield for a field in a region can be predicted without this information? An object-based approach is not possible in this case. Therefore, we reviewed the current state-of-the-art methods to find a possible solution. Field boundaries can be extracted by segmentation techniques using approaches such as deep learning or edge detection. Supervised learning approaches have proven their efficiency and

achieved excellent results (Chandwadkar, 2013; Diakogiannis et al., 2020; Masoud et al., 2020; Schultz et al., 2015; Waldner and Diakogiannis, 2019). Unsupervised learning does not need labels to learn and predict. It infers without knowledge and segments data into associated patterns. Regardless of the excellent results that can be achieved with supervised learning, unsupervised learning provides the possibility to deliver results without labels or large data processing efforts. Consequently, initial attempts focused on image segmentation and edge detection techniques. Image segmentation separates regions in an image into homogeneous areas where the pixels have similar properties. In this context, watershed, simple linear iterative clustering (SNIC), multi-threshold and multi-resolution segmentation have been investigated for field boundaries (Gorelick, 2020; Schultz et al., 2015; Waldner and Diakogiannis, 2019; Watkins and Niekerk, 2019a,b; Yan and Roy, 2014). One general problem here is the over- and under-segmentation of regions. Edge detection techniques such as the Sobel operator, Scharr operator or Canny edge have been compared for applications such as feature extraction or object detection in the past with the result that Canny edge detection achieves better results in comparison (Chandwadkar, 2013; Huang et al., 2017; Watkins and Niekerk, 2019a; Yellasiri et al., 2010). These algorithms detect edges to separate regions or objects in an image but suffer from noise such as false edges and incomplete boundaries (Chen et al., 2015; Watkins and Niekerk, 2019a). Hybrid approaches using region-based segmentation and edge detection were also investigated in order to benefit from the strengths of each category (Mueller et al., 2004; Rydberg and Borgefors, 2001). Following a simple approach, which eased implementation efforts and reduced noise, hybrid approaches were avoided. Canny edge shows good results compared to other edge operators. Nevertheless, noise hinders the application of Canny edge for field boundaries detection. The problem of noise is addressed by an index to reduce the information content and emphasises the field boundaries before applying Canny edge on each image. It is also assumed that the use of multiple observations strengthens the field boundaries as in the case of crop-type mapping. This simplified procedure was a first experimental attempt to cover all necessary aspects of object-based yield mapping at the field level.

1.5 Winter wheat yields at the field level

In a constantly changing environment due to climate change and growing demand for food, the development of intelligent approaches to optimise resources and yields is essential. Yield predictions provide a basis for various applications and are necessary for international organisations, farmers or financial institutions. Yield predictions relate to the following areas:

- Management zones
- Optimisation of resources (fertiliser, water, pesticides)
- Food security
- Food supply chain
- Forecast of yields
- Futures

In the past, various solutions have been proposed for yield prediction. A main focus of this work is the implementation of a practical and efficient solution that is cost-effective and can be used worldwide. For this reason, satellite-based research projects are considered that differ in terms of spectral information, resolution or satellite information used to explain different crop yields. Independent of the investigated crop type, parameters such as water need, nitrogen supply and climatological information are essential and influence the grain yield. Crop simulation models such as World Food Studies (WOFOST) are a proven methodology (Basso and Liu, 2018; Pan et al., 2019) as well as the incorporation of climatological data from nearby stations (Albers et al., 2017; Bolton and Friedl, 2001; Chen et al., 2004; Heil et al., 2020; Lobell et al., 2006; Schlenker and Roberts, 2009; Shi et al., 2013; Zhao et al., 2017). In general, past research activities differ between physical, empirical and hybrid approaches (Basso and Liu, 2018; Peng et al., 2020a,b; Shelia et al., 2019). The application of climatological data is one of the most used and simplest procedures whereby precipitation, temperature and solar radiation are the most important parameters. Some climatological parameters correlate with each other which

can lead to model overfitting if no additional restrictions can be made. Bolton and Friedl (2001) proposed evapotranspiration as an input variable to fuse climatological data and avoid overfitting. However, the climatological data only accounts for a part of the yield variance and is not suitable for yield maps at the field level. One of the first satellite-based yield applications have been based on MODIS data which provides a moderate resolution of up to 250 metre per pixel and support yield prediction on a regional or national scale (Bolton and Friedl, 2013; Doraiswamy et al., 2003; Liang et al., 2004; Tadesse et al., 2015a; Wang et al., 2018). For instance, Bolton and Friedl (2013) predicted maize yields in non-semi-arid areas and found out that the enhanced vegetation index ($EVI2$) gave the best results and explained around 67% of the yield variance. The authors also mention that the normalised difference water index ($NDWI$) is sensitive to watering and performs well in semi-arid regions. An index explains a plant-specific or yield-relevant characteristic by establishing a relationship between different wavelengths. Serrano et al. (2019) also applied the $NDWI$ and found high correlations with soil moisture and biomass productivity. To get an overview of regional developments, MODIS is an adequate data source but PF needs to cover the heterogeneity of fields. The availability of Landsat data enabled yield prediction at the field level, but Landsat provides only a few images per vegetation period. This changed with the Sentinel mission which provides a high temporal coverage for every location worldwide and specifically enables precision farming applications (Escolà et al., 2017; Skakun et al., 2019). Yield predictions at the field level are very ambitious as the relationship between soil, water, nitrogen and climatological data needs to be addressed. Therefore, it is important to learn the relationship between yield-relevant observations also in years with weather anomalies or varying nitrogen supplies. In the past, mainly indices or climatological data were used, but this research study focuses on water to explain winter wheat yields at the field level. The performance of indices and climatological data were additionally verified. The presented overview in section 1.2 is key to find a methodology which can be used for monitoring of the crop water demand. An evapotranspiration-based approach was chosen as it combines climatological and satellite data and tracks the daily crop water requirements (CWR) of different plants. The efficiency of this approach was also verified for irrigation management by recent research studies (Alface et al., 2019;

Argolo dos Santos et al., 2020; D'Urso and Belmonte, 2006; Vuolo et al., 2015a,b). This is an important confirmation for water demand measurements, since it has already proven its usefulness in form of a practical use case. The key here is simplicity and efficiency. Other studies that include water demand for yield prediction focus on energy balance models such as METRIC or SEBAL. Several authors (Awad, 2019; Khan et al., 2018; Tadesse et al., 2015a) emphasised the usefulness of actual evapotranspiration, but also stressed the issue of Landsat data availability. This problem does not occur with the approach used in Section 2.2.2 because it does not require land surface temperature. This Penman-based CWR also considered other indices like the normalised difference red edge index ($NDRE$), red edge inflection point ($REIP$) and $NDWI$ as K_c factor. $NDRE$ and $REIP$ strongly correlate with the LAI index and are thus more flexible, as they do not need to be calibrated (GAO et al., 2017; Herrmann et al., 2011; Lilienthal, 2014). LAI is a derived index based on empirical or physical evaluation (Asam, 2015; Revill et al., 2020). However, this makes the application in different climate zones or for different crops more difficult. Secondly, $REIP$ and $NDRE$ do not saturate as fast as $NDVI$. And most important, $REIP$ and $NDRE$ correlate with nitrogen content (Lilienthal, 2014; Zhang et al., 2019). The incorporation of observations concerning nitrogen and water makes it possible, on the one hand, to cover the most important features and, on the other hand, to treat the most important yield features in a direct and physical way.

1.6 Objectives and outline of the thesis

In summary, this work addresses key issues for yield prediction at the field level, crop-type and field boundary classification. The question arises how this three topics are related to each other. Yield prediction at the field level has not much been addressed in the past due to the availability of high resolution data. Supervised learning methods need labeled data such as field borders, crop types or yield records. Object-based yield prediction at the field level needs field boundaries and the corresponding crop type to apply a trained model. For example, if it is necessary to predict the yield of winter wheat fields in a region of South Africa, the field boundaries must first be identified, followed by the classification of winter wheat to specifically predict the yield of these fields. Therefore, the following questions will be addressed:

- Which input features are important for winter wheat yields ?
- To what extent does the temporal resolution of time series (monthly/weekly) influence the prediction?
- Which influence has the processing level of Sentinel-2 images ?
- To what extent do weather anomalies influence the results ?

Section 2 introduces all sites in Bavaria and collected data sets for the investigations with field borders, crop types and yield predictions, followed by section 3, which presents all results in detail. The presented results for yield prediction include a detailed comparison of various configurations and input features. Section 4 discusses the results and open questions and stresses further needs.

2 Material and methods

2.1 Crop types and field boundaries

2.1.1 Study site

All the results presented are based on study sites in Bavaria. Depending on the application, there were differences in the amount of data used for crop-type or yield prediction. The study area for crop-type mapping is the whole of Upper Bavaria, which comprises about 7875 square kilometres of agricultural land (LfStat, 2017). The crop types investigated were maize, winter wheat, winter barley, winter rapeseed, sugar beet, and potato. Some experiments were performed with an additional rejection class (Other), which covers those plant types not considered. Figure 2.1 summarises the most important characteristics such as temperatures, monthly precipitation and crop phenology. Figure 2.2 shows the validation area with 301 fields. The average annual temperature in Bavaria is 8.6 °C with an average precipitation of 811 mm. The measured climatological data in section 2.2.1 differ strongly from the annual average values, because they were determined for the vegetation period from the beginning of March to the end of July. Crop-type mapping also focuses on the vegetation period, but from the beginning of February to the end of August for the years 2016, 2017 and 2018. 2018 was characterised by unusually high temperatures and drought, while 2016 and 2017 were characterised by rather similar climatic conditions. The high temperatures and the drought in 2018 influenced the development of the crops as well as the spectral fingerprint. Table 2.1 provides an overview about the fields for field boundary and crop-type classification. Crop-type mapping was trained and validated using 2400 samples, while 301 samples from an area near Freising in Germany were used to identify field boundaries. 2099 fields were randomly selected from all parts of Upper Bavaria, and 301 adjacent fields from one region were used for validation and

field boundaries. The corresponding ground truth data with all the field borders and crop types for all years were provided by the Bavarian State Ministry of Agriculture and Forestry (StMELF).

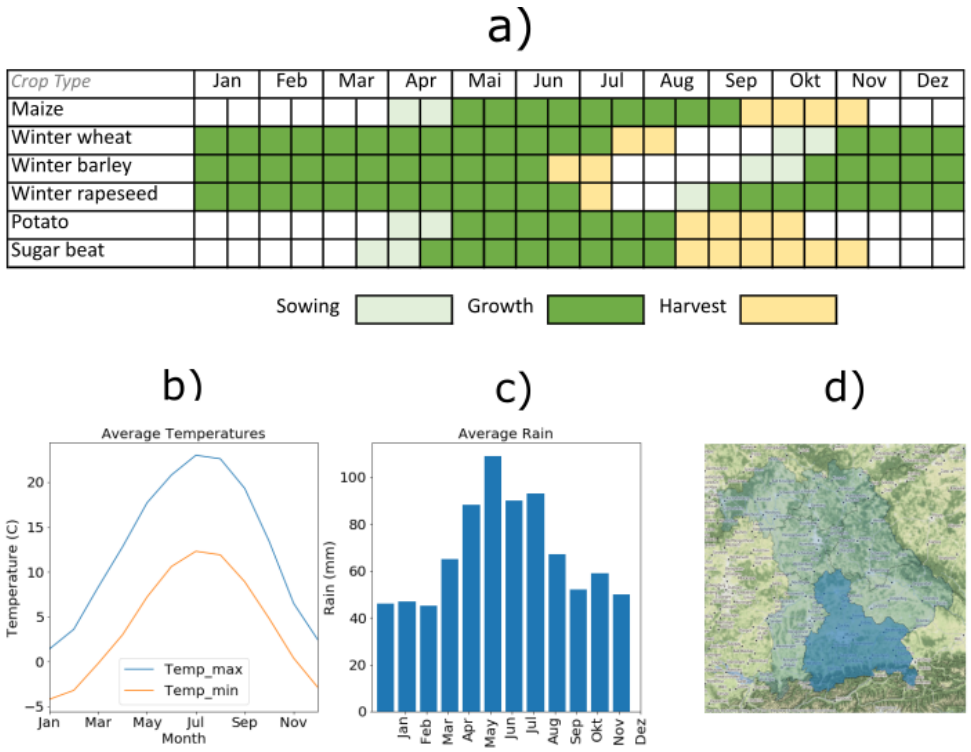

Figure 2.1: Climate overview and crop phenology of the test sites in Upper Bavaria. Figure a) shows the crop phenology with the sowing period in lime green, the vegetation period in darker green and the harvest period in yellow. Figures b) and c) show the average monthly maximum and minimum temperatures and precipitation. Figure d) highlights the area of Upper Bavaria in Bavaria under investigation. The fields in Upper Bavaria were randomly chosen to cover the whole area.

Table 2.1: Overview of samples for crop-type classification and field boundaries. Data for 2018 includes additional 301 samples to visualise crop-type mapping in one region.

	Crop Types	**Field Boundaries**
2016:	699	0
2017:	700	0
2018:	700 + 301	301

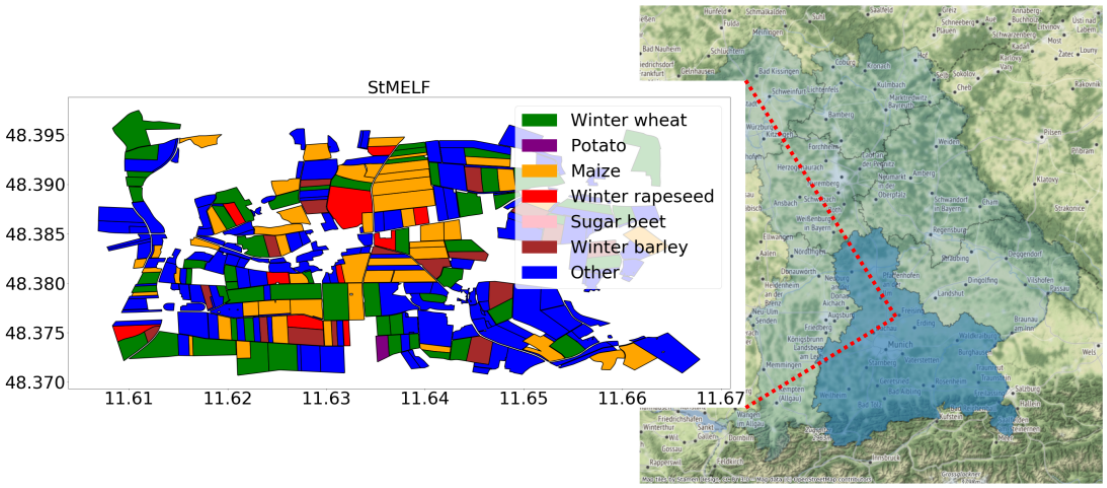

Figure 2.2: Coherent area near Dürnast in Upper Bavaria with 301 fields and corresponding decimal latitude and longitude coordinates, which were used to validate the field boundaries and crop types.

2.1.2 Crop-type processing

The processing chain for crop-type mapping is illustrated in Figure 2.3. It shows the necessary data inputs from OpenStreetMap (OSM), Sentinel-2 and StMELF, the pre-processing and classification based on support vector machine (SVM) and random forest (RF) (Biau and Scornet, 2016; Cortes and Vapnik, 1995; Cristianini and Shawe-Taylor, 2000). By using OSM, it is possible to remove non-relevant areas such as water bodies, forests, buildings or roads. The pre-processing includes the application of the $NDVI$ standard deviation, which indicates whether a pixel has changed over time. For example, water bodies or buildings hardly change over time, while vegetation shows a high temporal variance. The StMELF data consists of field boundaries and crop types in Bavaria for every year and were applied to the training and testing of both classifiers.

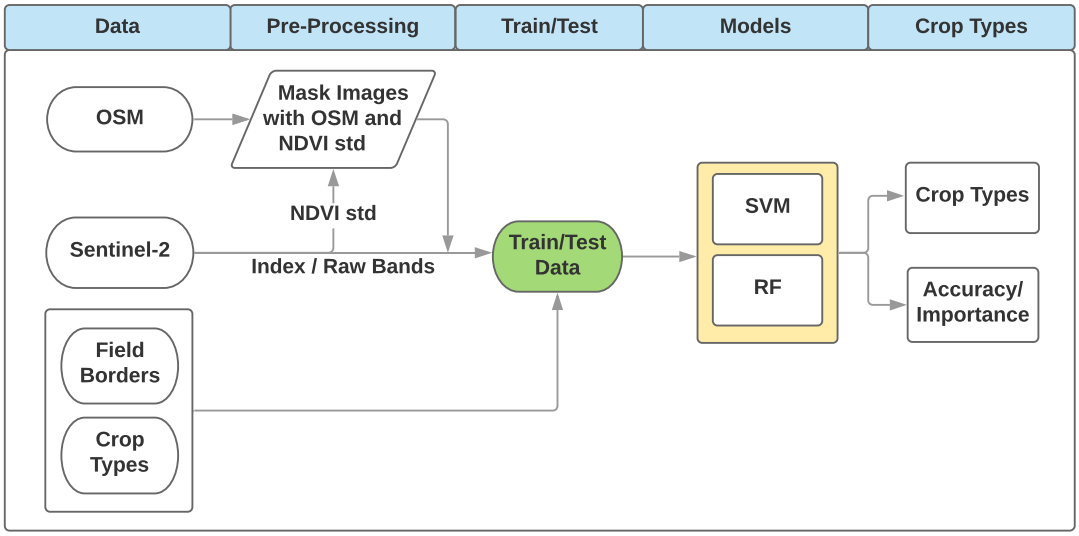

Figure 2.3: Overview of the processing of crop types with their input data and processing steps.

2.1.3 Field boundaries processing

The detection of field boundaries is an important step towards object-based crop-type mapping and yield prediction when official field borders are not available. Figure 2.4 introduces an unsupervised learning approach based on Open Computer Vision (OpenCV) and Canny edge detection (Bradski, 2000; Xu et al., 10/20/2017). Google Earth Engine (GEE) and OpenCV include the Canny edge algorithm, but the presented approach applies the GEE-based Canny edge detection to each image in a collection and outputs the sum of all Canny edge images as an image which in turn is processed with OpenCV. Gaussian blurring, image conversion or finding contours are supported by OpenCV. The recognised contours are processed into geo-referenced polygons and masked with OSM data to remove any irrelevant objects.

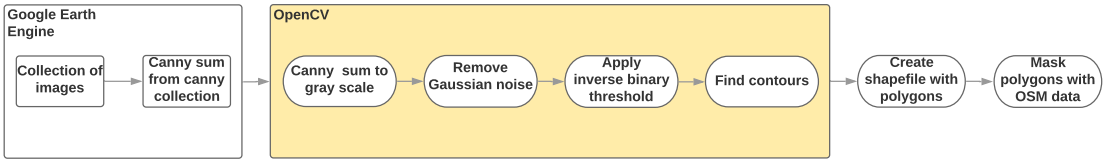

Figure 2.4: GEE, Canny edge detection and OpenCV pipeline for field boundary detection.

2.1.4 Metrics

Overall accuracy (OA), user accuracy (UA), producer accuracy (PA) and Kappa statistics have been applied for the evaluation of the classification performance (Humbold State University, 2020). Overall accuracy and Kappa evaluate the classification of all crop types, while PA and UA consider each crop type. OA is expressed by correctly classified crops divided by all reference crops. The Kappa coefficient ranges from 0 to 1, whereby 1 stands for a perfect classification result with ground truth. PA represents a measure of how well the ground truth data are classified while UA considers the classification reliability. It shows whether the classification has erroneously assigned other classes to a class and thus the classification does not match ground truth. Scikit-learn (Pedregosa et al., 2012) contains all the metrics presented, as well as algorithms such as SVM and RF. The Interception over Union (IoU) is additionally used for field boundary evaluation. It describes the area of overlap divided by the area of union.

2.2 Winter wheat yield prediction

2.2.1 Study site

The study regions are located in Upper Bavaria and in Upper Palatinate in Southern Germany. The most important crop types are winter wheat, maize, barley, rapeseed, sugar beet, and potato. In this study, winter wheat was chosen which is sown at the beginning of October and harvested at end of July or beginning of August. The average temperatures for the vegetation period and the investigated sites are indicated in Table 2.2, which shows increasing temperatures from 2016 to 2018. Considering the annual average, Bavaria has a mean temperature of 8.6 °C and a mean precipitation of 811 mm. In the three regions 121 winter wheat fields were selected with different sizes, visualised exemplary as georeferenced polygons in Figure 2.5. Six yield measurements for 2018 from a combine harvester were additionally used and aggregated to mean values.

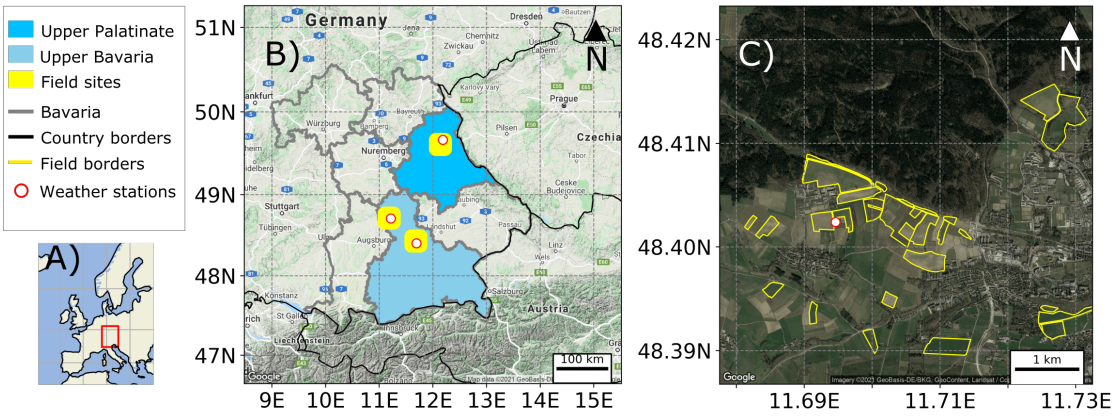

Figure 2.5: Winter wheat yields and corresponding field borders in WGS84 (EPSG:4326) where A) shows the location of Bavaria in Europe, B) depicts the investigated three regions where actual yields were determined from 2016 to 2018, and C) visualises the selected field sites in one test region near Dürnast in Upper Bavaria (Germany).

Table 2.2: Overview of yield and climatological data with their mean values (μ) and standard deviation (σ) from the beginning of March to the end of July, 2016 - 2018.

	2016	**2017**	**2018**
μ Temperature (^{o}C):	12.0	12.6	13.3
μ Precipitation (mm):	314.4	294.2	302.3
Number of Fields:	43	48	30
μ Yield (dt ha^{-1}):	84.9	77.9	70.9
σ Yield (dt ha^{-1}):	10.6	12.3	12.0

Table 2.2 lists the mean yield values and standard deviations with the highest yields obtained in 2016 (84.9 dt ha^{-1}) and the lowest in 2018 (70.9 dt ha^{-1}). We considered the vegetation period from the beginning of March to the end of July in 2016, 2017 and 2018. Yields determined in 2016 were above-average compared to Bavarian-wide region values amounting to 72.3 dt ha^{-1} (StMELF, 2020). All yields were weighed gravimetrically directly after threshing. Grain moisture content was determined and expressed as standard value of 14% for all yields. In 2018, we further collected six additional averaged field yields using a combine harvester. Figure 2.6 indicates the corresponding average temperatures and precipitation on a weekly basis as an average

value for all fields. For this purpose, climatological data were retrieved from the nearest weather station to each field. Especially noticeable is the temperature trend in April and early May in 2018, which was above average. The amount of precipitation was quite comparable in all years, but differed significantly between months. Figure 2.6 shows that the precipitation in spring 2018 was below average. The soil types are heterogeneous and include loamy sand, sand, gravel, loam, half-bog, and clay. Figure 2.7 visualises winter wheat yield distributions for all years and indicates the amount of nitrogen applied.

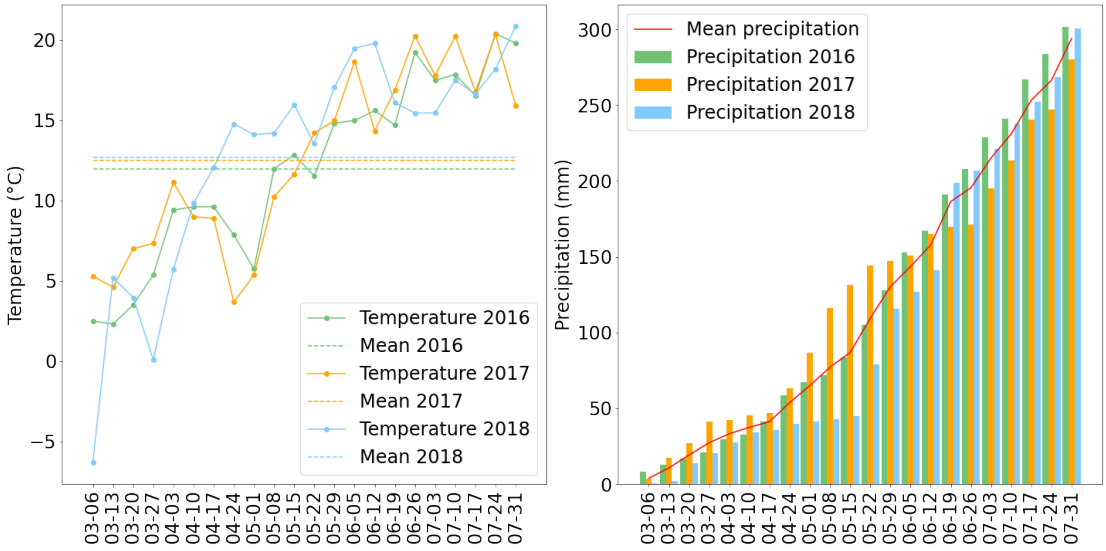

Figure 2.6: Aggregated average temperature (°C) and cumulative precipitation (mm) in weekly resolution from March to July.

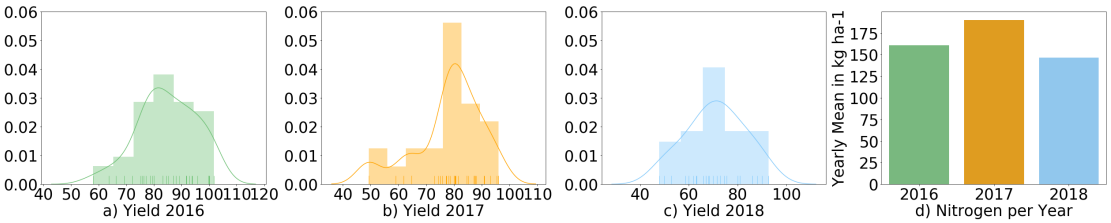

Figure 2.7: (a-c) Frequency of winter wheat yield distributions (dt ha^{-1}) and d) amounts of N applied (kg ha^{-1}) in the years 2016, 2017, and 2018.

2.2.2 Climatological data and evapotranspiration

Climatological data and ET are essential for yield prediction as the availability of water is one of the most important factors influencing yield. ET is used for irrigation control and can be customised using satellite data for plant-specific applications (Allan et al., 1998; Vuolo et al., 2015b). All climatological data were downloaded from nearby weather stations from the German Weather Service (DWD), which provides all data free of cost. The corresponding three weather stations are visualised in Figure 2.5 and vary in distance from 0.23 km to a maximum of 13.77 km to the fields in the target region. The downloaded measurements included hourly maximum and minimum temperature in degrees Celsius (°C), wind speed ($\mathrm{km\,h^{-1}}$), precipitation (mm), dew point (°C), cloud cover (%), sunshine (min), relative humidity (%) and air pressure (hPa). The estimated solar radiation R_s is based on the Hargreaves radiation equation and uses the maximum and minimum temperature as input where R_a stands for the extra-terrestrial radiation (Eq.(2.1)).

$$R_s = 0.16\sqrt{(T_{\max} - T_{\min})R_a} \quad (\mathrm{MJ\,m^{-2}\,d^{-1}}) \tag{2.1}$$

Wind speed (v) was converted into metres per second at 2 m above ground because the DWD measures the wind speed at a height (h) of 10 metres above the ground (Eq.(2.2)).

$$v_{2\mathrm{m}} = \frac{v_h 4.87}{\log(67.8h - 5.42)} \quad (\mathrm{m\,s^{-1}}) \tag{2.2}$$

For the computation of daily ET values, all climatological measurements were re-sampled to daily values. The Penman-Monteith method (FAO-56) was applied, which determines the reference evapotranspiration ET_0 via Eq. (2.3).

$$ET_0 = \frac{0.408\Delta(R_n - G) + \gamma\frac{900}{T + 273}u_2(e_s - e_a)}{\Delta + \gamma(1 + 0.34u_2)} \tag{2.3}$$

The difference between net radiation R_n and soil heat flux density G is described by $\Delta(R_n - G)$ ($\mathrm{MJ\,m^{-2}\,d^{-1}}$). The difference $(e_s - e_a)$ between saturation and actual vapour pressure (kPa) is multiplied by wind speed u_2 at 2 m height. T stands for the mean temperature at 2 m above ground and is computed by the maximum and minimum

temperature records. The reference evapotranspiration assumes a plant height of 0.12 m, a surface resistance of 70 s m^{-1} and an albedo of 0.23, since it assumes grass as hypothetical reference plant. A detailed description can be found in publications by the Food and Agriculture Organisation of the United Nations (FAO) (Allan et al., 1998; FAO, 2020). The minimum required climatological data for the calculation of ET_0 values are maximum and minimum temperatures, wind speed and relative humidity. Additional parameters improve the performance of the model, but experiences has shown that reliable results can be obtained with this basic information. To accommodate for physiological differences of plants, a plant-specific adaptation of ET_0 is required. The K_c coefficient can be calculated by ET_c/ET_0. If the measured plant evapotranspiration is not available, FAO recommends the adjustment using previously determined constants per crop (Allan et al., 1998; FAO, 2020). Therefore, the mean index value for each field and observation was adopted as the K_c factor for monitoring plant growth (Eq.(2.4)). The mean value is the aggregated mean value over all pixels within a field, which was rescaled between 0 and 1.15. FAO recommends to use a maximum value of 1.15 as K_c factor for winter wheat. To avoid negative values, 0 was chosen as minimum. The rescaling is important because indices have different value ranges.

$$K_c \in \{ \mu NDVI, \mu NDWI, \mu REIP, \mu NDRE \} \tag{2.4}$$

The final crop evapotranspiration equation (Eq.(2.5)) is a multiplication of the satellite-based K_c factor with the evapotranspiration ET_0:

$$ET_c = K_c \cdot ET_0 \quad \text{(mm)} \tag{2.5}$$

The daily difference between ET_c and precipitation (P) for every field was calculated to estimate the daily cumulated crop water requirement (CWR) (Eq.(2.6)) as follows:

$$CWR = \sum_{i=0}^{N} (\Delta_i) \quad \text{(mm)} \tag{2.6}$$

where:

$$\Delta_i = ET_c - P \tag{2.7}$$

ET_0, ET_c, Δ_i (Eq.(2.7)) and CWR were computed for each field and daily from the beginning of March until the end of July. The presented variables, climatological data and satellite observations were used for the evaluation using linear regression and random forest.

2.2.3 Parametrisation

The calculations were performed using stepwise linear regression and random forest. Stepwise LR included features if $p < 0.01$ and excluded them with $p > 0.05$. RF was parametrised with $n\_estimators = 300$, $max\_depth = 100$, $max\_features = sqrt$ and $J = 984$. The training and test sizes were 80% and 20%. All independent variables (features) were standardised, so that the distributions had 0 as mean value and 1 as standard deviation. Cross-validation (CV) was performed with ShuffleSplit where $n\_splits = 4$ and $test\_size = 0.2$. All methods and metrics were part of scikit-learn (Pedregosa et al., 2012).

2.2.4 Metrics

The model accuracy is based on R^2, mean absolute error (MAE) and root mean square error ($RMSE$), which are typical metrics for continues variables (Chai and Draxler, 2014; Moriasi et al., 2015). R^2, or the coefficient of determination, is a measure of how much a model explains the variance of the target variable. MAE determines the absolute difference between prediction and actual measurement or observation. $RMSE$ is often used for accuracy determination and is the square root of the mean square error. The square root thus reduces the effect of large errors. MAE and $RMSE$ evaluate the model error in the units of the target variable ($\mathrm{dt\,ha^{-1}}$), which is important for the evaluation and comparison with other research studies. Equations 2.8, 2.9 and 2.10 express the described statistical measures described with y_i for the i-th real observation and corresponding prediction $\hat{y}$.

$$R^2(y, \hat{y}) = 1 - \frac{\sum_{i=1}^{N}(y_i - \hat{y})^2}{\sum_{i=1}^{N}(y_i - \bar{y})^2} \tag{2.8}$$

$$MAE(y, \hat{y}) = \frac{1}{N} \sum_{i=1}^{N} \mid (y_i - \hat{y}) \mid \tag{2.9}$$

$$RMSE(y, \hat{y}) = \sqrt{\frac{1}{N} \sum_{i=1}^{N} (y_i - \hat{y})^2} \tag{2.10}$$

2.3 Description of the satellite data for the respective application

The Sentinel mission with its various satellites, high temporal coverage and free optical and radar-based data enables advances in precision farming. This study required data from Sentinel-2A and Sentinel-2B, which together provide multi-spectral data every 2-5 days. The availability depends on the cloud cover and the latitude of the site. Bavaria is at a latitude where data is available approximately every three days. Both satellites provide multi-spectral data with 13 available bands. Sentinel-2A was launched in June 2015, followed by Sentinel-2B in March 2017 to achieve a high revisit time. This is also the reason for a lower data availability until early April 2017. Table 2.3 summarises all bands and wavelengths. Bands 2, 3, 4, and band 8 have a resolution of 10 m per pixel while band 11 and 12 cover the SWIR frequencies and have a resolution of 20 m per pixel. Bands 10 and 9, with a resolution of 60 m per pixel, respond to water vapour and cirrus clouds and can be used for cloud detection (GEE, 2012). Table 2.3 lists five indices that are evaluated and compared in this study. The $NDVI$ (Rouse et al., 1974) is a good proxy and provides information on biomass, plant health and canopy chlorophyll content. It is widely used for irrigation, yield prediction or nitrogen management. However, it also has its disadvantages, as it quickly saturates when the biomass becomes dense. The $NDRE$ (Barnes et al., 2000) can also be used to detect the leaf chlorophyll content, plant health, the nitrogen status and fertiliser needs. Nitrogen uptake is a crucial yield-determining factor, why we also included the $REIP$ index (Guyot et al., 1988) which delivered significant results in past research studies. The $NDWI$ (Gao, 1996) is related to the canopy moisture content or water accumulations and is traditionally used for

drought monitoring. All satellite data have been downloaded from Google Earth Engine (GEE) (GEE, 2020; Gorelick et al., 2017) which provides a JavaScript and Python API to access and process terabytes of various satellite data. Sentinel-2 data is categorised by the processing level. There is a Level-1C product, delivering top-of-atmosphere (TOA) reflectance images and a Level-2A product with bottom-of-atmosphere (BOA) reflectance information. GEE processes the Level-1C product to BOA reflectance images with the European Space Agency's Sen2Cor open-source processor (Main-Knorn et al., 2017). Level-2A data are not available on GEE for our considered period, especially for 2016 and early 2017. We processed therefore the Level-1C product to BOA images using Py6S (Py6S, 2020). Both products, Level-1C and Level-2A, were evaluated for yield prediction, but only Level-1C was used for crop-type and field boundaries mapping. Figure 2.8 compares the reflectance values for a field and the vegetation period in 2017. It is evident that clouds introduce high noise in form of increased reflectance values. Cloudy pixels within a polygon or field are not so obvious to detect, why we used a Python framework (Sentinel Hub, 2020) for cloud filtering. This way, it was possible to minimise the noise for yield prediction. Nevertheless, we found in a preliminary study, that the usage of the scene cloud filter, provided by GEE, is acceptable for some applications, and that noise introduced by clouds can be partially processed.

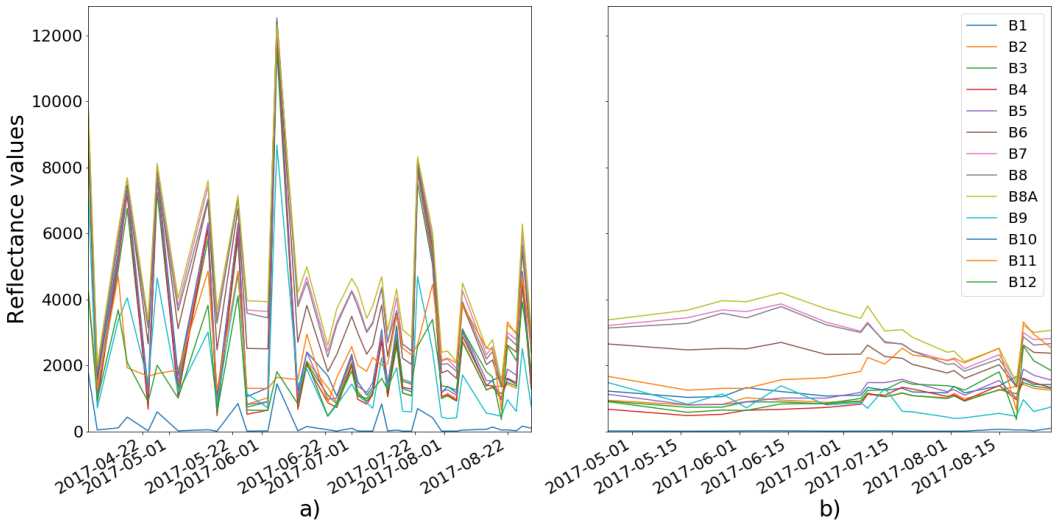

Figure 2.8: Comparison of reflectance values with a) clouds and b) filtered data of the indicated bands.

Table 2.3: Raw bands of Sentinel-2 and five vegetation indices evaluated in this study.

Band/Index	**Central Wavelength** (nm) **or Formula**	**Description**
Band 1	443.9 (S2A) / 442.3 (S2B)	Aerosol (60 m)
Band 2	496.6 (S2A) / 492.1 (S2B)	Blue (10 m)
Band 3	560 (S2A) / 559 (S2B)	Green (10 m)
Band 4	664.5 (S2A) / 665 (S2B)	Red (10 m)
Band 5	703.9 (S2A) / 703.8 (S2B)	Red edge (20 m)
Band 6	740.2 (S2A) / 739.1 (S2B)	Red edge (20 m)
Band 7	782.5 (S2A) / 779.7 (S2B)	Red edge (20 m)
Band 8	835.1 (S2A) / 833 (S2B)	NIR (10 m)
Band 8A	864.8 (S2A) / 864 (S2B)	NIR (20 m)
Band 9	945 (S2A) / 943.2 (S2B)	Water vapour (60 m)
Band 10	1373.5 (S2A) / 1376.9 (S2B)	Cirrus (60 m)
Band 11	1613.7 (S2A) / 1610.4 (S2B)	SWIR (20 m)
Band 12	2202.4 (S2A) / 2185.7 (S2B)	SWIR (20 m)
$NDVI$	$\frac{(B8 - B4)}{(B8 + B4)}$	Ratio of red to NIR
$NDWI$	$\frac{(B3 - B8)}{(B3 + B8)}$	Ratio of NIR to green
$NDWI$	$\frac{(B8 - B11)}{(B8 + B11)}$	Ratio of SWIR to NIR
$REIP$	$700 + 40 \cdot \frac{\frac{(B4 + B7)}{2} - B5}{(B6 - B5)}$	Red and red edge
$NDRE$	$\frac{(B8 - B5)}{(B8 + B5)}$	Ratio of red edge to NIR

Since the number of fields for crop types is very high and the processing of clouds represents an additional processing effort, not all clouds were filtered for crop-type mapping. Sentinel-2 data was downloaded from GEE with a filter of 20%. This filter (CLOUDY_PIXEL_PERCENTAGE) considers clouds in a complete Sentinel-2 scene. Field boundaries detection used a cloud filter of 2%. Crop-type mapping was investigated by $NDVI$ and raw bands. For each field and observation, the pixels were aggregated to a mean value to generate corresponding time series per field. This object-based approach was also used for yield prediction. A preliminary comparison of the effect of median, mean, maximum and minimum values was made with the result that mean values are suitable. The Sentinel-2 time series for yield prediction were resampled and linear interpolated to weekly and monthly values. The time series for crop-type mapping have a two-week temporal resolution. Data gaps were closed by linear interpolation. The polynomial interpolation was also verified in a previous study, but linear interpolation produced stable results.

3 Results

3.1 Crop-type classification

3.1.1 Comparison of crop-type classification using different methods

This section evaluates the influence of features on the classifier accuracy. A total of 2099 samples from the years 2016, 2017 and 2018 were used to evaluate the classifier performance and characteristics, with each crop class equally distributed. Additional and independent 301 field samples from 2018 and for one area were added to create crop-type images. The time series of all features are based on linear interpolation with a two-week temporal resolution from February to August. RF was evaluated using standard parameterisation and 1000 decision trees in the forest while SVM was parametrised with a linear kernel and C = 10. The accuracy evaluation is based on a test size of 25% and K-Fold cross validation with 5 splits. Table 3.1 shows an overview of the tests performed. The corresponding confusion matrices can be found in the appendix (section B.1 and B.2).

Table 3.1: Overview of the crop classification results based on overall accuracy (OA). The SVM and RF performance was evaluated with $NDVI$, all raw bands and without the "Other" rejection class.

	$NDVI$	**Bands**	**Without "Other"**
SVM:	70%	87%	90%
RF:	75%	88%	92%

In summary, SVM and RF performed equally well. RF was able to provide slightly better results and can improve these results with hyperparameter optimisation, but standard parameters were used for comparability. $NDVI$ achieved significantly lower accuracies than raw bands. The rejection class has the advantage that it covers crops that were not considered but it also affects the accuracy. Table 3.2 and Table 3.3 show the confusion matrix for SVM and RF based on raw bands and without the rejection class. Figure 3.1 evaluates the feature importance of the best RF model indicating that the reflectance values for May and band 6 were most important. Figure 3.2 and 3.3 visualise the crop-type maps, classified with the best RF models. The images are based on the additional and the independent 301 crop samples near Dürnast in 2018. Using the "Other" class reduced the OA to 78%, while 96% was achieved without the rejection class. In particular, winter barley, winter wheat and winter rapeseed were falsely classified or not differentiated. Here the multi-temporal approach showed a weakness, because winter rapeseed was clearly distinguished in spring, but showed a similar time trend as winter wheat and winter barley from June onwards (see 3.4).

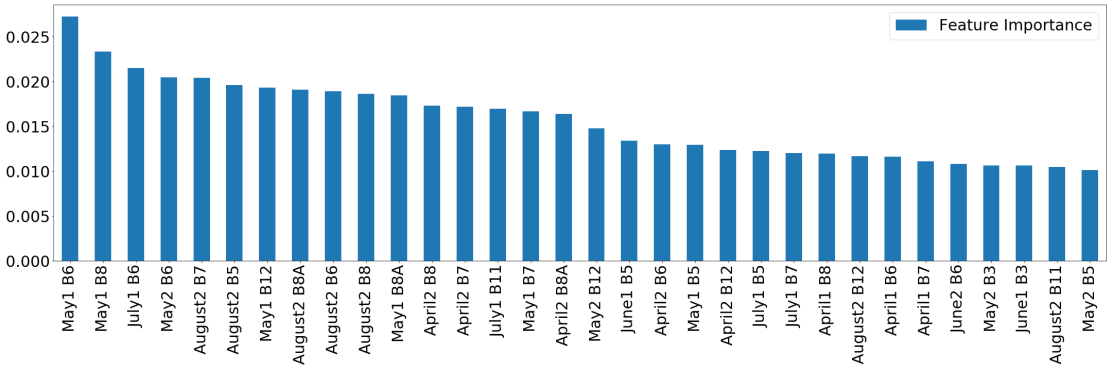

Figure 3.1: Most important features of the model for 2016-2018 and without the "Other" class.

Table 3.2: Classification with SVM, all raw bands and without the "Other" rejection class.

	Winter wheat (WW)	Winter barley (WB)	Winter rapeseed (WR)	Maize	Potato	Sugar beet (SB)	Total	UA (%)	PA (%)	
WW	61	2	3	2	1	0	69	88.41	87.14	
WB	8	62	4	1	0	0	75	82.67	91.18	
WR	1	3	78	3	1	0	86	90.7	91.76	
Maize	0	0	0	73	6	1	80	91.25	90.12	
Potato	0	0	0	1	56	4	61	91.8	84.85	
SB	0	1	0	1	2	75	79	94.94	93.75	
Total	70	68	85	81	66	80	450			
									OA	90%
									Kappa	0.95
									CV	0.91

Table 3.3: Classification with RF, all raw bands and without the "Other" rejection class.

	Winter wheat (WW)	Winter barley (WB)	Winter rapeseed (WR)	Maize	Potato	Sugar beet (SB)	Total	UA (%)	PA (%)	
WW	62	3	3	1	0	1	70	88.57	88.57	
WB	7	63	4	1	0	0	75	84	92.65	
WR	0	2	78	1	0	0	81	96.3	91.76	
Maize	1	0	0	76	3	0	80	95	93.83	
Potato	0	0	0	1	58	1	60	96.67	87.88	
SB	0	0	0	1	5	78	84	92.86	97.5	
Total	70	68	85	81	66	80	450			
									OA	92%
									Kappa	0.97
									CV	0.91

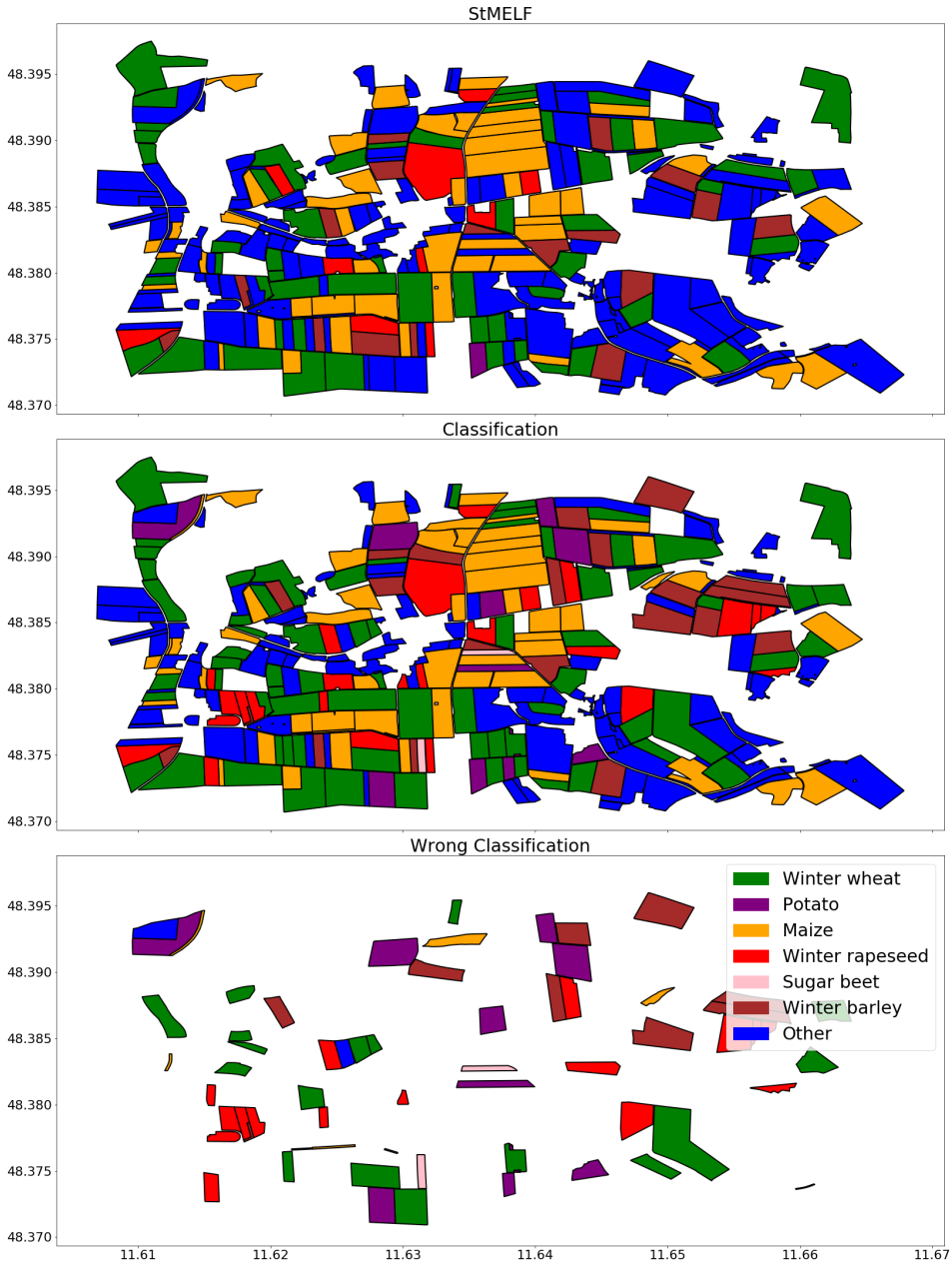

Figure 3.2: Classification with RF, all raw bands and the "Other" rejection class. Recorded crop types (ground truth data) of StMELF are shown in the first image. The classified crop types are shown in the second image while the last image visualises the falsely classified crops.

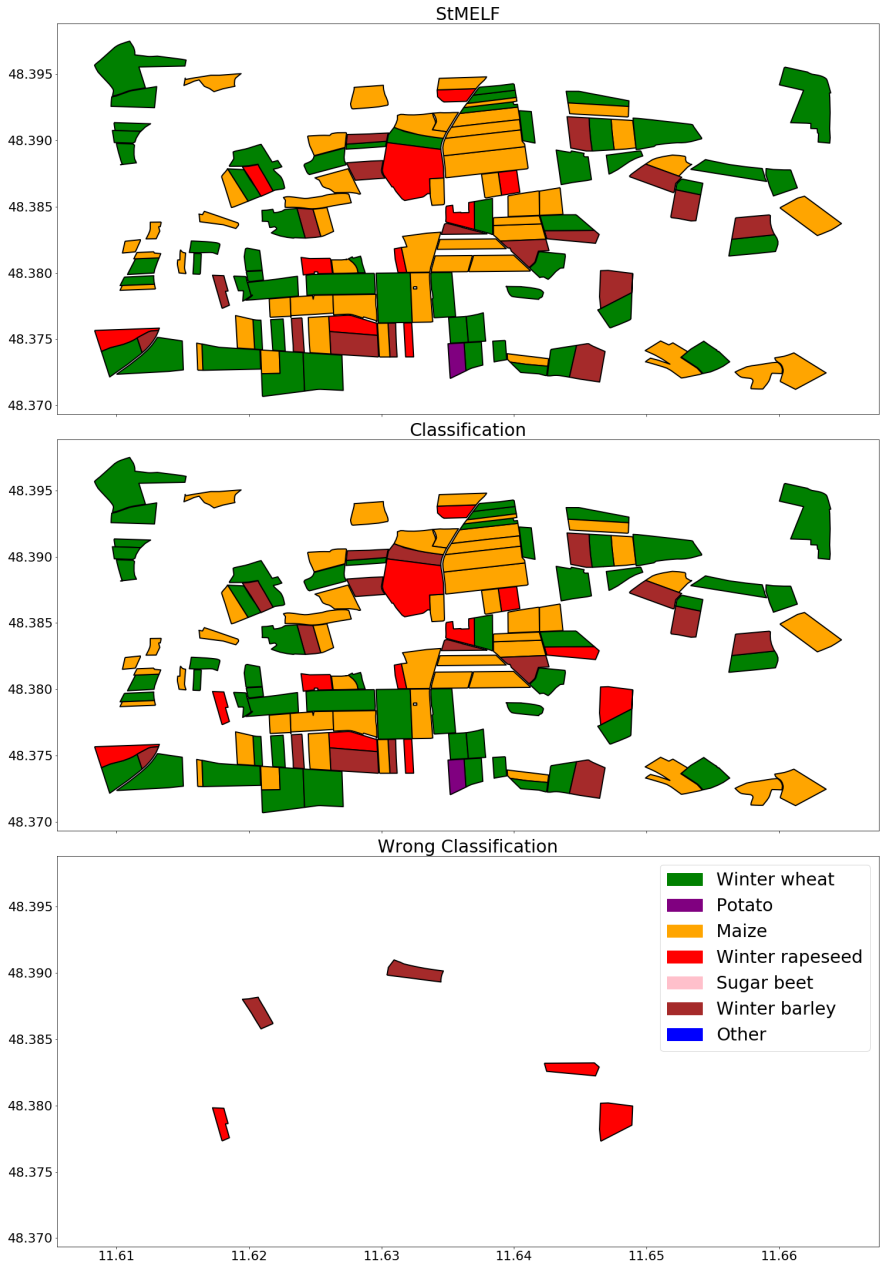

Figure 3.3: Classification with RF, all raw bands and without the "Other" class. Recorded crop types (ground truth data) of StMELF are shown in the first image. The classified crop types are shown in the second image while the last image visualises the falsely classified crops.

3.1.2 Crop-type prediction in a future year

The prediction of crop types in an unknown year and without labels is significant for practical uses. For this experiment, RF was trained with data from 2016 and 2017 to predict crop types in 2018. The year 2018 was a unique one, with above average temperatures and so it cannot be compared with earlier years. Figures 3.4 and 3.5 show the raw reflectance and $NDVI$ temporal patterns for each year. Although 2018 represents an anomaly, the temporal patterns are comparable and the crop types are separable. It should be emphasised that a small part of the clouds was allowed, which explains some of the peaks and misleading gradients in the images.

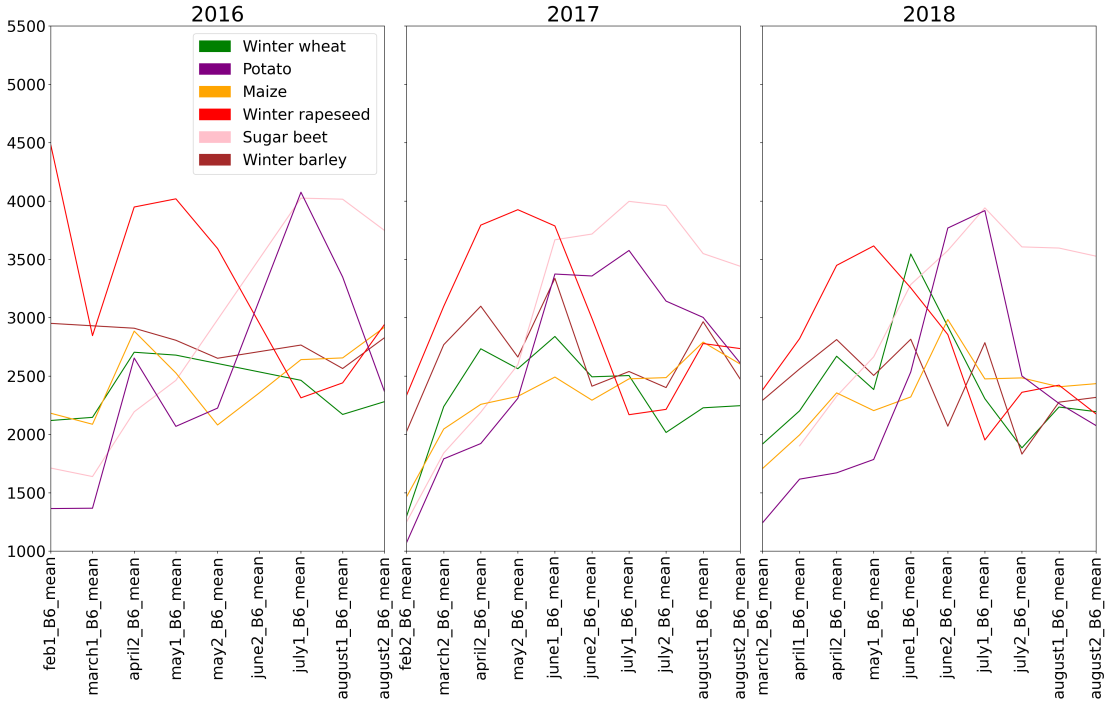

Figure 3.4: B6 mean temporal pattern for 2016, 2017 and 2018.

When evaluating Tables 3.4, 3.5, and Tables B.5, B.6 in the appendix, the high overall accuracies with RF are outstanding. SVM with a linear kernel is not reliable for predicting the crop types in 2018 (compare B.3). In contrast, RF achieves an overall accuracy of 79% with the rejection class and 80% without. Figures 3.6 and 3.7 show the application

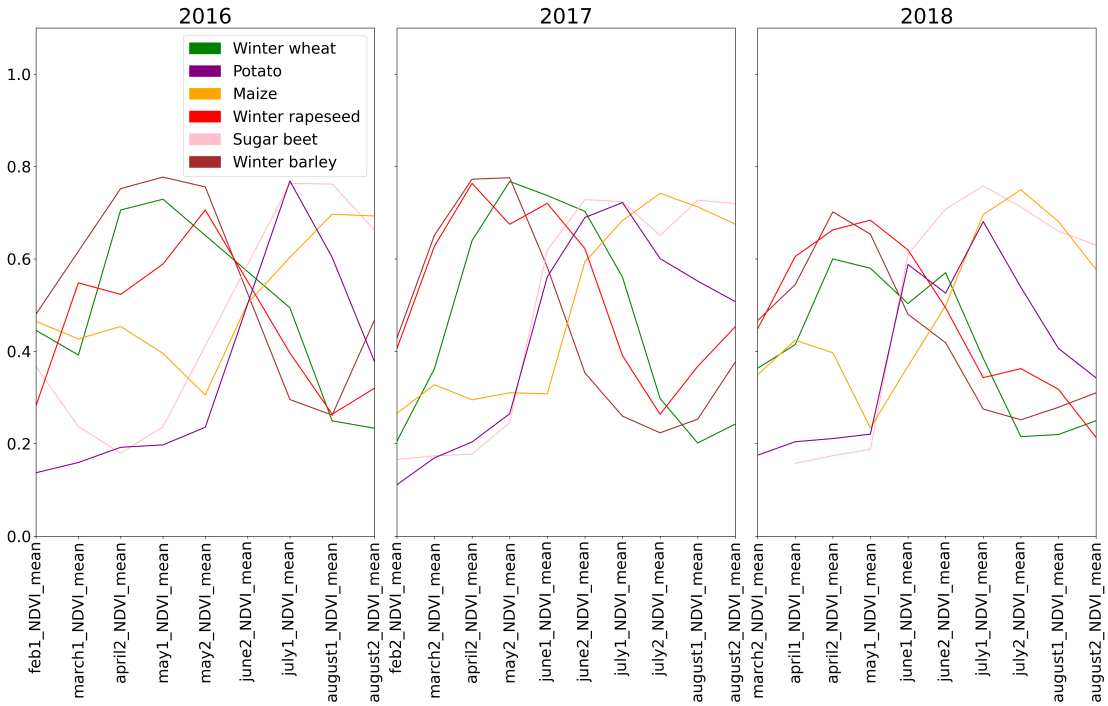

Figure 3.5: *NDVI* mean temporal pattern for 2016, 2017 and 2018.

of both models to the test area where an OA of 75% was achieved with the rejection class (and 86% without). The classification accuracies without labels from 2018 onwards are in the range of the accuracies with data from all the years concerned.

Table 3.4: Classification of crop types in 2018 with RF, all raw bands and the "Other" class. The model was trained with data for 2016 and 2017.

	Other	Winter wheat (WW)	Winter barley (WB)	Winter rapeseed (WR)	Maize	Potato	Sugar beet (SB)	Total	UA (%)	PA (%)
Other	78	9	16	1	4	0	0	108	72.22	78
WW	8	83	11	3	0	0	0	105	79.05	83
WB	3	4	67	1	0	0	0	75	89.33	67
WR	1	3	5	95	0	0	0	104	91.35	95
Maize	3	0	1	0	67	1	0	72	93.06	67
Potato	7	1	0	0	28	99	34	169	58.58	99
SB	0	0	0	0	1	0	66	67	98.51	66
Total	100	100	100	100	100	100	100	700		
									OA	79%
									Kappa	0.91

Table 3.5: Classification of crop types in 2018 with RF, all raw bands and without the "Other" class. The model was trained with data for 2016 and 2017.

	Winter wheat (WW)	Winter barley (WB)	Winter rapeseed (WR)	Maize	Potato	Sugar beet (SB)	Total	UA (%)	PA (%)
WW	85	20	5	1	0	0	111	76.58	85
WB	10	71	2	1	0	0	84	84.52	71
WR	3	5	93	0	0	0	101	92.08	93
Maize	0	2	0	69	1	0	72	95.83	69
Potato	2	2	0	28	99	34	165	60	99
SB	0	0	0	1	0	66	67	98.51	66
Total	100	100	100	100	100	100	600		
								OA	80%
								Kappa	0.94

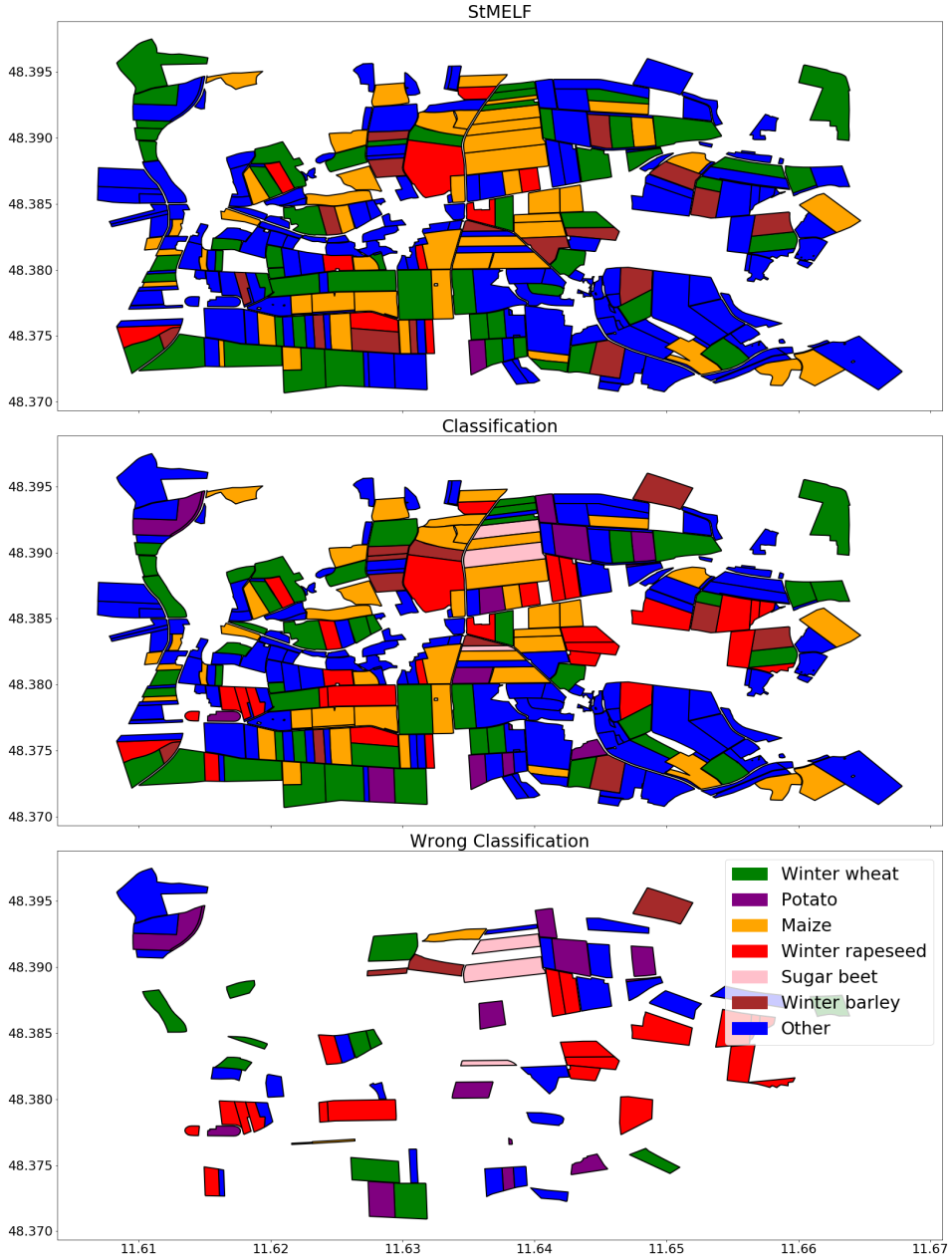

Figure 3.6: Crop types in 2018. The classification achieved an OA of 75% and is based on RF, all raw bands, the "Other" class and data from 2016 and 2017.

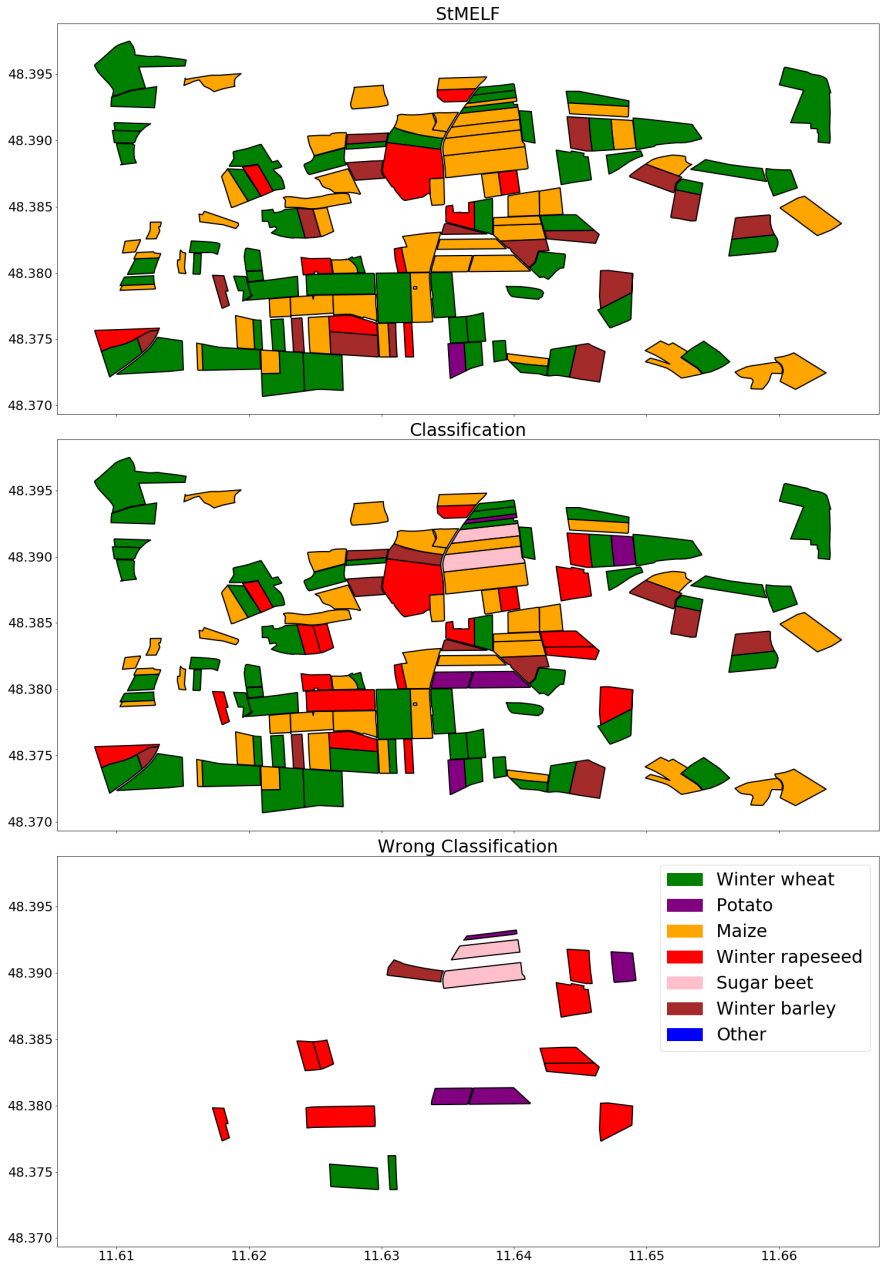

Figure 3.7: Crop types in 2018. The classification achieved an OA of 86% and is based on RF, all raw bands and does not include the "Other" rejection class. The trained model had no data of the crop type in 2018.

3.2 Field boundaries

Object-based approaches require field boundaries; therefore Canny edge was evaluated. RGB segmentation was firstly evaluated because humans recognise field boundaries in the same way. Secondly, a $NDWI$-based approach was used to reduce the noise introduced by RGB. Preliminary outputs of the processing pipeline presented in section 2.1.3 are shown in Figure 3.8 and Figure 3.9 for $NDWI$. A comparison of both figures reveals the advantage of $NDWI$ in relation to the reduction of irrelevant edges. $NDWI$ focuses on the field texture and reduces in-field edges. One image would produce insufficient results while the multi-temporal approach strengthens the edges from image to image. The Canny edge detection was parametrised with the mean over all pixels as threshold and sigma = 0.33. Roads, buildings, forests and lakes were masked using OSM. All the images in the multi-temporal stack were smoothed with bicubic resampling, since image resolution is an important success factor. The Sentinel-2 resolution is a limiting factor for the detection of small fields. Therefore, the use of bands with a resolution of 10 metres per pixel should be preferred. Figure 3.10 compares the polygons identified with recorded StMELF data. In the first tests with RGB and $NDWI$ an image stack from September 2017 to September 2018 was used to determine the field boundaries for 2018. Neighbouring fields with a similar or the same crop type could not be distinguished at the first attempt. Consequently, several fields were combined to form one field. However, this issue was overcome by using images that emphasise the contrast between the fields. This was achieved by using satellite images from the last autumn to May, since this avoids the vegetation period as much as possible, thus separating the same neighbouring fields, although over-segmentation is rarely introduced. It seems that some differences in soil texture cause this over-segmentation. This $NDWI$-based approach was validated and achieved an IoU = 0.7, a PA = 81% and a UA = 79%. UA is an important metric as it determines the reliability of the maps. In a previous work, SNIC was also evaluated (Lösch, 2019), but the images were over-segmented and therefore not applicable. Figure B.1 in the appendix shows a comparison of SNIC with the StMELF data basis.

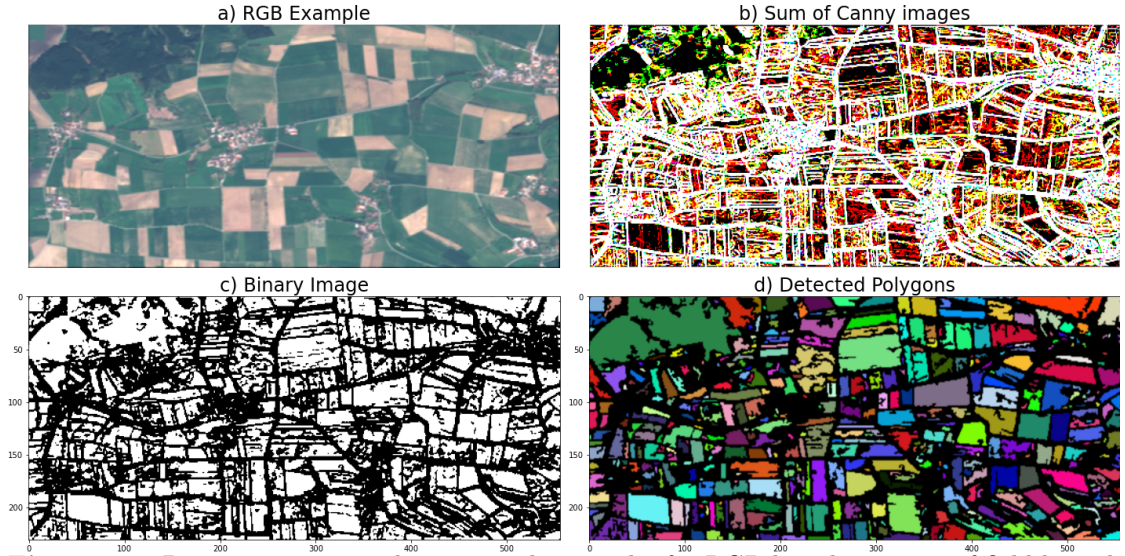

Figure 3.8: Processing steps and corresponding results for RGB-based mapping of field boundaries.

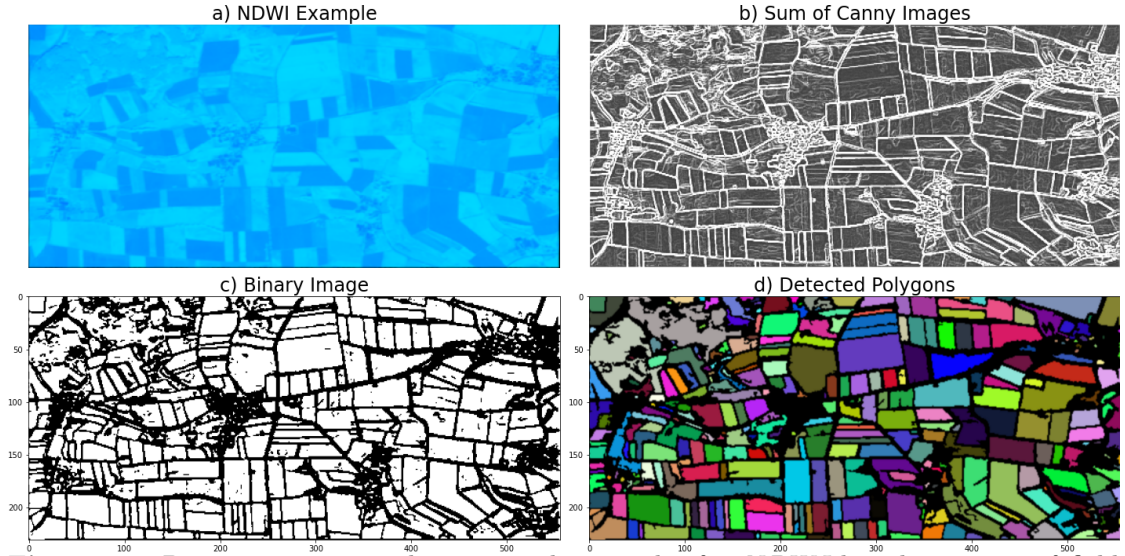

Figure 3.9: Processing steps and corresponding results for $NDWI$-based mapping of field boundaries.

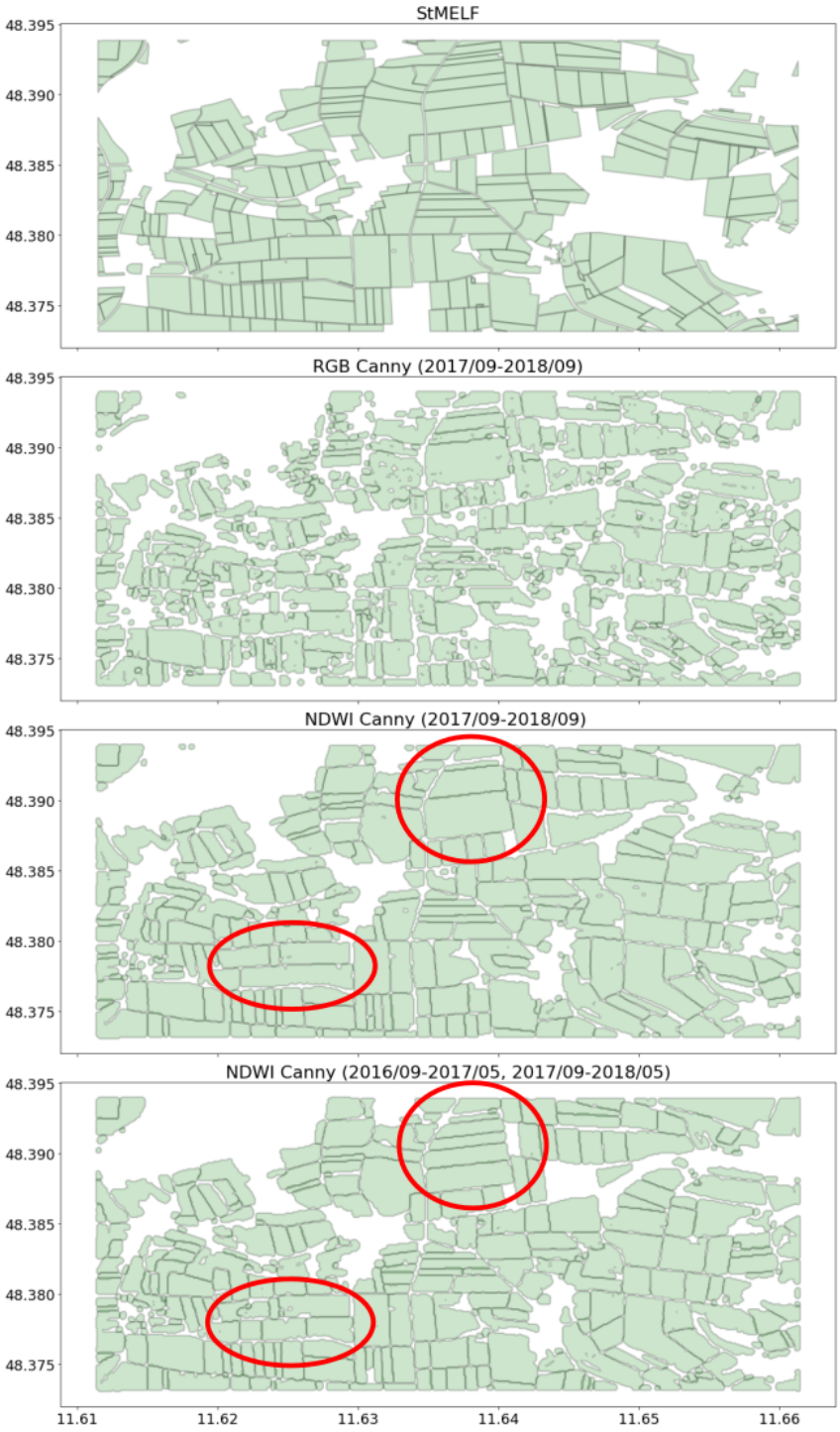

Figure 3.10: Comparison of the results with the reference data basis from StMELF. The red circles mark the improved results based on suitable satellite data.

3.3 Winter wheat yield prediction

3.3.1 Comparison of Level-1C and Level-2A data

A comparison of Level-1C (L1C) and Level-2A (L2A) data was made owing to the continued availability of Level-1C time series since 2015. Various tools, such as the Py6S or Sen2Cor processor, are available for the atmospheric processing of Level-1C products. Each framework achieves slightly different results. Independent of the atmospheric processing quality, we investigated the impact of the respective product on yield prediction. Figures 3.11 and 3.12 show the correlation between yield and band values. The correlation is based on the Kendall rank correlation, which does not require normally distributed measurements and is more robust concerning outliers than Pearson. Significant differences were not achieved for L2A compared to Level-1C. Figure 3.13 also shows the temporal pattern of two indices, where L2A-based $NDVI$ patterns were slightly improved while $NDWI$ patterns did not much differ. The final yield prediction evaluation showed that the accuracy minimally increased with all raw bands. In contrast, the use of an index delivers for both products similar results.

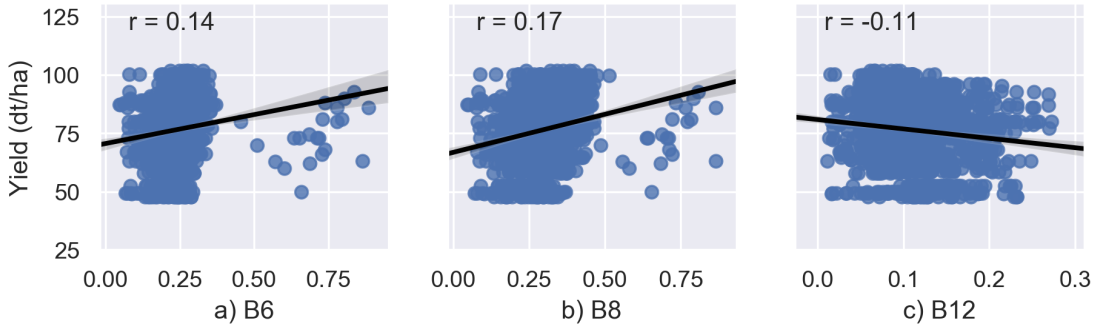

Figure 3.11: Correlations between Level-1C data and yield where a) visualises the correlation for band 6, b) for band 8, and c) for band 12.

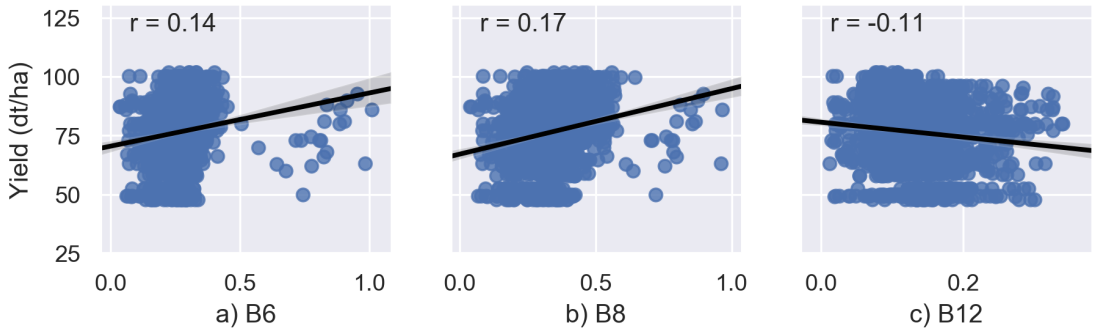

Figure 3.12: Correlations between Level-2A data and yield where a) visualises the correlation for band 6, b) for band 8, and c) for band 12.

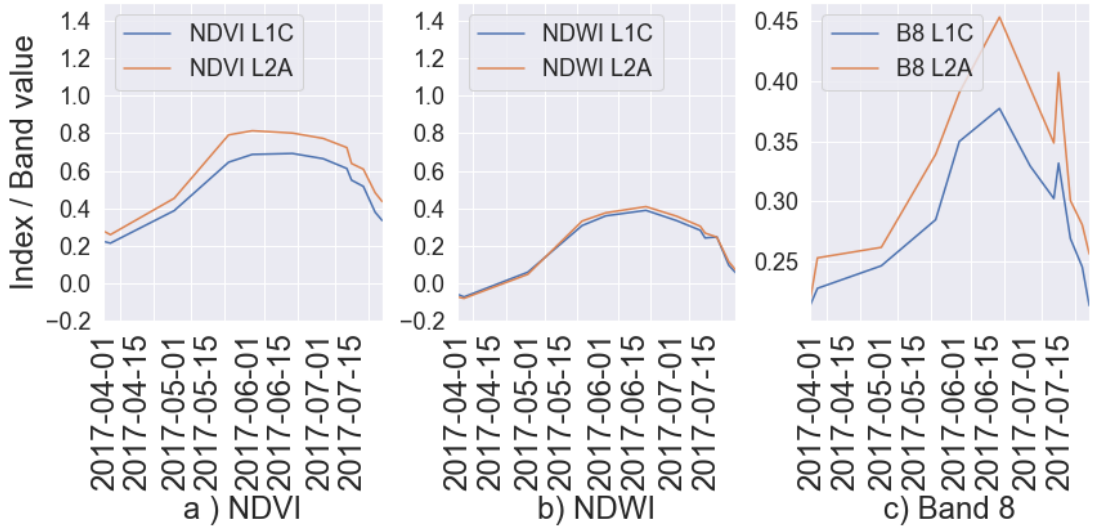

Figure 3.13: Comparison of temporal patterns of a) $NDVI$, b) $NDWI$ and c) band 8 of an exemplary field in 2017. Level-1C is visualised in blue while L2A in orange.

3.3.2 Evapotranspiration and water demand

The water consumption of a plant is an important yield determining factor. Since it is challenging to determine soil moisture in the root zone by satellite remote sensing, a validated approach for determining the water demand was adopted and the daily crop water requirements at the field level were determined by means of ET_c. As indicated, the K_c factor represents an averaged value over all pixels for a given field. Table 3.6

shows the results for ET_c and CWR, depending on the chosen index. Temperature and solar radiation are mean values, while all the other values were accumulated over the vegetation period from March to the end of July. Figure 3.14 visualises the cumulative CWR from March to the end of July. The temperature increased by 1.3 °C, within the three years under investigation, which is also reflected in a higher solar radiation. The mean temperature was 12.0 °C in 2016, 12.6 °C in 2017, and 13.3 °C in 2018. Increasing temperature and solar radiation also increased ET_0, while precipitation was about 300 mm in each year. ETc_{NDVI} showed the highest water demand across all years, while ETc_{REIP} indicated the lowest. Negative CWR values indicate, that additional water supply was not needed, while positive values, as in the case of CWR_{NDVI} and CWR_{NDRE}, indicate additional water needs. The highest crop water requirements were observed in 2017 with 100.8 mm calculated by CWR_{NDVI} and 60.6 mm calculated by CWR_{NDRE}.

Table 3.6: Overview of the mean ET_c and water balance (CWR) values on the field level in mm. The ET_c values are based on the Level-2A product.

	2016	**2017**	**2018**
Temperature (°C):	12.0	12.6	13.3
Solar Radiation (MJ):	17.8	19.1	19.2
ET_0 (mm):	448.4	499.0	514.6
Precipitation (mm):	314.4	294.2	302.3
ETc_{NDVI} (mm):	385.3	395.1	374.3
ETc_{NDWI} (mm):	276.2	265.6	251.8
ETc_{REIP} (mm):	189.6	210.9	218.0
ETc_{NDRE} (mm):	341.3	354.8	329.2
CWR_{NDVI} (mm):	70.9	100.8	72.0
CWR_{NDWI} (mm):	-38.2	-28.6	-50.5
CWR_{REIP} (mm):	-124.9	-83.3	-84.4
CWR_{NDRE} (mm):	26.9	60.6	26.9

Even though the deficit is small, the individual months must be analysed. The plot for 2018 in Figure 3.14 shows that there was less precipitation between March and middle May while at the same time, spring temperatures increased substantially (Figure 2.6). Although the field water capacity was filled up in each year after winter, some fields have sandy soils characterised by a reduced field water capacity, which in turn may affect the yield. Crop yields from 2016 onwards were decreased by around 10% annually. In June and July 2017, the CWR_{NDVI} and CWR_{NDRE} deviated more from the cumulative precipitation than in 2016 and 2018. Further inspection of Figure 3.15 reveals that both indices indirectly reflect increased precipitation in May 2017 via altered plant growth. Biomass and canopy water contents were decreased and increased rapidly due to following precipitation.

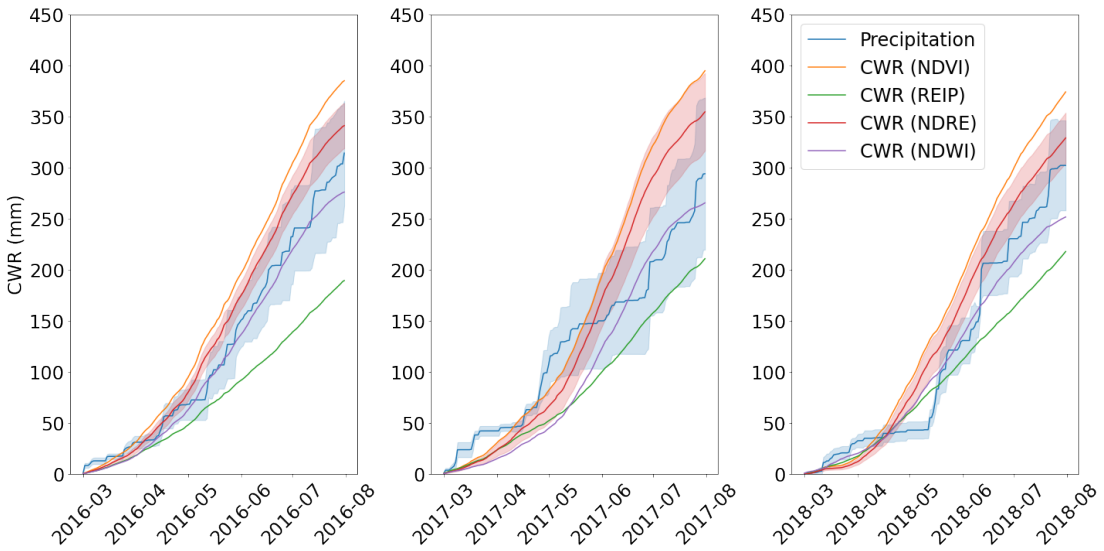

Figure 3.14: Cumulative daily crop water requirement (CWR) and precipitation based on $NDVI$, $NDWI$, $REIP$ and $NDRE$ and cumulative precipitation in the years 2016, 2017 and 2018. The temporal pattern of $NDRE$ and precipitation is visualised with its maximum and minimum deviation, reflecting the heterogeneity of the region.

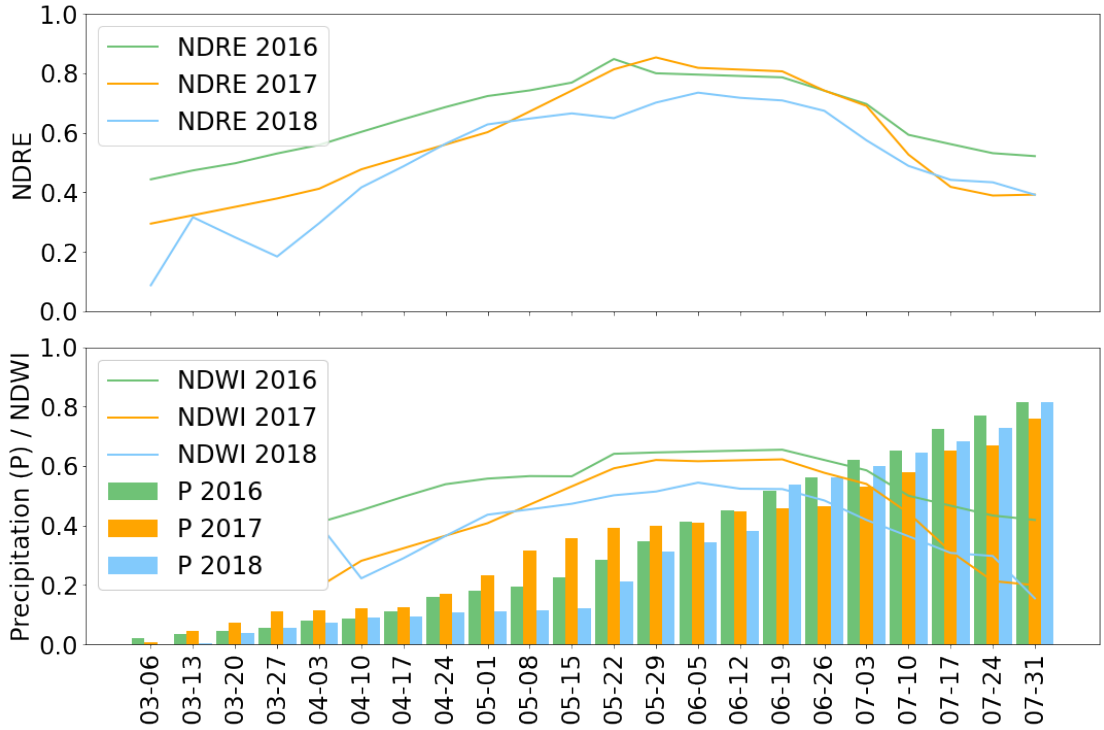

Figure 3.15: Time patterns of $NDWI$ and $NDRE$ for 2016, 2017, and 2018. The $NDWI$ reflects the effect of precipitation deficit or drought. The $NDWI$ and precipitation (P) values were normalised to 1 as maximum and 0 as a minimum to visualise the precipitation effect in 2017.

3.3.3 Yield prediction

3.3.3.1 Yield prediction with climatological data

The experiments with climatological data, shown in Table 3.7, include cloud cover, humidity, precipitation, solar radiation, maximum, minimum, and mean temperature, wind speed, sunshine duration, and air pressure. Since some parameters correlate with each other, this may lead to multicollinearity. Stepwise linear regression and random forest are suitable for the investigated cases and avoid overfitting. For stepwise linear regression, only predictors having the most significant influence on the dependent variable (yield) were used within the model. By analysing the feature importance of the first model with R^2 of 0.8 and a $RMSE$ of 6.39 dt ha^{-1}, solar radiation revealed to be most important in all five months before harvest, followed by precipitation in March.

Table 3.7: Overview of the best results with climatological data (CD), sorted by R^2 and $RMSE$. All daily climatological measurements were interpolated to weekly and monthly mean values and standardized. Random Forest (RF) and Stepwise Linear Regression (LR) were applied for the prediction of winter wheat yields.

Features	**Method**	**Resolution**	R^2	MAE	$RMSE$	CV	$CV std$
CD	RF	monthly	0.80	4.26	6.39	0.53	0.11
CD	RF	weekly	0.79	4.44	6.51	0.62	0.08
CD	LR	monthly	0.69	5.79	7.92	0.61	0.1
CD	LR	weekly	0.68	5.9	7.99	0.43	0.15

3.3.3.2 Yield prediction with an index or raw bands

LR was superior to RF, and the usage of all raw bands outperformed the index-based approach. The best indices for yield prediction were the $NDWI$ and the $REIP$. The water-sensitive $NDWI$ achieved a R^2 of 0.6 and a $RMSE$ of 8.9 $\mathrm{dt\,ha^{-1}}$, with cross-validated results showing that the $REIP$ was slightly better performing. In contrast, the $NDRE$ and $NDVI$ achieved lower accuracy and explained about 30 to 50 percent of the yield variance. Table 3.8 also supports the previous notion regarding Level-2A and Level-1C products. Yield prediction was only slightly better with L2A data. Weekly resolution excelled the monthly resolution, as it better reflected the biomass growth status of winter wheat. With a monthly resolution, important information can be lost. The significant bands of the best model ($p < 0.01$) were B6 and B7, four and five weeks before harvest and B4, B5, B7, B9, B10, and B11 in April and at the end of March. When comparing the feature importance of RF, it became evident that B8 and B8A were most important for RF one month before harvest. Nevertheless, the previously mentioned significant bands were also identified by RF as yield relevant factors.

Table 3.8: Comparison of yield prediction with raw bands and based on indices. All satellite data acquisitions were resampled to weekly and monthly mean values and linearly interpolated.

Features	**Method**	**Resolution**	**Level**	R^2	MAE	$RMSE$	CV	$CV std$
B1-B12	LR	weekly	2A	0.83	4.64	5.78	0.58	0.14
B1-B12	LR	weekly	1C	0.77	5.63	6.78	0.56	0.09
B1-B12	LR	monthly	2A	0.71	5.64	7.55	0.44	0.08
B1-B12	LR	monthly	1C	0.71	6.62	7.55	0.43	0.19
B1-B12	RF	weekly	2A	0.64	6.83	8.46	0.44	0.1
B1-B12	RF	weekly	1C	0.63	6.91	8.64	0.34	0.1
$NDWI$	LR	weekly	1C	0.6	7.12	8.92	0.4	0.29
B1-B12	RF	monthly	1C	0.58	7.4	9.19	0.42	0.14
B1-B12	RF	monthly	2A	0.54	7.61	9.57	0.3	0.27
$NDWI$	RF	weekly	1C	0.52	7.36	9.79	0.41	0.12
$NDWI$	RF	weekly	2A	0.52	7.16	9.79	0.28	0.24
$NDRE$	LR	weekly	2A	0.51	7.73	9.91	0.29	0.06
$NDRE$	LR	weekly	1C	0.49	7.87	10.05	0.3	0.13
$REIP$	LR	weekly	2A	0.49	7.88	10.14	0.49	0.08
$REIP$	RF	monthly	2A	0.48	7.32	10.17	0.31	0.17
$NDWI$	RF	monthly	2A	0.48	7.85	10.2	0.43	0.08
$REIP$	RF	weekly	2A	0.48	7.65	10.23	0.26	0.21
$REIP$	RF	weekly	1C	0.47	7.3	10.24	0.38	0.09
$NDVI$	RF	weekly	2A	0.47	7.89	10.25	0.27	0.08
$NDWI$	RF	monthly	1C	0.46	7.98	10.42	0.38	0.14

3.3.3.3 Yield prediction with value-based information

The next investigation focused on ET-based information, introduced in section 2.2.2. Table 3.9 compares the performance of all water-related features and lists the best 20 results.

Table 3.9: Value-based information and its impact on winter wheat yields. All daily values were resampled to weekly and monthly mean values and linearly interpolated. Precipitation is referred to as P in the table.

Features	**Method**	**Resolution**	**Level**	R^2	MAE	$RMSE$	CV	$CV std$
B1-B12, ET_0, P	LR	weekly	2A	0.84	4.91	5.63	0.72	0.07
B1-B12, ET_0, P	LR	monthly	1C	0.83	3.94	5.78	0.72	0.09
B1-B12, ET_0, P	LR	weekly	1C	0.83	4.85	5.87	0.72	0.06
CWR (K_c:$NDWI$)	LR	weekly	1C	0.79	4.89	6.45	0.62	0.04
B1-B12, ET_0, P	LR	monthly	2A	0.79	5.43	6.45	0.71	0.05
CWR (K_c:$NDWI$)	LR	weekly	2A	0.79	4.92	6.46	0.66	0.07
ET_c (K_c:$NDVI$)	LR	weekly	2A	0.74	5.82	7.15	0.34	0.14
Δ (K_c:$NDRE$)	LR	weekly	2A	0.74	5.4	7.16	0.49	0.18
ET_c (K_c:$REIP$)	RF	weekly	2A	0.74	5.2	7.2	0.52	0.1
ET_c (K_c:$NDVI$)	LR	weekly	1C	0.73	5.96	7.36	0.51	0.11
CWR (K_c:$REIP$)	RF	monthly	1C	0.73	5.36	7.37	0.61	0.04
ET_c (K_c:$REIP$)	RF	weekly	1C	0.73	5.03	7.37	0.63	0.14
Δ (K_c:$NDRE$)	RF	weekly	2A	0.72	5.25	7.44	0.46	0.13
Δ (K_c:$NDRE$)	RF	weekly	1C	0.72	5.35	7.52	0.48	0.11
ET_c (K_c:$REIP$)	LR	weekly	1C	0.71	6.04	7.63	0.61	0.11
ET_c (K_c:$REIP$)	RF	monthly	1C	0.7	5.54	7.68	0.37	0.11
CWR (K_c:$REIP$)	RF	weekly	1C	0.7	5.37	7.71	0.71	0.06
Δ (K_c:$NDRE$)	RF	monthly	1C	0.7	5.58	7.73	0.65	0.06
CWR (K_c:$NDRE$)	RF	weekly	1C	0.69	5.61	7.85	0.41	0.1
ET_c (K_c:$NDWI$)	LR	weekly	2A	0.69	6.05	7.87	0.33	0.22

LR achieved the best prediction with all bands, ET_0, and precipitation. RF achieved a R^2 of 0.65 with the same features. Surprisingly, the performance of the value-based information CWR or ET_c was less accurate than when using only the bands in combi-

nation with ET_0 and precipitation. It is interesting to notice that evapotranspiration and precipitation had a smaller influence on the accuracy when comparing the results in Table 3.8, where the use of bands alone achieved slightly lower accuracies. However, the cross-validation accuracy showed that this model was more reliable. The significant features for the best model ($p < 0.01$) were band 6, band 7 and band 9 at the end of June and beginning of July, as well as band 5, band 9, and band 11 in March. Short wave infrared bands were good proxies in spring while red edge bands performed well around one month before harvest. Precipitation contributed significantly about 9 and 20 weeks before harvest. The ET_0 parameter was excluded from the model as it was not significant. Nevertheless, in one experiment, the use of ET_0 alone achieved a R^2 of up to 0.68 and a $RMSE$ of 7.99 dt ha^{-1}. As shown in Table 3.8, the $NDWI$ was the most successful yield predictive feature using CWR, while the CWR combined with $REIP$ was also a good proxy depicting a high cross-validated R^2 (CV) and a low standard deviation accuracy.

3.3.3.4 Yield prediction with all features

As final experimental investigation, all features were included to compare the performance and to determine the best model. The use of all the features achieved a R^2 of 0.9 and a $RMSE$ of 4.4 dt ha^{-1} (Table 3.10). Comparing the cross-validated models with all features, monthly resolution weakened the results from 0.79 R^2 to 0.67 R^2. All features include climatological data, raw bands, indices and value-based information as input for the models. Random Forest performed moderate with climatological data and monthly resolution. Linear regression achieved better results in most cases, whereby the weekly resolution also improved the results, followed by two models that achieved satisfactory results with raw bands, precipitation and ET_0. The weekly and monthly resolution slightly influenced the accuracy. Table 3.11 lists all the significant features, determined by stepwise linear regression. In contrast, RF achieved a R^2 of 0.72 and a $RMSE$ of 7.53 dt ha^{-1} with all features. The significance of the independent variables varied slightly. When the second-best model was analysed, the solar radiation dominated again instead of humidity and minimum temperature. In this experimental run, stepwise LR determined the standard deviation of $REIP$, B9, and B5 in spring as significantly contributing

features. The standard deviation provides information on the heterogeneity of a field. Besides, the water requirement at the end of March and the beginning of April reflected by CWR was revealed to be significant.

Table 3.10: Overview of the best 20 results with all features. Precipitation is referred to as P and climatological data is referred to as CD.

Features	**Method**	**Resolution**	**Level**	R^2	MAE	$RMSE$	CV	$CV std$
All features	LR	weekly	2A	0.9	3.65	4.4	0.79	0.06
All features	LR	weekly	1C	0.9	3.21	4.49	0.74	0.11
B1-B12, ET_0, P	LR	weekly	2A	0.84	4.91	5.63	0.72	0.07
B1-B12, ET_0, P	LR	monthly	1C	0.83	3.94	5.78	0.72	0.09
All features	LR	monthly	2A	0.83	4.68	5.78	0.67	0.1
B1-B12	LR	weekly	2A	0.83	4.64	5.78	0.58	0.14
B1-B12, ET_0, P	LR	weekly	1C	0.83	4.85	5.87	0.72	0.06
CD	RF	monthly		0.8	4.26	6.39	0.53	0.11
CWR (K_c:$NDWI$)	LR	weekly	1C	0.79	4.89	6.45	0.62	0.04
B1-B12, ET_0, P	LR	monthly	2A	0.79	5.43	6.45	0.71	0.05
CWR (K_c:$NDWI$)	LR	weekly	2A	0.79	4.92	6.46	0.66	0.07
CD	RF	weekly		0.79	4.44	6.51	0.62	0.08
B1-B12	LR	weekly	1C	0.77	5.63	6.78	0.56	0.09
Δ (K_c:$REIP$)	RF	weekly	1C	0.75	4.74	7.0	0.61	0.06
ET_c (K_c:$NDVI$)	LR	weekly	2A	0.74	5.82	7.15	0.34	0.14
Δ (K_c:$NDRE$)	LR	weekly	2A	0.74	5.4	7.16	0.49	0.18
All features	LR	monthly	1C	0.74	5.29	7.2	0.65	0.1
ET_c (K_c:$REIP$)	RF	weekly	2A	0.74	5.2	7.2	0.52	0.1
Δ (K_c:$REIP$)	RF	weekly	2A	0.74	5.25	7.24	0.5	0.17
Δ (K_c:$NDVI$)	RF	weekly	1C	0.73	5.25	7.28	0.5	0.26

Table 3.11: Significant features ($p < 0.01$). Weeks describes the number of weeks before harvest, starting with the last week in July and counting back to the first week in March.

Feature	**Weeks**
Humidity	1
B6 mean	4
ET_c:(K_c:$NDWI$)	5
Min. Temperature	11
B9 mean	12
B9 std	12
CWR (K_c:$REIP$)	16
$REIP$ std	17
B5 std	19
B9 mean	20

4 Discussion and conclusions

4.1 Crop water demand

Water is one of the most important yield-contributing factors, if not the most important, why a detailed research in the field of satellite-based determination of water needs was conducted. The focus of this thesis is yield prediction at the field level. Therefore, high spatial and temporal resolutions of the data represent important requirements and are key to this work. Satellites such as ASCAT, SMOS or SMAP are not suitable in this context due to the spatial requirements. Sentinel-1 satisfies both requirements and can be used for soil moisture mapping at the field level. A meta-analysis of different publications, presented in 1.2, revealed that the estimation of soil moisture is linked to several issues. On the one hand a denser vegetation influences the measurements or backscatters, on the other hand the measurements are only suitable for the upper soil layer at best (Greifeneder et al., 2016; Greifeneder et al., 2018; Merzouki and McNairn, 2015; Merzouki et al., 2011; Pasolli et al., 2015). Basically, the applied C-band is the limiting characteristic because of its wavelength which can not penetrate vegetation at a $NDVI$ more than 0.7 (El Hajj et al., 2018a). The application of a P-band or L-band SAR would overcome this issue due to its higher wavelength. However, it could also be shown that the C-band provides very good estimates of surface soil moisture over bare soil or sparse vegetation cover. The dense vegetation could be bridged by including evapotranspiration (Andorfer, 2019). As part of an accompanying bachelor thesis, it was verified that ET_c can be used for the estimation of surface soil moisture with a high accuracy. A combination of both approaches, Sentinel-1 for SM determination in spring in combination with ET_c in the course of plant development, represents a possible alternative to solve the described disadvantages of Sentinel-1 (Andorfer, 2019). This study was based on continuous SM measurements with a time domain reflectometry (TDR)

sensor and timed with Sentinel-1 flyovers. Although it is possible to estimate surface SM, soil moisture measurements in the root zone would be needed to obtain better yield predictions for deep-rooted plants. The determination of root zone SM is still the subject of research, and in general no intensive efforts have been made compared to surface SM (Baldwin et al., 2017, 2019; Ford et al., 2014; Manfreda et al., 2014). For that reason, the yield prediction takes water needs estimates based on a FAO56-based approach. It was hypothesised that calculating the daily water demand may also improve yield prediction. Section 4.4 discusses the results and their general usability. By integrating $NDWI$, it is possible to provide indirect information on the status of water supply and this applies to areas with good water availability (Liang et al., 2020; Serrano et al., 2019).

4.2 Crop-type identification

The crop-type classification investigated covers several aspects. Each field selected was represented by a geo-referenced polygon, which was used to determine an average value for all containing pixels. We compared the SVM and RF algorithms and concluded that RF achieves very high accuracies. A multi-temporal approach was preferred and included resampled satellite observations every 14 days. This makes it possible to follow the phenological stages of the selected crops such as winter wheat or maize. Based on the phenological stage and the spectral differences, the crop types can be identified. This holds also true for crops such as winter wheat and winter barley, which have similar spectral fingerprints but are not as distinct as maize and winter wheat, for example. Cloud coverage represents a critical aspect to be considered. Our data set included 2400 samples (fields) from different locations in Upper Bavaria, so we allowed a small amount of noise (clouds) and downloaded data on each field from GEE with a meta cloud filter of 20%. Nevertheless, a complete cloud-free time series would be preferable. Still, since cloud filtering is a time-consuming application, it is sometimes better to focus on the target and allow some noise. Nevertheless, an analysis of the influence of the signal-to-noise ratio on the accuracy would be interesting. The application of Level-1C and L2A data is an important part of this work. L2A slightly improved the crop classification (Rußwurm et al., 2020) and yield prediction (see section 3.3) but the minimal differences do not justify the incorporation of L2A data. The greater computation effort, comparable

accuracies as well as differences of the L2A processors (e.g. Sen2Cor, Py6S) raise the question of whether Level-2A data should be used to develop new approaches. This only complicates the comparison of results. On the other hand, atmospheric effects are eliminated and the quality of the RGB images are improved. Consequently, the use of the processing level should be considered on a case-by-case basis and not as a necessity. The results shown in section 3.1, based on linear interpolation and RF, achieved accuracies up to 92%. It should be emphasised that these results are not yet suitable for further predictive application. The use of crop-type and field boundary detection also requires analysis in relation to their forecast capability. Yield forecasts are usually performed a few weeks before harvest. Consequently, the crop-type and field boundary detection must be performed in the same way for regions where no official field boundaries or crop types are available. Another important finding is the usage of all raw bands. While most publications focus on the usage of $NDVI$ time series, we verified the raw bands as well which improved the separation of crops. While the use of atmospherically corrected images seems to be a prerequisite, the arbitrary use of an index is not questioned. $NDVI$ is an index mainly used to assess chlorophyll and biomass. However, the biomass as well as the chlorophyll content of some crops do not differ very much, particularly in spring. So, the question arises why to choose a multi-temporal approach if one loses information? In contrast, the use of a spectral fingerprint, based on raw bands, offers the possibility to separate crops more clearly. This assumption was confirmed that the usage of raw bands delivers more accurate results (Marszalek et al., 2020). By using all 13 bands of Sentinel-2, the spectral bandwidth is extended and a better insight can be gained. For example, the RGB bands provide colour information, which is very advantageous in the case of rapeseed with its yellow and distinct colour in spring. The $NDVI$ would lose this additional information. One further point is related to Sentinel-1. In our experiments, the availability of cloud-free images is ensured and sufficient data could be used for detection. Gaps in the time series can be modelled by temporal interpolation, but when the target region suffers from very high cloud coverage (e.g. in the tropics), it would be advisable to fuse Sentinel-1 with Sentinel-2. The authors in (Tricht et al., 2018) mention the advantage of this fusion, but the presented experiments in Bavaria did not suffer from insufficient multi-spectral data availability.

4.3 Field boundaries

The need to derive field boundaries is the key to the classification of crop types. The object-based methodology used in this work for yield prediction and crop-type classification requires field borders. The investigations were based on recorded data obtained from StMELF, but a further transfer to regions without official field borders requires an automatised solution. Evaluating literature regarding the state-of-the-art, Canny edge detection was selected for the first experimental runs. One typical problem of edge detection is the high number of detected and irrelevant edges, which can be considered as noise. This problem could be avoided by using the $NDWI$ as an index designed for water assessment. Nevertheless, the simplified visualisation and the improved field boundaries do represent a benefit that reduces noise. A comparison with RGB images (band 2, 3 and 4) demonstrated this advantage. An observer in an aeroplane would recognise field boundaries from several characteristics such as colour or texture. But edge detection that suffers from noise detects too many edges in RGB and delivers less accurate results. The advantage of using the $NDWI$ in combination with a multi-temporal approach using several images permitted a producer accuracy of 81% and an user accuracy of 79%. Considering the simplicity of this approach and the fact that no labelled data are needed as in the case of supervised learning, these results are interesting. Since these results only reflect the first step, further experiments are necessary. The applied $NDWI$ is based on band 8 and band 3 and not band 11 as used for yield prediction. The 10 metre resolution is an important factor, since the resolution should be sufficient to visualise sharp field borders. Nevertheless, although more effort is required here, this unsupervised solution can be applied worldwide. The efficiency of supervised learning (Chandwadkar, 2013; Diakogiannis et al., 2020; Masoud et al., 2020; Schultz et al., 2015; Waldner and Diakogiannis, 2019), especially of neural networks, is not in doubt, but the simplicity of the methodology presented is motivating.

4.4 Yield prediction

4.4.1 Climatological data

While the low precipitation in spring 2018 possibly explains reduced yields, this remains more unclear for 2017. Precipitation in the spring of 2017 contributed to a substantial increase in biomass and accordingly the canopy water content, almost reaching that of 2016. However, high temperatures shortly before harvest in 2017 decreased yields probably by accelerating senescence and shortening the grain filling period. The importance of precipitation in spring is also in line with Albers et al. (2017). In general, higher temperatures cause heat stress and shorten the grain filling period (Wheeler et al., 1996). Nevertheless, solar radiation was more important than temperature, which was also reported in other studies (Andarzian et al., 2008; Fischer, 1985; Hernández-Barrera and Rodriguez-Puebla, 2017). The shortened grain filling period caused a shortened absorption of solar radiation, which probably led to yield decreases despite slightly increased solar radiation in 2017 and 2018. The use of climatological data for yield prediction reveals no spatial in-field variability, but it covered at least half of the cross-validated yield variance, which is also in line with previous studies (Albers et al., 2017; Andarzian et al., 2008). Distances between weather stations and fields should be taken into account. In our investigation the field stations were representative of the three sub-regions. If there are no weather stations nearby, satellite-based climatological data could be used as an alternative.

4.4.2 Indices and raw bands

The Level-2A product was compared to Level-1C, with Level-1C achieving suitable yield prediction accuracies. Although Level-2A improves reflectance values minimally, this does not lead to consistent improvements in all cases, and it should be case-specific ascertained whether L2A brings added value. The processing represents an additional overhead and is based on Py6S or Sen2Cor. The sole usage of raw bands using linear regression already achieved good results and eased yield prediction. In contrast, the $NDWI$ and the $REIP$ achieved slightly lower accuracies. In general, indices as ratios of bands focus on partial aspects, e.g., water content ($NDWI$) or nitrogen content ($REIP$) (Prey and

Schmidhalter, 2019a; Serrano et al., 2019). The red and blue wavelengths in the visual spectrum are absorbed by chlorophyll, but only the red band B4 was relevant in our investigation, which is also in line with Skakun et al. (2019). Band 5 up to band 9 cover the red-edge and near-infrared spectrum and are related to leaf structure, chlorophyll, and thus yield. The importance of these bands was already demonstrated (Prey and Schmidhalter, 2019b; Skakun et al., 2019). Surprisingly, the water vapour sensitive band 9 with its central wavelength around 945 nm contributed to the model performance, which is in agreement with (Babar et al., 2006; Prasad et al., 2007). In the SWIR spectrum, B11 contributed to yield prediction. A possible relationship to the soil and leaf water content may account for this (Skakun et al., 2019).

4.4.3 Evapotranspiration

The inclusion of the daily crop water requirements was one of the objectives and proved to be useful for yield prediction, as water is a significant yield driver (Grosso et al., 2018). By combining evapotranspiration with yield-relevant indices up to 79% of the yield variance could be explained. While yield prediction based on upper soil layer moisture content seems rather inappropriate (Pan et al., 2019), evapotranspiration proved to be valuable (Grosso et al., 2018; Tadesse et al., 2015b). This investigation used the FAO-56 method in combination with indices. Weekly linear interpolations revealed to be useful. In particular, the CWR explained yield decreases caused by hot and dry periods in 2017 and 2018. Heat and a high water demand in June and July 2017 probably affected winter wheat growth. Increased temperatures shortened the grain filling period. Nitrogen fertilisation was adequate being highest in 2017. The higher average temperature in 2018 probably also accounted for the yield reduction caused by a shortened grain filling period. CWR_{NDRE} in Figure 3.14 shows that the decreased precipitation could not meet the water demand in spring 2018. Stepwise linear regression proved to be advantageous compared to RF. Random forest usually needs more data while linear regression also allows to generalise on sparse data sets. Future testing with ET-related observations would benefit from additional soil information, but such high-resolution data were not available in this study. However, index-specific information may indirectly provide soil differences via vegetation reflectance and should be further investigated. The $NDRE$ and

$NDWI$ revealed to be useful in estimating the K_c factor and the daily water requirements. In general, the $NDRE$ is well correlated with biomass and does not saturate as quickly as the $NDVI$ (Lilienthal, 2014). The $NDWI$ indirectly allows to connect to water supply and nitrogen uptake (Geesing et al., 2014; Liang et al., 2020; Serrano et al., 2019). Integrating the $REIP$ as K_c factor to reflect the water and nitrogen status by means of a simplified feature however proved to be less accurate.

4.4.4 All features

Up to 90 percent of the yield variance could be explained by using stepwise linear regression. The use of all defined features would be costly. In contrast, raw bands combined with ET_0 and precipitation achieved almost similar results. This simplified feature combination outperformed all index or CWR-based models, achieving an accuracy of up to 0.84 R^2 with a RMSE of 5.63 $\mathrm{dt\,ha^{-1}}$. As in CWR, all climatological data were included, but the raw bands cover a wider spectral bandwidth. Yield relevant parameters such as temperature or solar radiation as discussed in section 4.4.1 are also part of the evapotranspiration (Eq. (2.3)). Hunt et al. (2019) assumed that individual bands could improve yield prediction, but this was not analysed. The authors further highlighted the advantage of fusing environmental data with Sentinel-2. The presented results could be transferred to pixel-based yield maps. Future work should also try to make early yield predictions.

References

Ahmed, A., Zhang, Y., and Nichols, S. Review and evaluation of remote sensing methods for soil-moisture estimation. *SPIE Reviews*, 2(1):1 – 18, 2011. doi: 10.1117/1.3534910.

Al-Kayssi, A., Al-Karaghouli, A., Hasson, A., and Beker, S. Influence of soil moisture content on soil temperature and heat storage under greenhouse conditions. *Journal of Agricultural Engineering Research - J AGR ENG RES*, 45:241–252, 1990. doi: 10.1016/S0021-8634(05)80076-9.

Albers, H., Gornott, C., and Hüttel, S. How do inputs and weather drive wheat yield volatility? The example of Germany. *Food Policy*, 70:50–61, 2017. doi: 10.1016/j.foodpol.2017.05.001.

Alface, A., Pereira, S., Filgueiras, R., and Cunha, F. Sugarcane spatial-temporal monitoring and crop coefficient estimation through NDVI. *Revista Brasileira de Engenharia Agrícola e Ambiental*, 23:330–335, 2019. doi: 10.1590/1807-1929/agriambi.v23n5p330-335.

Aliyu Kasim, A., Carlson, T., and Usman, H. Limitations in validating derived soil water content from thermal/optical measurements using the simplified triangle method. *Remote Sensing*, 12:1155, 2020. doi: 10.3390/rs12071155.

Allan, R., Pereira, L., and Smith, M. *Crop evapotranspiration-Guidelines for computing crop water requirements-FAO Irrigation and drainage paper 56*, volume 56. FAO, 1998.

Allen, R., Tasumi, M., and Trezza, R. Satellite-based energy balance for mapping evapotranspiration with internalized calibration (METRIC) – model. *Journal of Irrigation and Drainage Engineering*, 133, 2007. doi: 10.1061/(ASCE)0733-9437(2007)133:4(380).

Andarzian, B., Bakhshandeh, A., Bannayan, M., Emam, Y., Fathi, G., and Saeed, K. Wheatpot: A simple model for spring wheat yield potential using monthly weather data. *Biosystems Engineering*, 99:487–495, 04 2008. doi: 10.1016/j.biosystemseng.2007.12.008.

Andorfer, T. Analyse von satellitengestützten Verfahren zur Bodenfeuchtebestimmung, 2019. Bachelor thesis. Technical University of Munich, Weihenstephan. [Unpublished].

Argolo dos Santos, R., Mantovani, E., Filgueiras, R., Fernandes-Filho, E., Silva, A., and Venancio, L. Actual evapotranspiration and biomass of maize from a red-green-near-infrared (RGNIR) sensor on board an unmanned aerial vehicle (UAV). *Water*, 12:1–20, 2020. doi: 10.3390/w12092359.

Asam, S. *Potential of high resolution remote sensing data for leaf area index derivation using statistical and physical models.* PhD thesis, Universität Würzburg, 2015.

Awad, M. Toward precision in crop yield estimation using remote sensing and optimization techniques. *Agriculture*, 9:54, 2019. doi: 10.3390/agriculture9030054.

Babar, M. A., van Ginkel, M., Klatt, A. R., Prasad, B., and Reynolds, M. P. The potential of using spectral reflectance indices to estimate yield in wheat grown under reduced irrigation. *Euphytica*, 150:155–172, 01 2006. doi: 10.1007/s10681-006-9104-9.

Baldwin, D., Manfreda, S., Keller, K., and Smithwick, E. Predicting root zone soil moisture with soil properties and satellite near-surface moisture data across the conterminous United States. *Journal of Hydrology*, 546, 2017. doi: 10.1016/j.jhydrol.2017.01.020.

Baldwin, D., Manfreda, S., Lin, H., and Smithwick, E. Estimating root zone soil moisture across the eastern United States with passive microwave satellite data and a simple hydrologic model. *Remote Sensing*, 11:2013, 2019. doi: 10.3390/rs11172013.

Barmeier, G., Hofer, K., and Schmidhalter, U. Mid-season prediction of grain yield and protein content of spring barley cultivars using high-throughput spectral sensing. *European Journal of Agronomy*, 90:108–116, 2017. doi: 10.1016/j.eja.2017.07.005.

Barnes, E., Clarke, T., Richards, S., Colaizzi, P., Haberland, J., Kostrzewski, M., Waller, P., Choi, C., Riley, E., and Thompson, T. Coincident detection of crop water stress, nitrogen status, and canopy density using ground based multispectral data. In *Proceedings of the Fifth International Conference on Precision Agriculture*, 2000.

Basso, B. and Liu, L. Seasonal crop yield forecast: Methods, applications, and accuracies. *Advances in Agronomy*, 2018. doi: 10.1016/bs.agron.2018.11.002.

Bastiaanssen, W., Noordman, E., Pelgrum, H., Davids, G., Thoreson, B., and Allen, R. SEBAL model with remotely sensed data to improve water-resources management under actual field conditions. *Journal of Irrigation and Drainage Engineering*, 131: 85–93, 2005. doi: 10.1061/(ASCE)0733-9437(2005)131:1(85).

Becker, E. and Schmidhalter, U. Evaluation of yield and drought using active and passive spectral sensing systems at the reproductive stage in wheat. *Frontiers in Plant Science*, 8:379, 2017. doi: 10.3389/fpls.2017.00379.

Belgiu, M. and Csillik, O. Sentinel-2 cropland mapping using pixel-based and object-based time-weighted dynamic time warping analysis. *Remote Sensing of Environment*, 204: 509–523, 2018. doi: 10.1016/j.rse.2017.10.005.

Biau, G. and Scornet, E. A random forest guided tour. *TEST*, 25:197–227, 2016. doi: 10.1007/s11749-016-0481-7.

Blaschke, T., Hay, G. J., Kelly, M., Lang, S., Hofmann, P., Addink, E., Queiroz Feitosa, R., van der Meer, F., van der Werff, H., van Coillie, F., and Tiede, D. Geographic object-based image analysis – towards a new paradigm. *ISPRS Journal of Photogrammetry and Remote Sensing*, 87:180 – 191, 2014. doi: https://doi.org/10.1016/j.isprsjprs.2013.09.014.

Bolton, D. and Friedl, M. An introduction to the art of agrometeorological crop yield forecasting using multiple regression. *Crop Monitoring and Forecasting Group Crop Yield Forecasting and Agrometeorology Sub-Project UTF/BGD/029*, 2001.

Bolton, D. and Friedl, M. Forecasting crop yield using remotely sensed vegetation indices and crop phenology metrics. *Agricultural and Forest Meteorology*, 173:74 – 84, 2013. doi: 10.1016/j.agrformet.2013.01.007.

Bradski, G. The OpenCV library. *Dr. Dobb's Journal of Software Tools*, 2000.

Böhler, J., Schaepman, M., and Kneubühler, M. Crop classification in a heterogeneous arable landscape using uncalibrated UAV data. *Remote Sensing*, 10:1282, 2018. doi: 10.3390/rs10081282.

Chai, T. and Draxler, R. Root mean square error (RMSE) or mean absolute error (MAE)?– Arguments against avoiding RMSE in the literature. *Geoscientific Model Development*, 7:1247–1250, 06 2014. doi: 10.5194/gmd-7-1247-2014.

Chandwadkar, R. Comparison of edge detection techniques. In *6th Annual Conference of IRAJ*, 2013. doi: 10.13140/RG.2.1.5036.7123.

Chen, B., Qiu, F., Wu, B., and Du, H. Image segmentation based on constrained spectral variance difference and edge penalty. *Remote Sensing*, 7:5980–6004, 2015. doi: 10.3390/rs70505980.

Chen, C.-C., McCarl, B., and Schimmelpfennig, D. Yield variability as influenced by climate: A statistical investigation. *Climatic Change*, 66, 2004. doi: 10.1023/B:CLIM.0000043159.33816.e5.

Chetan, M., Dornik, A., and Urdea, P. Comparison of object and pixel-based land cover classification through three supervised methods. *Zeitschrift für Geodäsie, Geoinformation und Landmanagement*, 5:265–270, 2017. doi: 10.12902/zfv-0165-2017.

Cortes, C. and Vapnik, V. Support vector machines. *Machine Learning*, 20:273–293, 1995.

Cristianini, N. and Shawe-Taylor, J. *An Introduction to Support Vector Machines and Other Kernel-based Learning Methods*. Cambridge University Press, 2000. doi: https://doi.org/10.1017/CBO9780511801389.

DarkSky. Dark Sky API, 2020. URL `https://darksky.net/dev`. [Online; accessed 24-July-2020].

Diakogiannis, F., Waldner, F., Caccetta, P., and Wu, C. Resunet-a: A deep learning framework for semantic segmentation of remotely sensed data. *ISPRS Journal of Photogrammetry and Remote Sensing*, 162:94–114, 2020. doi: 10.1016/j.isprsjprs.2020.01.013.

Dimitrov, P., Dong, Q., Eerens, H., Gikov, A., Filchev, L., Roumenina, E., and Jelev, G. Sub-pixel crop type classification using PROBA-V 100 m NDVI time series and reference data from Sentinel-2 classifications. *Remote Sensing*, 11, 2019. doi: https://doi.org/10.3390/rs11111370.

DLR. EnMAP hyperspectral imager, 2020. URL `https://www.enmap.org`. [Online; accessed 12-August-2020].

Doraiswamy, P., Akhmedov, B., Stern, A., and Hatfield, J. MODIS applications for mapping regional crop yields. In *International Geoscience and Remote Sensing Symposium (IGARSS)*, volume 4, pages 2197 – 2199 vol.4, 2003. doi: 10.1109/IGARSS.2003.1294387.

D'Urso, G. and Belmonte, A. Operative approaches to determine crop water requirements from Earth observation data: Methodologies and applications. *AIP Conference Proceedings*, 852:14–25, 2006. doi: 10.1063/1.2349323.

D'Urso, G., Berger, K., Calera, A., Osann, M., Escadafal, R., Garatuza-Pajan, J., Hanich, L., Perdigao, A., Tapia, J., and Vuolo, F. Earth observation products for operational irrigation management: the PLEIADeS project. *Agricultural Water Management*, 98: 271–282, 2010. doi: 10.1117/12.830072.

DWD. AMBAV — National meteorological service of Germany, 2020a. URL `https://www.dwd.de/DE/klimaumwelt/ku_beratung/landwirtschaft/agrar_modelle/ambav.html`. [Online; accessed 24-July-2020].

DWD. Open data — National meteorological service of Germany, 2020b. URL `https://opendata.dwd.de/`. [Online; accessed 23-July-2020].

El Hajj, M., Baghdadi, N., Bazzi, H., and Zribi, M. Penetration analysis of SAR signals in the C and L bands for wheat, maize, and grasslands. *Remote Sensing*, 11:31, 2018a. doi: 10.3390/rs11010031.

El Hajj, M., Baghdadi, N., Zribi, M., Rodriguez-Fernandez, N., Wigneron, J.-P., Al-Yaari, A., Al Bitar, A., Albergel, C., and Calvet, J.-C. Evaluation of SMOS, SMAP, ASCAT and Sentinel-1 soil moisture products at sites in southwestern France. *Remote Sensing*, 10:569, 2018b. doi: 10.3390/rs10040569.

ESA. ALOS-2 (Advanced Land Observing Satellite) — eoPortal directory, 2020a. URL `https://earth.esa.int/web/eoportal/satellite-missions/a/alos-2`. [Online; accessed 12-August-2020].

ESA. PRISMA (Hyperspectral precursor and application mission) — eoPortal directory, 2020b. URL `https://directory.eoportal.org/web/eoportal/satellite-missions/p/prisma-hyperspectral`. [Online; accessed 12-August-2020].

ESA. PROBA-1 — Earth online, 2020c. URL `https://earth.esa.int/web/guest/missions/esa-operational-eo-missions/proba`. [Online; accessed 12-August-2020].

ESA. Sentinel-1 SAR instrument — Sentinel online, 2020d. URL `https://sentinel.esa.int/web/sentinel/technical-guides/sentinel-1-sar/sar-instrument`. [Online; accessed 12-August-2020].

ESA. Sentinel-2 — Sentinel online, 2020e. URL `https://sentinel.esa.int/web/sentinel/missions/sentinel-2`. [Online; accessed 12-August-2020].

ESA. Sentinel-3 Mission summary — Sentinel online, 2020f. URL `https://sentinel.esa.int/web/sentinel/missions/sentinel-3/overview/mission-summary`. [Online; accessed 12-August-2020].

Escolà, A., Badia, N., Arnó, J., and Martínez-Casasnovas, J. A. Using Sentinel-2 images to implement precision agriculture techniques in large arable fields: First results of a case study. *Advances in Animal Biosciences*, 8:377–382, 2017. doi: https://doi.org/10.1017/S2040470017000784.

Faisol, A., Indarto, I., Novita, E., and Budiyono. An evaluation of MODIS global evapotranspiration product (MOD16A2) as terrestrial evapotranspiration in east Java - Indonesia. *IOP Conference Series: Earth and Environmental Science*, 485:012002, 2020. doi: 10.1088/1755-1315/485/1/012002.

FAO. Crop evapotranspiration - Guidelines for computing crop water requirements - FAO irrigation and drainage paper 56, 2020. URL `http://www.fao.org/3/X0490E/x0490e00.htm#Contents`. [Online; accessed 23-July-2020].

Fischer, R. A. Number of kernels in wheat crops and the influence of solar radiation and temperature. *The Journal of Agricultural Science*, 105(2):447–461, 1985. doi: 10.1017/S0021859600056495.

Ford, T., Harris, E., and Quiring, S. Estimating root zone soil moisture using near-surface observations from SMOS. *Hydrology and Earth System Sciences*, 18, 2014. doi: 10.5194/hess-18-139-2014.

Foroughi, H., Naseri, A., Nasab, S., Hamzeh, S., Sadeghi, M., Tuller, M., and Jones, S. A new mathematical formulation for remote sensing of soil moisture based on the red-nir space. *International Journal of Remote Sensing*, 41:8034–8047, 2020. doi: 10.1080/01431161.2020.1770365.

Friedl, M. and Sulla-Menashe, D. MCD12Q1 MODIS/Terra+Aqua land cover type yearly L3 global 500m SIN Grid V006 [data set]. NASA EOSDIS land processes DAAC, 2019. URL `https://doi.org/10.5067/MODIS/MCD12Q1.006`. [Online; accessed 31-August-2020].

Gao, B.-C. NDWI—A normalized difference water index for remote sensing of vegetation liquid water from space. *Remote Sensing of Environment*, 58:257–266, 1996. doi: 10.1016/S0034-4257(96)00067-3.

GAO, L., WANG, X.-F., GU, X.-F., TIAN, Q.-J., JIAO, J.-N., WANG, P.-Y., and LI, D. Exploring the influence of soil types underneath the canopy in winter wheat leaf area index remote estimating. *Chin J Plan Ecolo*, 41(12):1273–1288, 2017. doi: 10.17521/cjpe.2017.0231.

GEE. Sentinel-2 MSI: Multispectral instrument, Level-1C — Earth Engine data catalog, 2012. URL `https://developers.google.com/earth-engine/datasets/catalog/COPERNICUS_S2`. [Online; accessed 21-July-2020].

GEE. EO1 Hyperion hyperspectral imager — Earth Engine data catalog, 2020. URL `https://developers.google.com/earth-engine/datasets/catalog/EO1_HYPERION`. [Online; accessed 12-August-2020].

GEE. A planetary-scale platform for Earth science data & analysis — Google Earth Engine, 2020. URL `https://earthengine.google.com/`. [Online; accessed 21-July-2020].

Geesing, D., Diacono, M., and Schmidhalter, U. Site-specific effects of variable water supply and nitrogen fertilisation on winter wheat. *Journal of Plant Nutrition and Soil Science*, 177, 2014. doi: 10.1002/jpln.201300215.

Gorelick. Segmentation, 2020. URL `https://docs.google.com/presentation/d/1p_W06MwdhRFZjkb7imYkuTchatY5nxb5aTRgh6qm2uU/view#slide=id.p`. [Online; accessed 27-January-2020].

Gorelick, N., Hancher, M., Dixon, M., Ilyushchenko, S., Thau, D., and Moore, R. Google Earth Engine: Planetary-scale geospatial analysis for everyone. *Remote Sensing of Environment*, 202:18–27, 2017. doi: 10.1016/j.rse.2017.06.031.

Goswami, S., Matin, S., Saxena, A., and Bairagi, G. A review: The application of remote sensing, GIS and GPS in precision agriculture. *International Journal of Advanced Technology & Engineering Research (IJATER)*, Volume 2, 2012.

Greifeneder, F., Notarnicola, C., and Wagner, W. Using machine learning and SAR data for the upscaling of large scale modelled soil moisture in the Alps. In *Proceedings of EUSAR 2016: 11th European Conference on Synthetic Aperture Radar*, pages 1–4, 2016.

Greifeneder, F., Khamala, E., Sendabo, D., Wagner, W., Zebisch, M., Farah, H., and Notarnicola, C. Detection of soil moisture anomalies based on Sentinel-1. *Physics and Chemistry of the Earth, Parts A/B/C*, 2018. doi: 10.1016/j.pce.2018.11.009.

Grosso, C., Manoli, G., Martello, M., Chemin, Y., Pons, D., Teatini, P., Piccoli, I., and Morari, F. Mapping maize evapotranspiration at field scale using SEBAL: A comparison with the FAO method and soil-plant model simulations. *Remote Sensing*, 10:1452, 2018. doi: 10.3390/rs10091452.

Guyot, G., Frederic, B., and Major, D. High spectral resolution: Determination of spectral shifts between the red and the near infrared. *International Archives of Photogrammetry and Remote Sensing*, 11:750–760, 1988.

Guzinski, R., Nieto, H., Sandholt, I., and Karamitilios, G. Modelling high-resolution actual evapotranspiration through Sentinel-2 and Sentinel-3 data fusion. *Remote Sensing*, 2020. doi: 10.3390/rs12091433.

Hao, P., Wang, L., Zhan, Y., and Niu, Z. Using moderate-resolution temporal NDVI profiles for high-resolution crop mapping in years of absent ground reference data: A case study of Bole and Manas counties in Xinjiang, China. *ISPRS International Journal of Geo-Information*, 5:67, 2016. doi: 10.3390/ijgi5050067.

Harfenmeister, K., Spengler, D., and Itzerott, S. A progressive crop-type classification using multitemporal remote sensing data and phenological information. *PFG - Journal of Photogrammetry, Remote Sensing and Geoinformation Science*, 86, 2018. doi: 10.1007/s41064-018-0050-7.

Heil, K., Lehner, A., and Schmidhalter, U. Influence of climate conditions on the temporal development of wheat yields in a long-term experiment in an area with Pleistocene loess. *Climate*, 8, 2020. doi: 10.3390/cli8090100.

Hernández-Barrera, S. and Rodriguez-Puebla, C. Wheat yield in Spain and associated solar radiation patterns: Wheat yield and solar radiation. *International Journal of Climatology*, 01 2017. doi: 10.1002/joc.4975.

Herrmann, I., Pimstein, A., Karnieli, A., Cohen, Y., Alchanatis, V., and Bonfil, D. LAI assessment of wheat and potato crops by VENμS and Sentinel-2 bands. *Remote Sensing of Environment*, 115:2141–2151, 2011. doi: 10.1016/j.rse.2011.04.018.

Huang, L., Yu, X., and Zuo, X. Edge detection in UAV remote sensing images using the method integrating Zernike moments with clustering algorithms. *International Journal of Aerospace Engineering*, 2017:1–7, 2017. doi: 10.1155/2017/1793212.

Humbold State University. GSP 2016: Introduction to remote sensing, 2020. URL `http://gis.humboldt.edu/OLM/Courses/GSP_216_Online/lesson6-2/metrics.html`. [Online; accessed 25-January-2020].

Hunt, M., Blackburn, A., Carrasco, L., Redhead, J., and Rowland, C. High resolution wheat yield mapping using sentinel-2. *Remote Sensing of Environment*, 233:111410, 11 2019. doi: 10.1016/j.rse.2019.111410.

Idso, S. B., Schmugge, T. J., Jackson, R. D., and Reginato, R. J. The utility of surface temperature measurements for the remote sensing of surface soil water status. *Journal of Geophysical Research (1896-1977)*, 80(21):3044–3049, 1975. doi: 10.1029/JC080i021p03044.

Immitzer, M., Vuolo, F., and Atzberger, C. First experience with Sentinel-2 data for crop and tree species classifications in central Europe. *Remote Sensing*, 8:166, 2016. doi: 10.3390/rs8030166.

IPATE, G., Voicu, G., and Dinu, I. Research on the use of drones in precision agriculture. *U.P.B. Sci. Bull., Series D*, 77:263–274, 2015.

Jeevalakshmi, D., Reddy, S., and Manikiam, B. Land surface temperature retrieval from Landsat data using emissivity estimation. *International Journal of Applied Engineering Research*, 12:9679–9687, 2017. doi: 10.1080/01431160110115041.

Kamble, B., Kilic, A., and Hubbard, K. Estimating crop coefficients using remote sensing-based vegetation index. *Remote Sensing, vol. 5, issue 4, pp. 1588-1602*, 5: 1588–1602, 2013. doi: 10.3390/rs5041588.

Khabbazan, S., Vermunt, P., Steele-Dunne, S., Arntz, L., Marinetti, C., Valk, D., Iannini, L., Molijn, R., Westerdijk, C., and Sande, C. Crop monitoring using Sentinel-1 data: A case study from the Netherlands. *Remote Sensing*, 11:1887, 2019. doi: 10.3390/rs11161887.

Khan, M. A., Stockle, C., Nelson, R., Peters, R., Adam, J., Lamb, B., Chi, J., and Waldo, S. Estimating biomass and yield using METRIC evapotranspiration and simple growth algorithms. *Agronomy journal*, 111, 2018. doi: 10.2134/agronj2018.04.0248.

Lakshmi, V., Jackson, T., and Zehrfuhs, D. Soil moisture-temperature relationships: Results from two field experiments. *Hydrological Processes*, 17, 2003. doi: https://doi.org/10.1002/hyp.1275.

Lepot, M., Aubin, J.-B., and Clemens, F. Interpolation in time series: An introductive overview of existing methods, their performance criteria and uncertainty assessment. *Water*, 9:796, 2017. doi: 10.3390/w9100796.

LfStat. Statistische Berichte - a5113 201700: Flächenerhebung. In *Art d. tatsächlichen Nutzung in Bayern zum Stichtag 31.* Bayerisches Landesamt für Statistik (LfStat), 2017.

Li, B., Ti, C., Zhao, Y., and Yan, X. Estimating soil moisture with Landsat data and its application in extracting the spatial distribution of winter flooded paddies. *Remote Sensing*, 8:38, 2016. doi: 10.3390/rs8010038.

Li, Z.-L., Tang, R., Wan, Z., bi, Y., Zhou, C., Tang, B., Yan, G., and Zhang, X. A review of current methodologies for regional evapotranspiration estimation from remotely sensed data. *Sensors (Basel, Switzerland)*, 9:3801–53, 2009. doi: https://doi.org/10.3390/s90503801.

Liang, M., Pause, M., Prechtel, N., and Schramm, M. Regionalization of coarse scale soil moisture products using fine-scale vegetation indices-prospects and case study. *Remote Sensing*, 2020. doi: 10.3390/rs12030551.

Liang, S., Fang, H., Hoogenboom, G., Teasdale, J., and Cavigelli, M. Estimation of crop yield at the regional scale from MODIS observations. In *International Geoscience and Remote Sensing Symposium (IGARSS)*, volume 3, pages 1625 – 1628 vol.3, 2004. doi: 10.1109/IGARSS.2004.1370640.

Lilienthal, H. Optical sensors in agriculture: Principles and concepts. *Journal für Kulturpflanzen*, 66:34–41, 2014. doi: https://doi.org/10.5073/JfK.2014.02.01.

Lobell, D., Nicholas, K., and Field, C. Weather-based yield forecasts developed for 12 California crops. *California Agriculture*, 60:211–215, 2006. doi: 10.3733/ca.v060n04p211.

Lösch, M. Maschinelles Lernen und Fruchtartenklassifizierung mittels multitemporaler Fernerkundungsdaten. Master's thesis, Technical University of Munich, 2019. [Unpublished].

Ma, L., Li, M., Ma, X., Cheng, L., Du, P., and Liu, Y. A review of supervised object-based land-cover image classification. *ISPRS Journal of Photogrammetry and Remote Sensing*, 130:277 – 293, 2017. doi: https://doi.org/10.1016/j.isprsjprs.2017.06.001.

Main-Knorn, M., Pflug, B., Louis, J., Debaecker, V., Müller-Wilm, U., and Gascon, F. Sen2Cor for Sentinel-2. In *Proc. SPIE 10427, Image and Signal Processing for Remote Sensing XXIII*, 2017. doi: 10.1117/12.2278218.

Mallick, K., Bhattacharya, B., and Patel, N. Estimating volumetric surface moisture content for cropped soils using a soil wetness index based on surface temperature and NDVI. *Agricultural and Forest Meteorology*, 149:1327–1342, 2009. doi: https://doi.org/10.1016/j.agrformet.2009.03.004.

Manfreda, S., Brocca, L., Moramarco, T., Melone, F., and Sheffield, J. A physically based approach for the estimation of root-zone soil moisture from surface measurements. *Hydrology and Earth System Sciences*, 18:1199–1212, 2014. doi: 10.5194/hess-18-1199-2014.

Marszalek, M., Lösch, M., Körner, M., and Schmidhalter, U. Multi-temporal crop type and field boundary classification with Google Earth Engine. *Preprints*, 2020. doi: 10.20944/preprints202004.0316.v1. [PREPRINT].

Masoud, K., Persello, C., and Tolpekin, V. Delineation of agricultural field boundaries from Sentinel-2 images using a novel super-resolution contour detector based on fully convolutional networks. *Remote Sensing*, 12:59, 2020. doi: 10.3390/rs12010059.

Maus, V., Câmara, G., Souza, R., Ipia, A., Ramos, F., and Queiroz, G. A time-weighted dynamic time warping method for land-use and land-cover mapping. *IEEE Journal of*

Selected Topics in Applied Earth Observations and Remote Sensing, 9:3729–3739, 2016. doi: 10.1109/JSTARS.2016.2517118.

Mazzia, V., Khaliq, A., and Chiaberge, M. Improvement in land cover and crop classification based on temporal features learning from Sentinel-2 data using recurrent-convolutional neural network (R-CNN). *Applied Sciences*, 10:238, 2019. doi: 10.3390/app10010238.

McShane, R., Driscoll, K., and Sando, R. A review of surface energy balance models for estimating actual evapotranspiration with remote sensing at high spatiotemporal resolution over large extents. Technical report, U.S. Geological Survey, 2017.

Mercier, A., Betbeder, J., Rapinel, S., Jegou, N., Baudry, J., and Hubert-Moy, L. Evaluation of Sentinel-1 and -2 time series for estimating LAI and biomass of wheat and rapeseed crop types. *Journal of Applied Remote Sensing*, 14:1, 2020. doi: 10.1117/1.JRS.14.024512.

Merzouki, A. and McNairn, H. A hybrid (multi-angle and multi-polarization) approach to soil moisture retrieval using the integral equation model: Preparing for the RADARSAT constellation mission. *Canadian Journal of Remote Sensing*, 41:00–00, 2015. doi: 10.1080/07038992.2015.1104629.

Merzouki, A., McNairn, H., and Pacheco, A. Mapping soil moisture using RADARSAT-2 data and local autocorrelation statistics. *IEEE Journal of Selected Topics in Applied Earth Observations and Remote Sensing*, 4:128 – 137, 2011. doi: 10.1109/JSTARS.2011.2116769.

Mistele, B. and Schmidhalter, U. Tractor-based quadrilateral spectral reflectance measurements to detect biomass and total aerial nitrogen in winter wheat. *Agronomy Journal - AGRON J*, 102, 2010. doi: 10.2134/agronj2009.0282.

Moreira, A. and Krieger, G. Spaceborne Synthetic Aperture Radar (SAR) systems: State of the art and future developments. In *Microwave Conference*, pages 101 – 104, 2003. doi: 10.1109/EUMA.2003.340900.

Mori, U., Mendiburu, A., Dasgupta, S., and Lozano, J. A. Early classification of time series by simultaneously optimizing the accuracy and earliness. *IEEE Transactions on Neural Networks and Learning Systems*, 29(10):4569–4578, 2018.

Moriasi, D., Gitau, M., Pai, N., and Daggupati, P. Hydrologic and water quality models: Performance measures and evaluation criteria. *Transactions of the ASABE (American Society of Agricultural and Biological Engineers)*, 58:1763–1785, 12 2015. doi: 10.13031/trans.58.10715.

Mueller, M., Segl, K., and Kaufmann, H. Edge- and region-based segmentation technique for the extraction of large, man-made objects in high-resolution satellite imagery. *Pattern Recognition*, 37:1619–1628, 2004. doi: 10.1016/j.patcog.2004.03.001.

NASA. Terra/Aqua MODIS, 2020. URL `https://ladsweb.modaps.eosdis.nasa.gov`. [Online; accessed 12-August-2020].

Nasrallah, A., Baghdadi, N., El Hajj, M., Darwish, T., Belhouchette, H., Faour, G., Darwich, S., and Mhawej, M. Sentinel-1 data for winter wheat phenology monitoring and mapping. *Remote Sensing*, 11:2228, 2019. doi: 10.3390/rs11192228.

Natteshan, N. and Kumar, N. Effective SAR image segmentation and classification of crop areas using MRG and CDNN techniques. *European Journal of Remote Sensing*, pages 1–15, 2020. doi: 10.1080/22797254.2020.1727777.

Nitze, I., Schulthess, U., and Asche, H. Comparison of machine learning algorithms, random forest, artificial neural network and support vector machine to maximum likelihood for supervised crop type classification. In *GEOBIA*, Rio de Janeiro, 2012.

Orynbaikyzy, A., Gessner, U., and Conrad, C. Crop type classification using a combination of optical and radar remote sensing data: A review. *International Journal of Remote Sensing*, 40(17):6553–6595, 2019. doi: 10.1080/01431161.2019.1569791.

Paloscia, S., Pettinato, S., Santi, E., Notarnicola, C., Pasolli, L., and Reppucci, A. Soil moisture mapping using Sentinel-1 images: Algorithm and preliminary validation. *Remote Sensing of Environment*, 134:234, 2013. doi: 10.1016/j.rse.2013.02.027.

Pan, H., Chen, Z., Allard, d., and Ren, J. Joint assimilation of leaf area index and soil moisture from Sentinel-1 and Sentinel-2 data into the WOFOST model for winter wheat yield estimation. *Sensors*, 19:3161, 2019. doi: 10.3390/s19143161.

Pasolli, L., Notarnicola, C., Bertoldi, G., Bruzzone, L., Remelgado, R., Greifeneder, F., Niedrist, G., Della Chiesa, S., Tappeiner, U., and Zebisch, M. Estimation of soil moisture in mountain areas using SVR technique applied to multiscale active radar images at C-band. *IEEE Journal of Selected Topics in Applied Earth Observations and Remote Sensing*, 8:262–283, 2015. doi: 10.1109/JSTARS.2014.2378795.

Pedregosa, F., Varoquaux, G., Gramfort, A., Michel, V., Thirion, B., Grisel, O., Blondel, M., Prettenhofer, P., Weiss, R., Dubourg, V., Vanderplas, J., Passos, A., Cournapeau, D., Brucher, M., Perrot, M., Duchesnay, E., and Louppe, G. Scikit-learn: Machine learning in Python. *Journal of Machine Learning Research*, 12, 2012. URL `https://arxiv.org/abs/1201.0490`.

Peng, B., Guan, K., Tang, J., Ainsworth, E., Asseng, S., Bernacchi, C., Cooper, M., Delucia, E., Elliott, J., Ewert, F., Grant, R., Gustafson, D., Hammer, G., Jin, Z., Jones, J., Kimm, H., Lawrence, D., Li, Y., Lombardozzi, D., and Wang, Z. Towards a multiscale crop modelling framework for climate change adaptation assessment. *Nature Plants*, 6:338–348, 2020a. doi: 10.1038/s41477-020-0625-3.

Peng, B., Guan, K., Wang, Z., Jiang, C., Frankenberg, C., Sun, Y., He, L., and Köhler, P. Assessing the benefit of satellite-based solar-induced chlorophyll fluorescence in crop yield prediction. *International Journal of Applied Earth Observation and Geoinformation*, 90:102126, 2020b. doi: 10.1016/j.jag.2020.102126.

Petitjean, F., Inglada, J., and Gancarski, P. Satellite image time series analysis under time warping. *IEEE Transactions on Geoscience and Remote Sensing*, 50:3081–3095, 2012. doi: 10.1109/TGRS.2011.2179050.

Pierdicca, N., Pulvirenti, L., and Pace, G. A prototype software package to retrieve soil moisture from Sentinel-1 data by using a Bayesian multitemporal algorithm. *Selected Topics in Applied Earth Observations and Remote Sensing, IEEE Journal of*, 7:153–166, 2014. doi: 10.1109/JSTARS.2013.2257698.

Prasad, B., Carver, B., Stone, M., Babar, M., Raun, W., and Klatt, A. Potential use of spectral reflectance indices as a selection tool for grain yield in winter wheat under great plains conditions. *Reproduced from Crop Science. Published by Crop Science Society of America CROP SCIENCE*, 47, 01 2007. doi: 10.2135/cropsci2006.07.0492.

Prey, L. and Schmidhalter, U. Temporal and spectral optimization of vegetation indices for estimating grain nitrogen uptake and late-seasonal nitrogen traits in wheat. *Sensors*, 19:4640, 2019a. doi: 10.3390/s19214640.

Prey, L. and Schmidhalter, U. Simulation of satellite reflectance data using high-frequency ground based hyperspectral canopy measurements for in-season estimation of grain yield and grain nitrogen status in winter wheat. *Isprs Journal of Photogrammetry and Remote Sensing*, 149:176–187, 2019b.

Py6S. A Python interface to 6S, 2020. URL `https://py6s.readthedocs.io/en/latest/`. [Online; accessed 21-July-2020].

Pérez-Ruiz, M. and Upadhyaya, S. *GNSS in precision agricultural operation*. IntechOpen, 2012. doi: 10.13140/2.1.4162.3362.

R., P., Anupashsha, R., Kumar, S., Saha, s., and Dadhwal, V. Assessing potential of MODIS derived temperature/vegetation condition index (TVDI) to infer soil moisture status. *International Journal of Remote Sensing*, 30:23–39, 2009. doi: https://doi.org/10.1080/01431160802108497.

Remelgado, R., Zaitov, S., Kenjabaev, S., Stulina, G., Sultonov, M., Ibrakhimov, M., Akhmedov, M., Dukhovny, V., and Conrad, C. A crop type dataset for consistent land cover classification in central Asia. *Scientific Data*, 7, 2020. doi: https://doi.org/10.1038/s41597-020-00591-2.

Revill, A., Florence, A., MacArthur, A., Hoad, S., Rees, B., and Williams, M. Quantifying uncertainty and bridging the scaling gap in the retrieval of leaf area index by coupling Sentinel-2 and UAV observations. *Remote Sensing*, 12:1843, 2020. doi: 10.3390/rs12111843.

Rischbeck, P., Elsayed, S., Mistele, B., Barmeier, G., Heil, K., and Schmidhalter, U. Data fusion of spectral, thermal and canopy height parameters for improved yield prediction of drought stressed spring barley. *European Journal of Agronomy*, 78:44–59, 2016. doi: 10.1016/j.eja.2016.04.013.

Roerink, G., Su, Z., and Menenti, M. S-SEBI: A simple remote sensing algorithm to estimate the surface energy balance. *Physics and Chemistry of the Earth, Part B: Hydrology, Oceans and Atmosphere*, 25:147–157, 2000. doi: 10.1016/S1464-1909(99)00128-8.

Rouse, J., Haas, R., Scheel, J., and Deering, D. Monitoring vegetation systems in the great plains with ERTS. In *3rd Earth Resource Technology Satellite-1 (ERTS) Symposium*, page 301–317, 1974.

Rußwurm, M., Tavenard, R., Lefévre, S., and Körner, M. Early classification for agricultural monitoring from satellite time series. In *International Conference on Machine Learning AI for Social Good Workshop*, 2019. URL `https://arxiv.org/abs/1908.10283`.

Rußwurm, M., Lefévre, S., and Körner, M. BreizhCrops: A satellite time series dataset for crop type identification. *Remote Sensing and Spatial Information Sciences ISPRS*, 2020. URL `https://arxiv.org/abs/1905.11893v`.

Rydberg, A. and Borgefors, G. Integrated method for boundary delineation of agricultural fields in multispectral satellite images. *Geoscience and Remote Sensing, IEEE Transactions on*, 39:2514 – 2520, 2001. doi: 10.1109/36.964989.

Saini, R. and Ghosh, S. Crop classification on single date Sentinel-2 imagery using random forest and support vector machine. *Int. Arch. Photogramm. Remote Sens. Spatial Inf. Sci*, pages –5, 683–688, 2018. doi: 10.5194/isprs-archives-XLII-5-683-2018.

Saiz-Rubio, V. and Rovira-Más, F. From smart farming towards agriculture 5.0: A review on crop data management. *Agronomy*, 10, 2020. doi: https://doi.org/10.3390/agronomy10020207.

Sandholt, I., Rasmussen, K., and Andersen, J. A simple interpretation of the surface temperature/vegetation index space for assessment of surface moisture status. *Remote Sensing of Environment*, 79:213–224, 2002. doi: 10.1016/S0034-4257(01)00274-7.

Schlenker, W. and Roberts, M. Nonlinear temperature effects indicate severe damages to U.S. crop yields under climate change. In *Proceedings of the National Academy of Sciences of the United States of America*, volume 106, pages 15594–8, 2009. doi: 10.1073/pnas.0906865106.

Schmidhalter, U., Maidl, F.-X., Heuwinkel, H., Demmel, M., Auernhammer, H., Noack, P., and Rothmund, M. Precision farming — adaptation of land use management to small scale heterogeneity. *Perspectives for Agroecosystem Management: Balancing Environmental and Socio-Economic Demands*, pages 121–425, 2008. doi: https://doi.org/10.1016/B978-044451905-4.50007-6.

Schultz, B., Immitzer, M., Formaggio, A., Sanches, I., Luiz, A., and Atzberger, C. Self-guided segmentation and classification of multi-temporal Landsat 8 images for crop type mapping in southeastern Brazil. *Remote Sensing*, 7:14482–14508, 2015. doi: 10.3390/rs71114482.

Sekertekin, A. and Bonafoni, S. Land surface temperature retrieval from Landsat 5, 7, and 8 over rural areas: Assessment of different retrieval algorithms and emissivity models and toolbox implementation. *Remote Sensing*, 12:294, 2020. doi: https://doi.org/10.3390/rs12020294.

Senay, G., Kagone, S., Singh, R., Gowda, P., Velpuri, N. M., Alemu, H., and Verdin, J. Operational evapotranspiration mapping using remote sensing and weather datasets: A new parameterization for the SSEB approach. *JAWRA Journal of the American Water Resources Association*, 49:577–591, 2013. doi: 10.1111/jawr.12057.

Senkondo, W., Munishi, S., Tumbo, M., Nobert, J., and Lyon, S. Comparing remotely-sensed surface energy balance evapotranspiration estimates in heterogeneous and data-limited regions: A case study of Tanzania's Kilombero valley. *Remote Sensing*, 11:1289, 2019. doi: 10.3390/rs11111289.

Sentinel Hub. Sentinel Hub's cloud detector for Sentinel-2 imagery — Github repository, 2020. URL `https://github.com/sentinel-hub/sentinel2-cloud-detector`. [Online; accessed 21-July-2020].

Serrano, J., Shahidian, S., and Marques Da Silva, J. Evaluation of normalized difference water index as a tool for monitoring pasture seasonal and inter-annual variability in a Mediterranean agro-silvo-pastoral system. *Water*, 11:62, 2019. doi: https://doi.org/10.3390/w11010062.

Shelia, V., Hansen, J., Sharda, V., Porter, C., Aggarwal, P., Wilkerson, C. J., and Hoogenboom, G. A multi-scale and multi-model gridded framework for forecasting crop production, risk analysis, and climate change impact studies. *Environmental Modelling & Software*, 115:144 – 154, 2019. doi: https://doi.org/10.1016/j.envsoft.2019.02.006.

Shi, W., Tao, F., and Zhang, Z. A review on statistical models for identifying climate contributions to crop yields. *Journal of Geographical Sciences*, 23, 2013. doi: 10.1007/s11442-013-1029-3.

Sishodia, R., Ray, R., and Singh, S. Applications of remote sensing in precision agriculture: A review. *Remote Sensing*, 12:3136, 2020. doi: 10.3390/rs12193136.

Skakun, S., Vermote, E., Franch, B., Roger, J.-C., Kussul, N., Ju, J., and Masek, J. Winter wheat yield assessment from Landsat 8 and Sentinel-2 data: Incorporating surface reflectance, through phenological fitting, into regression yield models. *Remote Sensing*, 11:1768, 2019. doi: 10.3390/rs11151768.

Sousa, V., Salami, G., Silva, M., Silva, E., Júnior, J., and Alba, E. Methodological evaluation of vegetation indexes in land use and land cover (LULC) classification. *Geology, Ecology, and Landscapes*, 2019. doi: 10.1080/24749508.2019.1608409.

StMELF. Government report on agriculture 2018, 2020. URL `https://www.agrarbericht-2018.bayern.de/landwirtschaft-laendliche-entwicklung/getreide.html`. [Online; accessed 21-July-2020].

Sun, Z., Wei, B., Su, W., Shen, W., Wang, C., You, D., and Liu, Z. Evapotranspiration estimation based on the SEBAL model in the Nansi lake wetland of China. *Mathematical and Computer Modelling*, 54:1086–1092, 2011. doi: 10.1016/j.mcm.2010.11.039.

Tadesse, T., Senay, G. B., Berhan, G., Regassa, T., and Beyene, S. Evaluating a satellite-based seasonal evapotranspiration product and identifying its relationship with other satellite-derived products and crop yield: A case study for Ethiopia. *International Journal of Applied Earth Observation and Geoinformation*, 40:39 – 54, 2015a. doi: https://doi.org/10.1016/j.jag.2015.03.006.

Tadesse, T., Senay, G. B., Berhan, G., Regassa, T., and Beyene, S. Evaluating a satellite-based seasonal evapotranspiration product and identifying its relationship with other satellite-derived products and crop yield: A case study for Ethiopia. *International Journal of Applied Earth Observation and Geoinformation*, 40:39–54, 2015b. doi: https://doi.org/10.1016/j.jag.2015.03.006.

The University of Arizona. AZMET - The Arizona meteorological network, 2020. URL `https://cals.arizona.edu/azmet/`. [Online; accessed 24-July-2020].

Tricht, K., Gobin, A., Gilliams, S., and Piccard, I. Synergistic use of radar Sentinel-1 and optical Sentinel-2 imagery for crop mapping: A case study for Belgium. *Remote Sensing*, 10:1642, 2018. doi: 10.3390/rs10101642.

USGS. Landsat-7 — United States Geological Survey, 2020. URL `https://www.usgs.gov/land-resources/nli/landsat/landsat-7`. [Online; accessed 12-August-2020].

Vuolo, F., D'Urso, G., De Michele, C., Bianchi, B., and Cutting, M. Satellite-based irrigation advisory services: A common tool for different experiences from Europe to Australia. *Agricultural Water Management*, 147:82–95, 2015a. doi: 10.1016/j.agwat.2014.08.004.

Vuolo, F., Essl, L., and Atzberger, C. Costs and benefits of satellite-based tools for irrigation management. *Frontiers in Environmental Science*, 3, 2015b. doi: https://doi.org/10.3389/fenvs.2015.00052.

Vuolo, F., Neuwirth, M., Immitzer, M., Atzberger, C., and Ng, W.-T. How much does multi-temporal Sentinel-2 data improve crop type classification? *International Journal of Applied Earth Observation and Geoinformation*, 72:122–130, 2018. doi: 10.1016/j.jag.2018.06.007.

Wagner, W., Sabel, D., Doubkova, M., Bartsch, A., and Pathe, C. The potential of Sentinel-1 for monitoring soil moisture with a high spatial resolution at global scale. In *Earth Observation and Water Cycle Science*. ESA, 2010.

Waldner, F. and Diakogiannis, F. Deep learning on edge: Extracting field boundaries from satellite images with a convolutional neural network, 2019. URL `http://arxiv.org/pdf/1910.12023v1.`

Wang, A., Tran, C., Desai, N., Lobell, D., and Ermon, S. Deep transfer learning for crop yield prediction with remote sensing data. In *1st ACM SIGCAS Conference*, pages 1–5, 2018. doi: 10.1145/3209811.3212707.

Watkins, B. and Niekerk, A. A comparison of object-based image analysis approaches for field boundary delineation using multi-temporal Sentinel-2 imagery. *Computers and Electronics in Agriculture*, 158:294–302, 2019a. doi: 10.1016/j.compag.2019.02.009.

Watkins, B. and Niekerk, A. Automating field boundary delineation with multi-temporal Sentinel-2 imagery. *Computers and Electronics in Agriculture*, 167:105078, 2019b. doi: 10.1016/j.compag.2019.105078.

Watkins, B. and Van Niekerk, A. A comparison of object-based image analysis approaches for field boundary delineation using multi-temporal Sentinel-2 imagery. *Computers and Electronics in Agriculture*, 158:294–302, 2019. doi: 10.1016/j.compag.2019.02.009.

Wei, L., Yu, M., Liang, Y., Yuan, Z., Huang, C., Li, R., and Yu, Y. Precise crop classification using spectral-spatial-location fusion based on conditional random fields for UAV-borne hyperspectral remote sensing imagery. *Remote Sensing*, 11, 2019. doi: 10.3390/rs11172011.

Wheeler, T., Hong, T., Ellis, R., Batts, G., Morison, J., and Hadley, P. The duration and rate of grain growth, and harvest index, of wheat (Triticum aestivum L.) in response

to temperature and CO2. *Journal of Experimental Botany - J EXP BOT*, 47:623–630, 05 1996. doi: 10.1093/jxb/47.5.623.

Wikipedia contributors. Earth Observing-1 — Wikipedia, the free encyclopedia, 2020a. URL `https://en.wikipedia.org/w/index.php?title=Earth_Observing-1&oldid=980359761`. [Online; accessed 12-August-2020].

Wikipedia contributors. Landsat 8 — Wikipedia, the free encyclopedia, 2020b. URL `https://en.wikipedia.org/w/index.php?title=Landsat_8&oldid=977412442`. [Online; accessed 12-August-2020].

Wikipedia contributors. Sentinel-1 — Wikipedia, the free encyclopedia, 2020c. URL `https://en.wikipedia.org/w/index.php?title=Sentinel-1&oldid=982920389`. [Online; accessed 12-August-2020].

Wikipedia contributors. Sentinel-2 — Wikipedia, the free encyclopedia, 2020d. URL `https://en.wikipedia.org/w/index.php?title=Sentinel-2&oldid=980206636`. [Online; accessed 12-August-2020].

Wikipedia contributors. Sentinel-3 — Wikipedia, the free encyclopedia, 2020e. URL `https://en.wikipedia.org/w/index.php?title=Sentinel-3&oldid=976808980`. [Online; accessed 12-August-2020].

Xu, Z., Baojie, X., and Guoxin, W. Canny edge detection based on OpenCV. In *13th IEEE International Conference on Electronic Measurement & Instruments (ICEMI) 2017*, Yangzhou, China, 10/20/2017. S.l. ISBN 978-1-5090-5035-2.

Yan, L. and Roy, D. Automated crop field extraction from multi-temporal web enabled Landsat data. *Remote Sensing of Environment*, 144:42–64, 2014. doi: 10.1016/j.rse.2014.01.006.

Yellasiri, R., Tu, S., Poornima, B., and Kalyani, B. Segmentation and object recognition using edge detection techniques. *International Journal of Computer Science and Information Technology*, 2:153–161, 2010. doi: 10.5121/ijcsit.2010.2614.

Zhang, D., Tang, R., Zhao, W., Tang, B., Wu, H., Shao, K., and Li, Z.-L. Surface soil water content estimation from thermal remote sensing based on the temporal variation of land surface temperature. *Remote Sensing*, 6, 2014. doi: 10.3390/rs6043170.

Zhang, K., Ge, X., Shen, P., Li, W., Liu, X.-J., Cao, Q., Zhu, Y., Cao, Q., and Tian, Y. Predicting rice grain yield based on dynamic changes in vegetation indexes during early to mid-growth stages. *Remote Sensing*, 11:387, 2019. doi: 10.3390/rs11040387.

Zhao, C., Liu, B., Piao, S., Wang, X., Lobell, D., Huang, Y., Huang, M., Yao, Y., Bassu, S., Ciais, P., Durand, J.-L., Elliott, J., Ewert, F., Janssens, I., Li, T., Lin, E., Liu, Q., Martre, P., Müller, C., and Asseng, S. Temperature increase reduces global yields of major crops in four independent estimates. *Proceedings of the National Academy of Sciences*, 114:201701762, 2017. doi: 10.1073/pnas.1701762114.

A List with publications

Poster presentation	
Title	Satellitengestützte Bewässerung & Digitalisierung der Landwirtschaft
Authors	**Michael Marszalek**, Urs Schmidhalter
Conference	PFGK18: Photogrammetrie - Fernerkundung - Geoinformatik - Kartographie - 2018
Objective	The high temporal availability of satellite data in combination with cloud technologies enables the implementation of new applications. In this context, a precision irrigation solution was developed to save water while optimising yields.
Results and conclusions	Automated processing and analysis with machine learning in the Google cloud and the availability of free satellite data was a novelty and enabled the automation of what was until recently a cost-intensive work.
Contributions	Management and implementation of the software; professional support from the co-author on irrigation issues.

Preprint	
Title	Multi-temporal Crop Type and Field Boundary Classification with Google Earth Engine (Preprint)
Authors	**Michael Marszalek**, Maximilian Lösch, Marco Körner, Urs Schmidhalter
Archiv	www.preprints.org, doi: 10.20944/preprints202004.0316.v1

Objectives	The aim of the study includes an efficient and reproducible implementation of a crop-type and field boundary classification. This is an intermediate step for yield prediction at the field level. In this context, the following experiments were investigated: 1) Comparison of crop-type classification with SVM and RF in combination with various features. 2) Classification of crop types in 2018 based on a model with data from 2016 and 2017. 3) A robust field boundary detection.
Results and conclusions	The results showed that the usage of all raw bands of Sentinel-2 outperformed an index-based approach. The 13 bands provided more insights and separated the crop types with accuracies up to 92%. Random forest achieved better results than support vector machines. Field boundary detection with $NDWI$ achieved a producer accuracy of 81% and an user accuracy of 79% and can be used for regions without national available field boundaries.
Contributions	Management and partial implementation of the basic concept and analysis of the results; writing of the manuscript with contributions of the co-authors; implementation of the first software and related results were realised by a co-author in the scope of a master thesis.

Submitted

Title	Early crop-type mapping under climate anomalies
Authors	**Michael Marszalek**, Maximilian Lösch, Marco Körner, Urs Schmidhalter

Objectives	The study was based on the previously listed preprint and clarified the following questions: 1) Is index-based classification or the use of raw bands better for classification? 2) Can crop types be classified well in a year without labels and based on observations from previous years? 4) What accuracy is achieved depending on the classification time within a vegetation period?
Results and conclusions	The results showed that the use of the raw bands achieved higher accuracies. A prediction based on data from previous years in a year with unusual climatological conditions and without labels also achieved valid results. The prediction depending on the time within a growing season needed satellite observations until July to classify most of the crop types with the best possible accuracy.
Contributions	Management and partial implementation of the basic concept; analysis of the results; writing of the manuscript with contributions of the co-authors; implementation of the first software and related results were realised by a co-author in the scope of a master thesis.

To be submitted

Title	Prediction of multi-year winter wheat yields at the field level with satellite and climatological data
Authors	**Michael Marszalek**, Marco Körner, Urs Schmidhalter
Objectives	The aim of the study is to predict winter wheat yields at the field level. The following main objectives were addressed: 1) Generation of a daily satellite-based water requirement (CWR) for each field using Penman and inclusion in the yield prediction. 2) Comparison of climatological data, raw bands, indices and value-based information (CWR, ET_c) from Sentinel-2.

Results and conclusions	The results showed that climatological data alone is no more appropriate than using satellite data alone. Combining climatological data with satellite data increased the yield prediction accuracy. The CWR-based approach proved to be slightly worse than using all raw bands, ET_0 and precipitation. This simplified feature combination eased the implementation and achieved a R^2 of 0.84 with a RMSE of 5.63 $\mathrm{dt\,ha^{-1}}$.
Contributions	Implementation of the basic concept and analysis of the results with contributions of the co-authors; writing of the manuscript with contributions of the co-authors.

B Supplementary material

B.1 Crop-type mapping with SVM

Table B.1: Classification with SVM and $NDVI$. The last row 'Total' of the confusion matrix shows the amount of ground truth data, while the column 'Total' shows the classification sum.

	Other	**Winter wheat (WW)**	**Winter barley (WB)**	**Winter rapeseed (WR)**	**Maize**	**Potato**	**Sugar beet (SB)**	**Total**	**UA (%)**	**PA (%)**
Other	52	2	4	10	3	1	0	72	72.22	66.67
WW	8	57	5	8	1	1	0	80	71.25	77.03
WB	5	9	62	18	0	0	0	94	65.96	75.61
WR	6	4	9	35	0	0	0	54	64.81	48.61
Maize	4	0	1	1	46	6	10	68	67.65	63.01
Potato	2	2	1	0	4	51	3	63	80.95	71.83
SB	1	0	0	0	19	12	62	94	65.96	82.67
Total	78	74	82	72	73	71	75	525		
									OA	70%
									Kappa	0.84
									CV	0.69

Table B.2: Classification with SVM and all raw bands.

	Other	**Winter wheat (WW)**	**Winter barley (WB)**	**Winter rapeseed (WR)**	**Maize**	**Potato**	**Sugar beet (SB)**	**Total**	**UA (%)**	**PA (%)**
Other	64	5	5	2	5	4	1	86	74.42	82.05
WW	7	64	5	2	0	2	0	80	80	86.49
WB	0	4	70	4	0	0	0	78	89.74	85.37
WR	2	1	1	64	0	1	1	70	91.43	88.89
Maize	1	0	0	0	67	3	0	71	94.37	91.78
Potato	2	0	0	0	1	57	3	63	90.48	80.28
SB	2	0	1	0	0	4	70	77	90.91	93.33
Total	78	74	82	72	73	71	75	525		
									OA	87%
									Kappa	0.88
									CV	0.89

B.2 Crop-type mapping with RF

Table B.3: Classification with RF and $NDVI$. The last row 'Total' of the confusion matrix shows the amount of ground truth data, while the column 'Total' shows the classification sum.

	Other	**Winter wheat (WW)**	**Winter barley (WB)**	**Winter rapeseed (WR)**	**Maize**	**Potato**	**Sugar beet (SB)**	**Total**	**UA (%)**	**PA (%)**
Other	54	0	0	5	2	1	0	62	87.1	69.23
WW	4	54	4	5	1	0	0	68	79.41	72.97
WB	4	7	67	8	0	0	0	86	77.91	81.71
WR	8	12	9	53	1	0	0	83	63.86	73.61
Maize	6	1	2	1	58	10	11	89	65.17	79.45
Potato	2	0	0	0	3	49	6	60	81.67	69.01
SB	0	0	0	0	8	11	58	77	75.32	77.33
Total	78	74	82	72	73	71	75	525		
									OA	75%
									Kappa	0.86
									CV	0.75

Table B.4: Classification with RF and all raw bands.

	Other	**Winter wheat (WW)**	**Winter barley (WB)**	**Winter rapeseed (WR)**	**Maize**	**Potato**	**Sugar beet (SB)**	**Total**	**UA (%)**	**PA (%)**
Other	58	1	1	1	2	1	0	64	90.62	74.36
WW	8	64	4	0	0	0	0	76	84.21	86.49
WB	5	7	73	6	1	0	0	92	79.35	89.02
WR	0	1	4	65	0	0	0	70	92.86	90.28
Maize	1	1	0	0	65	2	3	72	90.28	89.04
Potato	5	0	0	0	4	65	1	75	86.67	91.55
SB	1	0	0	0	1	3	71	76	93.42	94.67
Total	78	74	82	72	73	71	75	525		
									OA	88%
									Kappa	0.92
									CV	0.89

B.3 Crop-type mapping for 2018 with SVM

Table B.5: Classification of crop types in 2018 with SVC, all raw bands and the "Other" class. The model was trained with data from 2016 and 2017.

	Other	Winter wheat (WW)	Winter barley (WB)	Winter rapeseed (WR)	Maize	Potato	Sugar beet (SB)	Total	UA (%)	PA (%)
Other	78	49	60	23	56	83	53	402	19.4	78
WW	0	8	0	1	3	1	1	14	57.14	8
WB	4	10	13	2	2	0	0	31	41.94	13
WR	18	33	27	74	33	10	27	222	33.33	74
Maize	0	0	0	0	6	0	1	7	85.71	6
Potato	0	0	0	0	0	6	6	12	50	6
SB	0	0	0	0	0	0	12	12	100	12
Total	100	100	100	100	100	100	100	700		
									OA	28%
									Kappa	0.08

Table B.6: Classification of crop types in 2018 with SVC, all raw bands and without the "Other" class. The model was trained with data from 2016 and 2017.

	Winter wheat (WW)	Winter barley (WB)	Winter rapeseed (WR)	Maize	Potato	Sugar beet (SB)	Total	UA (%)	PA (%)
WW	39	44	14	21	36	39	193	20.21	39
WB	5	11	2	2	0	0	20	55	11
WR	56	45	84	67	56	42	350	24	84
Maize	0	0	0	10	1	2	13	76.92	10
Potato	0	0	0	0	7	7	14	50	7
SB	0	0	0	0	0	10	10	100	10
Total	100	100	100	100	100	100	600		
								OA	27%
								Kappa	0.12

B.4 Field boundaries

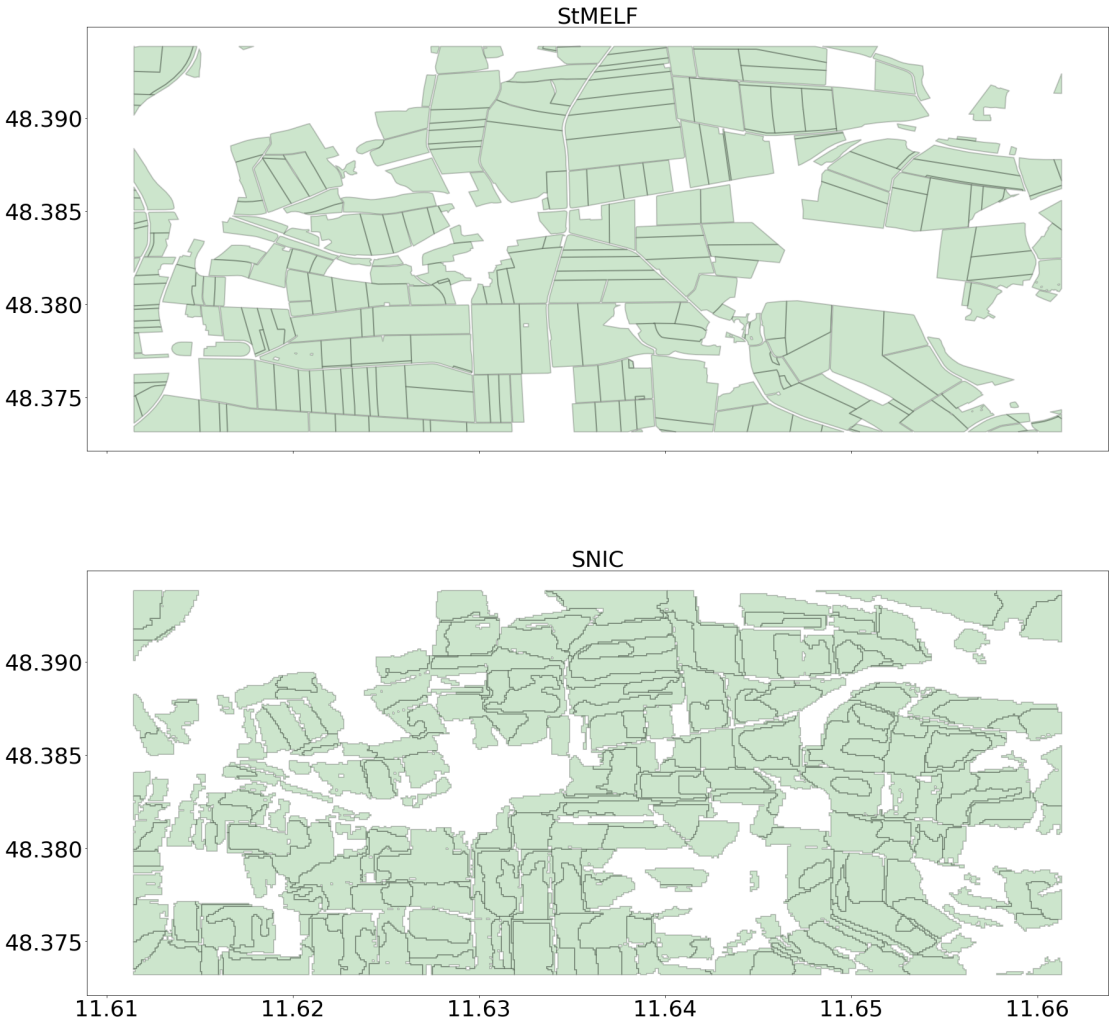

Figure B.1: Comparison of StMELF data and SNIC results.

B.5 Combine harvester yields

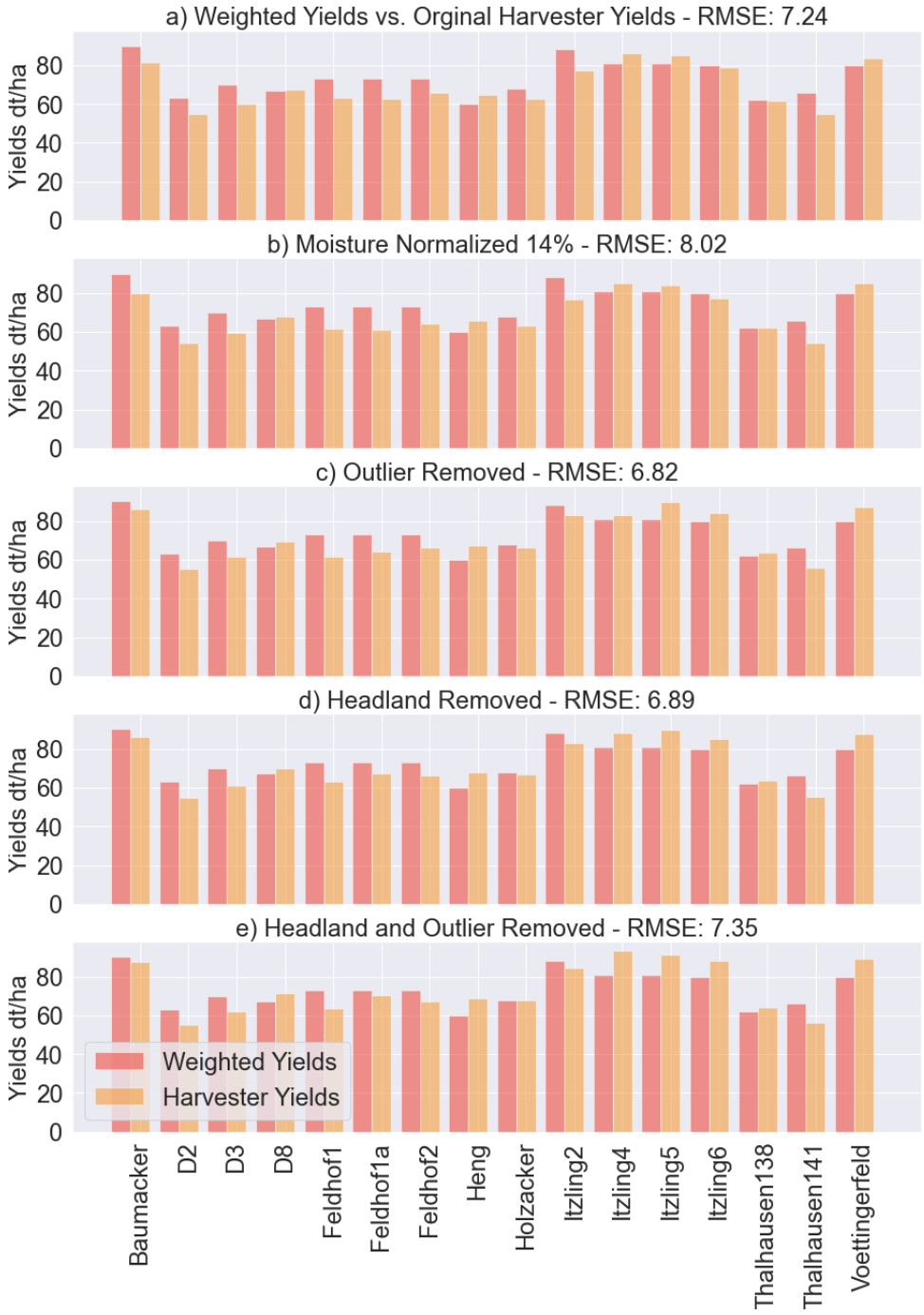

Figure B.2: Comparison of combine harvester records with weighed yields in 2018.

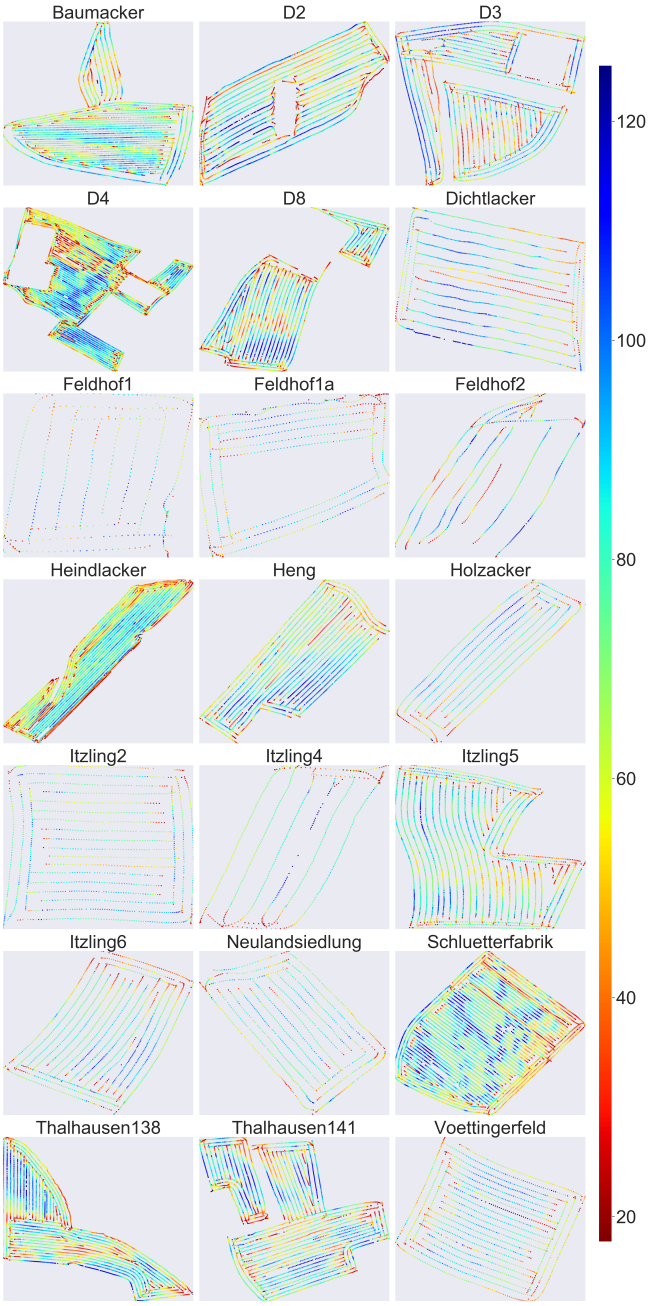

Figure B.3: Winter wheat yield values obtained from the combine harvester in 2018. One field (Moehlacker) was excluded for visualisation consistency.

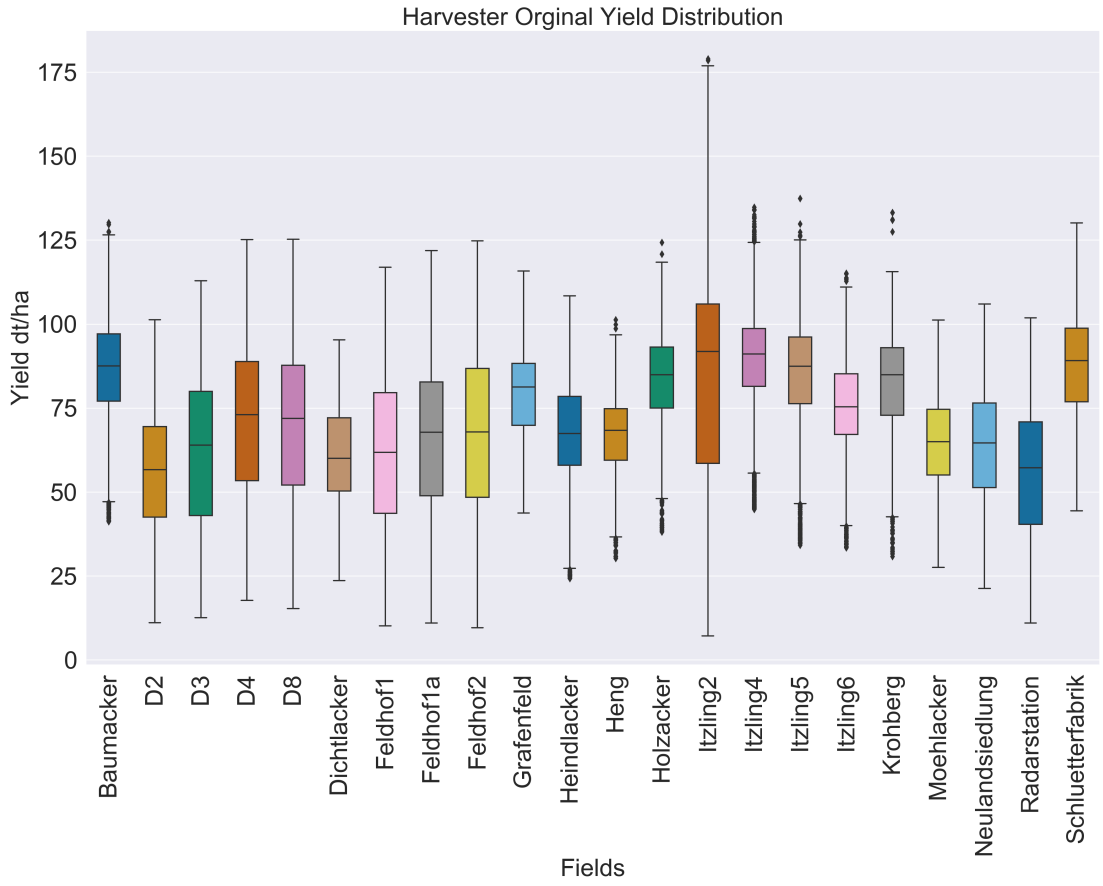

Figure B.4: Box plot for all 22 combine harvester yields, visualising the mean values and variance within a field.

B.6 Summarised results for yield prediction

Table B.7: An overview of all results sorted by the highest R^2 and the corresponding $RMSE$. M. stands for method, Res. for resolution and L. for level. Precipitation is referred to as P and climatological data is referred to as CD.

Features	**M.**	**Res.**	**L.**	R^2	MAE	$RMSE$	CV	$CV\,std$
All features	LR	weekly	2A	0.9	3.65	4.4	0.79	0.06
All features	LR	weekly	1C	0.9	3.21	4.49	0.74	0.11
B1-B12, ET_0, P	LR	weekly	2A	0.84	4.91	5.63	0.72	0.07
B1-B12, ET_0, P	LR	monthly	1C	0.83	3.94	5.78	0.72	0.09
All features	LR	monthly	2A	0.83	4.68	5.78	0.67	0.1
B1-B12	LR	weekly	2A	0.83	4.64	5.78	0.58	0.14
B1-B12, ET_0, P	LR	weekly	1C	0.83	4.85	5.87	0.72	0.06
CD	RF	monthly		0.8	4.26	6.39	0.53	0.11
CWR (K_c:$NDWI$)	LR	weekly	1C	0.79	4.89	6.45	0.62	0.04
B1-B12, ET_0, P	LR	monthly	2A	0.79	5.43	6.45	0.71	0.05
CWR (K_c:$NDWI$)	LR	weekly	2A	0.79	4.92	6.46	0.66	0.07
CD	RF	weekly		0.79	4.44	6.51	0.62	0.08
B1-B12	LR	weekly	1C	0.77	5.63	6.78	0.56	0.09
Δ (K_c:$REIP$)	RF	weekly	1C	0.75	4.74	7.0	0.61	0.06
ET_c (K_c:$NDVI$)	LR	weekly	2A	0.74	5.82	7.15	0.34	0.14
Δ (K_c:$NDRE$)	LR	weekly	2A	0.74	5.4	7.16	0.49	0.18
All features	LR	monthly	1C	0.74	5.29	7.2	0.65	0.1
ET_c (K_c:$REIP$)	RF	weekly	2A	0.74	5.2	7.2	0.52	0.1
Δ (K_c:$REIP$)	RF	weekly	2A	0.74	5.25	7.24	0.5	0.17
Δ (K_c:$NDVI$)	RF	weekly	1C	0.73	5.25	7.28	0.5	0.26
ET_c (K_c:$NDVI$)	LR	weekly	1C	0.73	5.96	7.36	0.51	0.11
CWR (K_c:$REIP$)	RF	monthly	1C	0.73	5.36	7.37	0.61	0.04
ET_c (K_c:$REIP$)	RF	weekly	1C	0.73	5.03	7.37	0.63	0.14
Δ (K_c:$NDRE$)	RF	weekly	2A	0.72	5.25	7.44	0.46	0.13
Δ (K_c:$NDRE$)	RF	weekly	1C	0.72	5.35	7.52	0.48	0.11

Features	**M.**	**Res.**	**L.**	R^2	MAE	$RMSE$	CV	$CV std$
All features	RF	weekly	1C	0.72	5.71	7.53	0.62	0.08
B1-B12	LR	monthly	2A	0.71	5.64	7.55	0.44	0.08
B1-B12	LR	monthly	1C	0.71	6.62	7.55	0.43	0.19
Δ (K_c:$NDWI$)	RF	weekly	2A	0.71	5.71	7.58	0.59	0.1
All features	RF	weekly	2A	0.71	5.8	7.59	0.61	0.08
ET_c (K_c:$REIP$)	LR	weekly	1C	0.71	6.04	7.63	0.61	0.11
Δ (K_c:$NDVI$)	RF	weekly	2A	0.71	5.4	7.63	0.36	0.15
Δ (K_c:$REIP$)	RF	monthly	2A	0.71	5.71	7.64	0.54	0.22
Δ (K_c:$NDWI$)	RF	weekly	1C	0.71	5.67	7.66	0.62	0.04
All features	RF	monthly	1C	0.71	5.67	7.66	0.49	0.08
ET_c (K_c:$REIP$)	RF	monthly	1C	0.7	5.54	7.68	0.37	0.11
CWR (K_c:$REIP$)	RF	weekly	1C	0.7	5.37	7.71	0.71	0.06
Δ (K_c:$NDRE$)	RF	monthly	1C	0.7	5.58	7.73	0.65	0.06
Δ (K_c:$NDWI$)	LR	weekly	1C	0.7	5.94	7.79	0.62	0.11
Δ (K_c:$NDWI$)	LR	weekly	2A	0.7	5.93	7.8	0.47	0.24
CWR (K_c:$NDRE$)	RF	weekly	1C	0.69	5.61	7.85	0.41	0.1
All features	RF	monthly	2A	0.69	5.89	7.86	0.57	0.08
ET_c (K_c:$NDWI$)	LR	weekly	2A	0.69	6.05	7.87	0.33	0.22
Δ (K_c:$NDRE$)	LR	weekly	1C	0.69	5.84	7.92	0.58	0.08
CD	LR	monthly		0.69	5.79	7.92	0.61	0.1
Δ (K_c:$REIP$)	LR	weekly	1C	0.68	5.96	7.95	0.59	0.07
ET_0	RF	weekly		0.68	5.96	7.99	0.61	0.09
CD	LR	weekly		0.68	5.9	7.99	0.43	0.15
CWR (K_c:$NDVI$)	LR	weekly	2A	0.68	6.2	8.01	0.44	0.11
Δ (K_c:$REIP$)	LR	weekly	2A	0.68	5.97	8.03	0.62	0.08
ET_c (K_c:$REIP$)	RF	monthly	2A	0.67	5.98	8.12	0.3	0.15
ET_0	LR	weekly		0.67	6.07	8.17	0.62	0.04
CWR (K_c:$REIP$)	LR	weekly	2A	0.66	6.63	8.2	0.58	0.1
Δ (K_c:$NDVI$)	RF	monthly	1C	0.66	6.34	8.2	0.33	0.17
CWR (K_c:$NDVI$)	RF	monthly	1C	0.66	5.86	8.22	0.46	0.13

Features	**M.**	**Res.**	**L.**	R^2	MAE	$RMSE$	CV	$CV std$
ET_c (K_c:$REIP$)	LR	weekly	2A	0.66	6.33	8.23	0.41	0.01
Δ (K_c:$NDWI$)	RF	monthly	1C	0.65	6.5	8.33	0.51	0.2
B1-B12, ET_0, P	RF	weekly	2A	0.65	6.66	8.34	0.49	0.1
Δ (K_c:$NDWI$)	RF	monthly	2A	0.65	6.45	8.35	0.68	0.1
Δ (K_c:$NDRE$)	RF	monthly	2A	0.65	6.55	8.38	0.41	0.1
B1-B12, ET_0, P	RF	weekly	1C	0.64	6.9	8.42	0.41	0.15
B1-B12	RF	weekly	2A	0.64	6.83	8.46	0.44	0.1
CWR (K_c:$NDWI$)	RF	weekly	2A	0.64	6.26	8.47	0.52	0.2
CWR (K_c:$NDVI$)	RF	weekly	1C	0.64	6.17	8.53	0.39	0.11
CWR (K_c:$NDRE$)	RF	weekly	2A	0.64	6.09	8.53	0.4	0.12
CWR (K_c:$NDWI$)	RF	weekly	1C	0.63	6.32	8.54	0.52	0.18
ET_c (K_c:$NDWI$)	LR	weekly	1C	0.63	6.76	8.62	0.34	0.17
ET_0	RF	monthly		0.63	6.34	8.64	0.49	0.08
B1-B12	RF	weekly	1C	0.63	6.91	8.64	0.34	0.1
Δ (K_c:$NDVI$)	LR	weekly	2A	0.62	6.72	8.66	0.67	0.04
B1-B12, ET_0, P	RF	monthly	1C	0.62	7.04	8.68	0.56	0.05
Δ (K_c:$NDWI$)	LR	monthly	2A	0.62	6.74	8.7	0.23	0.27
Δ (K_c:$NDVI$)	LR	weekly	1C	0.62	6.64	8.73	0.65	0.14
CWR (K_c:$NDRE$)	RF	monthly	1C	0.61	6.26	8.8	0.42	0.06
CWR (K_c:$NDVI$)	RF	monthly	2A	0.61	6.72	8.8	0.48	0.1
Δ (K_c:$NDWI$)	LR	monthly	1C	0.61	6.83	8.81	0.46	0.27
B1-B12, ET_0, P	RF	monthly	2A	0.61	7.21	8.83	0.38	0.12
ET_c (K_c:$NDVI$)	RF	weekly	1C	0.61	6.88	8.84	0.45	0.15
CWR (K_c:$NDRE$)	RF	monthly	2A	0.61	6.65	8.84	0.19	0.37
Δ (K_c:$NDVI$)	RF	monthly	2A	0.61	6.7	8.86	0.6	0.07
$NDWI$	LR	weekly	1C	0.6	7.12	8.92	0.4	0.29
ET_c (K_c:$NDRE$)	RF	weekly	1C	0.6	6.58	8.94	0.47	0.08
CWR (K_c:$NDWI$)	RF	monthly	2A	0.6	6.7	8.99	0.38	0.1
ET_c (K_c:$NDRE$)	LR	weekly	1C	0.59	7.03	9.03	0.4	0.1
CWR (K_c:$REIP$)	RF	monthly	2A	0.59	6.63	9.04	0.41	0.15

Features	**M.**	**Res.**	**L.**	R^2	MAE	$RMSE$	CV	$CV std$
ET_c (K_c:$NDWI$)	RF	weekly	2A	0.59	6.27	9.05	0.54	0.06
CWR (K_c:$REIP$)	RF	weekly	2A	0.59	6.87	9.07	0.57	0.11
ET_c (K_c:$NDWI$)	RF	weekly	1C	0.58	6.3	9.14	0.47	0.14
CWR (K_c:$NDWI$)	RF	monthly	1C	0.58	6.87	9.15	0.27	0.21
Δ (K_c:$NDRE$)	LR	monthly	1C	0.58	6.98	9.16	0.48	0.14
B1-B12	RF	monthly	1C	0.58	7.4	9.19	0.42	0.14
Δ (K_c:$REIP$)	RF	monthly	1C	0.57	6.3	9.21	0.54	0.17
ET_c (K_c:$NDRE$)	RF	weekly	2A	0.57	6.65	9.23	0.45	0.13
Δ (K_c:$REIP$)	LR	monthly	2A	0.57	7.45	9.24	0.39	0.15
CWR (K_c:$NDRE$)	LR	weekly	1C	0.57	7.32	9.3	0.43	0.16
CWR (K_c:$NDVI$)	RF	weekly	2A	0.56	6.74	9.37	0.36	0.1
Δ (K_c:$NDRE$)	LR	monthly	2A	0.56	7.26	9.41	0.31	0.11
Δ (K_c:$NDVI$)	LR	monthly	1C	0.55	7.28	9.46	0.39	0.2
CWR (K_c:$NDRE$)	LR	monthly	1C	0.54	7.41	9.55	0.48	0.07
CWR (K_c:$NDVI$)	LR	monthly	1C	0.54	7.49	9.56	0.38	0.16
CWR (K_c:$NDRE$)	LR	weekly	2A	0.54	7.51	9.57	0.45	0.04
B1-B12	RF	monthly	2A	0.54	7.61	9.57	0.3	0.27
CWR (K_c:$NDWI$)	LR	monthly	2A	0.54	7.2	9.6	0.12	0.42
ET_c (K_c:$NDRE$)	LR	weekly	2A	0.54	7.41	9.61	0.39	0.14
ET_c (K_c:$NDVI$)	RF	monthly	1C	0.54	7.3	9.61	0.26	0.15
ET_c (K_c:$NDVI$)	RF	weekly	2A	0.53	7.16	9.73	0.5	0.06
CWR (K_c:$NDRE$)	LR	monthly	2A	0.52	7.59	9.74	0.25	0.25
CWR (K_c:$NDVI$)	LR	weekly	1C	0.52	7.67	9.75	0.5	0.08
$NDWI$	RF	weekly	1C	0.52	7.36	9.79	0.41	0.12
$NDWI$	RF	weekly	2A	0.52	7.16	9.79	0.28	0.24
CWR (K_c:$NDWI$)	LR	monthly	1C	0.52	7.4	9.81	0.35	0.13
ET_c (K_c:$NDRE$)	RF	monthly	1C	0.52	7.04	9.82	0.42	0.17
CWR (K_c:$NDVI$)	LR	monthly	2A	0.52	7.73	9.84	0.26	0.29
CWR (K_c:$REIP$)	LR	monthly	2A	0.51	7.85	9.84	0.11	0.17
Δ (K_c:$NDVI$)	LR	monthly	2A	0.51	7.62	9.85	0.3	0.07

Features	**M.**	**Res.**	**L.**	R^2	MAE	$RMSE$	CV	$CV std$
$NDRE$	LR	weekly	2A	0.51	7.73	9.91	0.29	0.06
CWR (K_c:$REIP$)	LR	monthly	1C	0.49	7.89	10.04	0.36	0.17
$NDRE$	LR	weekly	1C	0.49	7.87	10.05	0.3	0.13
Δ (K_c:$REIP$)	LR	monthly	1C	0.49	7.61	10.09	0.36	0.17
$REIP$	LR	weekly	2A	0.49	7.88	10.14	0.49	0.08
$REIP$	RF	monthly	2A	0.48	7.32	10.17	0.31	0.17
$NDWI$	RF	monthly	2A	0.48	7.85	10.2	0.43	0.08
$REIP$	RF	weekly	2A	0.48	7.65	10.23	0.26	0.21
$REIP$	RF	weekly	1C	0.47	7.3	10.24	0.38	0.09
$NDVI$	RF	weekly	2A	0.47	7.89	10.25	0.27	0.08
ET_c (K_c:$NDWI$)	RF	monthly	1C	0.46	7.1	10.39	0.38	0.14
CWR (K_c:$REIP$)	LR	weekly	1C	0.46	8.01	10.41	0.44	0.12
$NDWI$	RF	monthly	1C	0.46	7.98	10.42	0.38	0.14
$REIP$	LR	weekly	1C	0.45	8.06	10.45	0.39	0.04
$NDRE$	RF	weekly	2A	0.45	7.81	10.49	0.2	0.38
$NDRE$	RF	weekly	1C	0.45	8.0	10.52	0.23	0.05
$NDVI$	RF	weekly	1C	0.44	7.97	10.56	0.21	0.03
$REIP$	RF	monthly	1C	0.44	7.98	10.56	0.32	0.11
ET_c (K_c:$NDWI$)	RF	monthly	2A	0.44	6.99	10.57	0.42	0.05
$NDVI$	RF	monthly	1C	0.43	8.24	10.67	0.19	0.15
$NDVI$	LR	weekly	1C	0.43	8.41	10.68	0.12	0.42
ET_c (K_c:$NDRE$)	RF	monthly	2A	0.41	7.54	10.82	0.34	0.13
ET_c (K_c:$NDVI$)	RF	monthly	2A	0.41	8.13	10.87	0.31	0.07
$REIP$	LR	monthly	1C	0.4	8.79	10.97	0.27	0.06
$NDWI$	LR	weekly	2A	0.39	7.99	10.99	0.35	0.18
$NDVI$	LR	monthly	1C	0.38	8.49	11.13	0.27	0.1
$REIP$	LR	monthly	2A	0.38	9.11	11.15	0.4	0.04
$NDRE$	LR	monthly	1C	0.37	8.89	11.23	0.19	0.23
$NDRE$	RF	monthly	2A	0.36	8.07	11.31	0.29	0.12
$NDVI$	LR	weekly	2A	0.36	8.88	11.34	0.19	0.07

Features	**M.**	**Res.**	**L.**	R^2	MAE	$RMSE$	CV	$CV std$
$NDRE$	RF	monthly	1C	0.33	8.42	11.55	0.13	0.12
ET_c (K_c:$REIP$)	LR	monthly	1C	0.33	8.59	11.58	0.12	0.09
$NDVI$	RF	monthly	2A	0.32	8.69	11.62	0.21	0.06
$NDRE$	LR	monthly	2A	0.32	9.2	11.65	0.2	0.11
$NDWI$	LR	monthly	2A	0.31	9.25	11.72	0.02	0.11
$NDWI$	LR	monthly	1C	0.31	9.22	11.74	0.27	0.14
$NDVI$	LR	monthly	2A	0.3	9.32	11.83	-0.0	0.31
ET_c (K_c:$NDWI$)	LR	monthly	2A	0.27	9.07	12.08	0.12	0.19
ET_c (K_c:$NDRE$)	LR	monthly	1C	0.26	9.24	12.12	0.09	0.14
ET_c (K_c:$NDWI$)	LR	monthly	1C	0.26	9.22	12.18	0.03	0.31
ET_c (K_c:$NDRE$)	LR	monthly	2A	0.25	9.3	12.23	-0.16	0.24
ET_c (K_c:$NDVI$)	LR	monthly	1C	0.24	9.43	12.33	0.18	0.08
ET_c (K_c:$NDVI$)	LR	monthly	2A	0.22	9.53	12.46	0.12	0.18
ET_0	LR	monthly		0.08	10.64	13.58	-0.05	0.15
ET_c (K_c:$REIP$)	LR	monthly	2A	0.07	10.65	13.59	0.06	0.11

B.7 ET validation

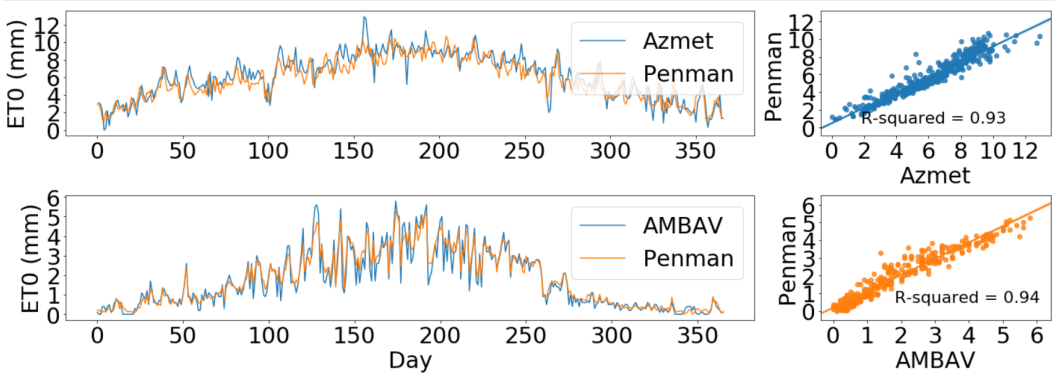

Figure B.5: Comparison of calculated ET_0 values for 2016 based on climatological data from DarkSky (DarkSky, 2020). The comparison was done with evapotranspiration data from DWD (DWD, 2020a,b) and the Arizona meteorological network (AZMET) (The University of Arizona, 2020). Depending on the data source, the ET_0 results vary slightly as the climatological parameters may vary.

C Acknowledgements

In 2015, I decided to turn my life in a new direction with the aim to found a start-up in the field of precision farming. At that time, I was not aware of the paths such a decision could take. A start-up turned into a dissertation, which gave me the opportunity to develop professionally and personally and to become more aware of my weaknesses and strengths. In these eventful years, with setbacks, but also important insights, I had the support of several people whom I would like to thank at this point.

I thank my friends for the conversations and the one or other evening that got me through exhausting times. I would like to thank especially Daniela and Matthias for the encouraging and funny evenings. I was very happy to discuss with colleagues about machine learning, statistics, regression or new precision farming applications. I would like to thank all my colleagues of the faculty and in Dürnast who helped me with questions and answers or cheered me up with a houseplant, a conversation or coffee, and especially Maximilian and Anna for their yield data. Although my work was mainly on the computer, I have enjoyed working and experiencing agriculture in Dürnast from time to time. I would like to thank the colleagues from the Chair of Remote Sensing Technology and especially Dr. Marco Körner for his professional support and time to improve my work. I would like to thank Dr. Andreas Vollrath for helping me as a mentor. I would like to thank Prof. Asseng for his willingness to act as examiner, and Prof. Yu for taking over the chairmanship of the commission.

The most important comes at the end. I would like to thank Prof. Urs Schmidhalter for his support over the past years. I have gone through a work-intensive time of my life. Your encouraging words and your helpfulness have helped me a lot.

I would like to thank my parents Monika and Jan who always supported me to reach my goals.